Université de Strasbourg

THÈSE DE DOCTORAT

pour obtenir le titre de

DOCTEUR EN PHYSIQUE DE LA MATIÈRE CONDENSÉE

Theoretical study of electronic structure and magnetism in materials for spintronics

---

par Fatima IBRAHIM

soutenue le 31 Janvier, 2014

Membres du Jury:

Directeur de Thése	: Mébarek ALOUANI
Rapporteur Externe	: Mairbek CHSHIEV
	: Thierry DEUTSCH
Examinateur	: Jean-Louis GALLANI.

Institut de physique et Chimie des Matériaux de Strasbourg

Acknowledgement

Performing my PhD thesis in the Institut de Physique et Chimie des Matèriaux de Strasbourg (IPCMS), I had the pleasure to work for three years among leaders in the scientific society. By the end of this period, I would like to express my gratitude to all those who gave me the possibility to complete this thesis.

I am deeply indebted to my supervisor Prof. Mébarek Alouani whose stimulating suggestions and encouragement helped me all over the period of my thesis. Thank you for offering me this valuable chance to perform my PhD studies under your worthily and precious supervision. Thank you for your efforts, scientific instructions, and discussions that you provided me with, in order to achieve my Thesis.

I gratefully acknowledge the direction of the IPCMS and especially the DMONS department for giving me the opportunity to perform my thesis studies in this institute.

I would like also to thank all the experimental scientists who contributed to this work through their experimental results and fruitful discussions: the group of Nathalie Viart, Christian Meny, Daniel Stoeffler, Martin Bowen, Eric Beaurepaire, Samy Boukari, and Wolfgang Weber.

I have furthermore to thank the members of the jury Mairbek Chshiev, Thierry Deutsch, and Jean-Louis Gallani who accepted to review this work.

Thanks to all my coworkers whom I enjoyed working with. Thank you Ali Jaafar, Saqib Javaid, Saber Gueddida, and Fatima Djeghloul. Thanks to all my office colleagues: Mohammad Haidar, Vincent Davesne, Wojciech Szewc, Filip Schleicher, Dimitra Xenioti, Hashim Al Daboochah, Mohammad Hamieh, and Puja Dey.

Special thanks to every one of my friends for the good moments that we shared together. Rania and Jamal Mohammed, Ahmed Maghraoui and Ferdaous Ben Romdhane, Iman Abdalla, Israa Slim, Ali Jaafar and Salsabil Marzoughi Jaafar, Batoul Srour, Ola Srour, Batoul and Mohammad Hamieh, ...Thank you all.

I would like to thank my parents whose presence during my defense meant a lot to me. Thank you for supporting and encouraging me during all these years no matter what I say I can not thank you enough.

A deep thank you from my heart to my husband, Ali Hallal, who was by

my side in the happy and sad moments to give me support and courage to continue. Also a deep thanks for my little son, Mohammad-Hussein Hallal, whose presence gave me a lot of courage. He is my partner in this work since he was in my womb during the fruitful part of my thesis.

Finally, a special thank you to sir Abu Saleh and Om Banin for their support, I owe you a lot.

Contents

List of Figures

Chapter 1
Introduction

In areas of modern research on the nanoscale, spintronics is an emerging active field based on utilizing the electron spin to encode information in electronic devices. The essence of spintronics resides in the concept of magnetoresistance where both the giant magnetoresistance (GMR) [Zutic 2004] and tunneling manetoresistance (TMR) [Julliere 1975] phenomena resemble the spin-polarized transport in either spin valves or magnetic tunnel junctions. In this concept, a spacer, which could be either a non-magnetic metal or an insulator, is sandwiched between two ferromagnetic electrodes such that the difference in the resistance between parallel and antiparallel configurations of the electrodes corresponds to the magnetoresistance. Considering the fact that transport properties strongly depend on the magnetic properties, the prospect of spintronics requires developing and employing materials with remarkable magnetic properties. To this end, ab-initio calculations have become an efficient tool to understand characteristic properties of materials and which provides interpretation for experimentally observable phenomena.

The aim of this thesis is to understand the physics of functional magnetic materials proposed for spintronic applications using ab-initio density functional simulations. In this respect, two classes of functional materials are considered: the magnetoelectric oxide, gallium ferrite (GFO), and the hybrid organic/ferromagnet interface, manganese phthalocyanine/cobalt (MnPc/Co). In fact, both magnetoelectric and organic materials have received growing interests in the field of spintronics.

1.1 Magnetoelectric materials

First, we consider the magnetoelectric materials. Such materials accommodate both magnetic and electric properties, i.e. coexistence of a magnetization and polarization together with a coupling among these two degrees of freedom known as the magnetoelectric effect. In fact, the magnetoelectric coupling provides the opportunity of the electric control of the magnetization and vice versa. This feature triggered the proposals of possible spintronic device designs where magnetoelectric materials are incorporated in a magnetoelectric memory device [Bibes 2008, Binek 2005]. Such devices include TMR device involving a magnetoelectric film as a tunnel barrier between two ferromagnetic layers across which a bias voltage is applied. The other proposed device is based on spin valves used in GMR systems where a magnetoelectric film serves as a tunable pinning bottom layer. The principle of functioning in these applications relies on the magnetoelectric coupling within the magnetoelectric material and the exchange coupling across its interface with the ferromagnetic adjacent layer.

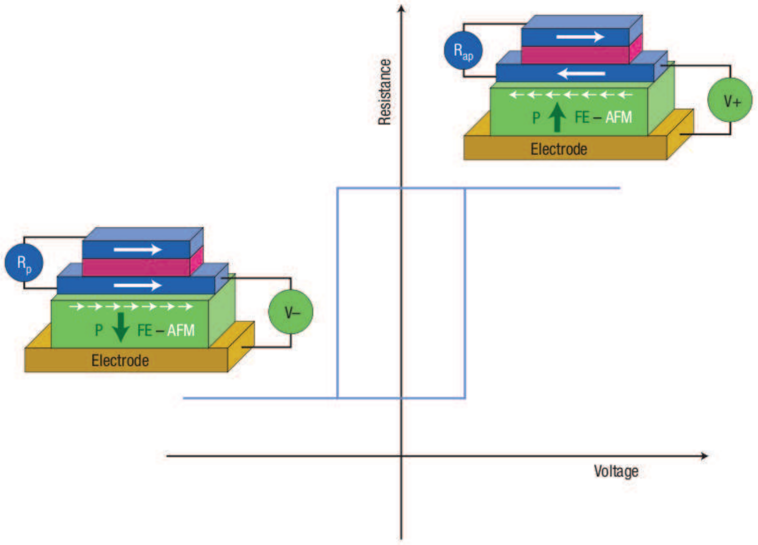

Figure 1.1: Schematic of possible integration of a magnetoelectric material in a spin valve [Bibes 2008].

In the frame of research on magnetoelectric materials that possess peculiar properties, such as an overall non-vanishing magnetization holding up to room temperature and a strong magnetoelectric effect, GFO has so far appeared of particular interest [Remeika 1960, Rado 1964]. Indeed, the electronic and magnetic properties of GFO have rarely been investigated theoretically. In particular, the theoretical investigation of the experimentally-demonstrated dependence of GFO properties on the Fe concentration [Arima 2004, Trassin 2009] seems to be interesting. Besides, a more detailed magnetic description on the microscopic scale is required, namely the anisotropic feature of the system. These issues are addressed in a considerable part of this thesis.

1.2 Hybrid organic/ferromagnetic interfaces

Motivated by the scope of developing organic spin devices [Naber 2007], the study of the spin properties of organic semiconductors have attracted considerable attention [Dediu 2009, Atodiresei 2010, Iacovita 2008]. In fact, the crucial property that introduces organic semiconductors as such good candidates is that spin-orbit coupling and hyperfine interactions are predicted to be extremely small [Dediu 2009, Sanvito 2007]. Interestingly, organic semiconductors are capable of forming hybrid organic-ferromagnetic interfaces that exhibit high spin-injection efficiency [Sanvito 2010]. In this case, the spin injection can be controlled by tuning the interface electronic and magnetic properties. The family of phthalocyanine (Pc) offers a potential choice for these aforementioned hybrid interfaces due to their thermal stability and the possibility to tune their structure, chemical, magnetic, and transport properties [Wang 2009, Liao 2001].

Theoretical and experimental studies have witnessed and described a distinctive feature of Pc/ferromagnetic hybrid interfaces which is the presence of spin-polarized states introducing hereafter the concept termed spinterface [Methfessel 2011, Sanvito 2010]. In particular, manganese phthalocaynine MnPc/Co(001) has so far revealed interesting properties residing in its magnetic active interface [Javaid 2010]. However, a better understanding of the Co/MnPc interface is still required. For instance, a more detailed description of the spinterface-formation mechanism is crucial. Besides, it is obviously interesting to include spin-orbit coupling to gain detailed insight of its magnetic properties. In this respect, we address these arguments, in the second part of this thesis, while trying to provide a more realistic description of the interactions across a MnPc/metallic interface.

This manuscript consists of four main chapters as follows:
In chapter 2, we provide an overview of the fundamental ideas of the density functional theory, in particular, the projector augmented wave method is illustrated being the method used in the framework of this thesis. Chapter 3 gives a brief review of the relativistic density functional theory and the scalar relativistic approximation for the spin-orbit coupling. Besides, the magnetocrystalline anisotropy is defined and the methods for calculating it are described.
Chapter 4 is dedicated to the description of the properties of the magnetoelectric gallium ferrite (GFO). The chapter starts by introducing the well-known properties of GFO. Then, we show and discuss the results on the impact of the Fe concentration on the different properties of GFO: structural, electronic, magnetic, and magnetic anisotropy. The last part of this chapter addresses the optical properties where the basic theory is described followed by the optical properties of GFO; in particular, the optical properties are introduced as a good tool to determine the cationic site occupation in GFO.
In chapter 5, the interface between manganese phthalocyanine and Co(001) including both van der Waals and spin-orbit interaction is described and discussed. First, an overview of the well-known properties of Pc/metal interfaces preceded by the properties of the Pc molecules is given. In the second part of this chapter, the theoretical results on the electronic and magnetic properties of Co/MnPc interface are presented and discussed in view of experimental photoemission and x-ray magnetic circular dichroism (XMCD) results.
The manuscript ends up by drawing the main conclusions from this thesis and providing a perspective concerning the two main subjects discussed.

Chapter 2

Density functional theory and PAW method

Contents

2.1 Introduction

The fundamental basis of understanding the different properties of materials and phenomena relies upon understanding their electronic structure. Indeed, developing theoretical approaches that can accurately describe a system of interacting particles, electrons and nuclei, emerged as a serious challenge encountering theoretical physics. An exact theory for a system of ions and interacting electrons is intimately quantum mechanical based on solving a many-body Schrödinger equation which is evidently complex. One of the milestones in solving this problem is the Born-Oppenheimer approximation [Born 1927]. Their idea was that the ions can be thought of as moving slowly in space while the electrons respond instantaneously to any ionic motion. Consequently, the many-body wave function becomes explicitly dependent on the electronic degrees of freedom only. The validity of this approximation is based on the huge difference of mass between ions and electrons which allows considering the former as classical particles.

The simplification provided by the Born-Oppenheimer approximation doesn't resolve the entire problem's complexity which now resides in the nature of the electrons themselves, namely the electron-electron interactions. In fact, such interactions involve the exchange property of the electrons which is an implication of Pauli exclusion principle beside the correlation property where each electron is affected by the motion of every other electron in the system. Integrating such complex types of interaction requires a more simplified approximation known as the one-electron picture in which the system is described by a collection of classical ions and single quantum particles that reproduce the behavior of the electrons. In developing this picture the exchange and correlation effects among electrons are not neglected, instead they are taken into account in an average or effective way. This is often referred to as the mean-field approximation for the electron-electron interactions.

The mean-field theory is the heart of the Hartree-Fock approximation [Fock 1930a, Fock 1930b]. In this case, the wave function of the many-body system is introduced as an antisymmetric product of single particle wave functions where each satisfies a Schrödinger equation. This approximation incorporates the exchange interactions which are the manifestation of Pauli exclusion principle, that act as so to separate electrons of the same spin. Consequently, a depletion of the charge density arises in the vicinity of a given electron forming what is known as the exchange hole. Although the Hartree-Fock approximation treats exactly the exchange, it neglects more detailed correlations due to many-body interactions in particular long-range Coulomb correlations. These missing correlations are reflected in the breakdown of the Hartree-Fock approximation in treating metallic and bulk systems in general where it usually overestimates the band gap and underestimates the binding energy.

The requirement for a computationally practicable approach that incorporates both the exchange and correlation prompted the arousal of the density functional theory which has become the primary tool for electronic structure calculations in condensed matter. In what follows we elucidate the fundamental ideas of the density functional theory. In particular, we illustrate on the projector augmented wave method being the density functional-based method used in the present work.

2.2 Density functional theory

2.2.1 Hohenberg-Kohn-Sham approach

In a series of seminal papers, Hohenberg, Kohn, and Sham developed a different way of looking at the electronic structure problem which has been called the density functional theory (DFT). This theory has a large impact on the calculations of the properties of molecules and solids. The basic concept of the DFT is that instead of dealing with the many-body Schrödinger equation which involves the many-body wave function, one deals with a formulation of the problem that involves the total density of the electrons.

DFT is based upon two theorems proved by Hohenberg and Kohn [Hohenberg 1964] that apply to any system of interacting particles in an external potential $V_{ext}(r)$ including any problem of electrons and nuclei where the Hamiltonian is written as

$$\hat{H} = -\frac{\hbar^2}{2m_e}\sum_i \nabla_i^2 + \sum_i V_{ext}(\mathbf{r}_i) + \frac{1}{2}\sum_{i\neq j}\frac{e^2}{|\mathbf{r}_i - \mathbf{r}_j|}. \tag{2.1}$$

The two theorems state that:

- The external potential $V_{ext}(\mathbf{r})$ is a unique functional of the electron density, thus all the ground-state properties are solely determined by the ground state density.

- The ground state energy is obtained variationally; the density that minimizes the total energy is the exact ground state density $n_0(r)$.

Later in 1965, Kohn and Sham provided an approach which replaces the difficult interacting many-body system with an auxiliary system of independent particles but with an interacting density [Kohn 1965]. The built-in assumption is that the ground state density of the interacting system is equal to that of some chosen non-interacting system. This brings out the Kohn-Sham independent particle equations of the form

$$[-\frac{\nabla^2}{2} + V_{eff}(\mathbf{r})]\psi_i(\mathbf{r}) = \epsilon_i \psi_i(\mathbf{r}). \tag{2.2}$$

The effective potential is expressed as

$$V_{eff}(\mathbf{r}) = V_{ext}(\mathbf{r}) + V_H(\mathbf{r}) + V_{xc}(\mathbf{r}), \tag{2.3}$$

where the external potential generated by the nuclei at position $\mathbf{R}_i$ having charge $Z_i e$ is

$$V_{ext}(\mathbf{r}) = \sum_i \frac{Z_i e^2}{|\mathbf{r} - \mathbf{R}_i|}, \tag{2.4}$$

the Hartree potential which is the electrostatic part of the electron-electron interaction is

$$V_H(\mathbf{r}) = \int d^3r' \frac{n(\mathbf{r}')}{|\mathbf{r} - \mathbf{r}'|}. \tag{2.5}$$

The exchange-correlation potential V_{xc} is the part of the potential which incorporates all the difficult many-body interactions. The density of this auxiliary system is constructed from the orbitals $\psi_i(\mathbf{r})$ such that

$$n(\mathbf{r}) = \sum_i |\psi_i(\mathbf{r})|^2. \tag{2.6}$$

Based on the nature of the Kohn-Sham approach where the effective potential depends on the density and the density itself depends on the one-particle states ψ_i, the solution of the Kohn-Sham equations is attained via self consistent manner. An actual calculation procedure utilizes a numerical procedure that successively changes V_{eff} and n to approach the self-consistent solution. For a given form of the exchange-correlation functional, a starting density is guessed which in turn determines a potential V_{eff}. This potential is used to obtain a solution of KS equation from which a new density is constructed and used to determine a new V_{eff}. This iterative process is applied until the output density doesn't vary with respect to the input one.

In the Kohn Sham approach to the full interacting many-body problem the Hohenberg-Kohn expression of the ground state energy functional is written as

$$E_{KS}[n(\mathbf{r})] = T_0[n(\mathbf{r})] + \int d\mathbf{r} V_{ext}(\mathbf{r})n(\mathbf{r}) + E_H[n(\mathbf{r})] + E_{xc}[n(\mathbf{r})]. \tag{2.7}$$

In this expression the first term represents the independent-particle kinetic energy

$$T_0[n(\mathbf{r})] = \sum_i^{occ} \langle \psi_i | -\frac{\hbar^2}{2m_e}\nabla^2 | \psi_i \rangle. \tag{2.8}$$

The accuracy of the ground-state density and energy obtained by solving the Kohn Sham equations is limited by the approximation in the crucial exchange-correlation functional since its exact form is unknown. In fact, E_{xc} is often relatively a small fraction of the total energy but is typically of large contribution to the chemical bonding. Therefore, accurate approximations to the E_{xc} are required to the whole enterprise of the DFT. Despite the complexity in the nature of the exchange-correlation functional, great progress has been made with remarkable simple approximations; an issue that is addressed in the following section.

2.2.2 Expressions of the exchange-correlation potential

Kohn and Sham proposed the most popular way of dealing with the complexity of the exchange-correlation functional, the local-density approximation (LDA). They suggested that solids can often be considered close to the limit of the homogeneous electron gas which implies that the effects of exchange and correlation are local in character. Thus, the exchange-correlation energy can be simply expressed as an integral over all space with the exchange-correlation density at each point assumed to be the same as in a homogeneous electron gas with that density and is expressed as follows:

$$E_{xc}^{LDA}[n(\mathbf{r})] = \int d^3 r n(\mathbf{r}) \epsilon_{xc}^{homo}(n(\mathbf{r})), \tag{2.9}$$

where ϵ_{xc}^{homo} is the exchange-correlation energy per electron in a homogeneous electron gas. Highly accurate results for the evaluation of this latter were found by Ceperley and Alder [Ceperley 1980] using Quantum Monte-Carlo techniques and parametrized by Perdew and Zunger [Perdew 1981a]. Therefore, LDA is exact for a uniform density or more generally for densities that vary slowly in space. In particular, LDA should be valid when the length scale of the density variation is large compared to the length scales set by the local density such as the Fermi wavelength or the screening length. Consequently, LDA is convenient for the description of simple crystalline metals while it is worst for very inhomogeneous cases such as atoms.

Indeed, some of the well known failures of the LDA such as the overestimation of the cohesive energies have stimulated the attempts to construct better functionals. In this sense, the gradient-corrected functionals were introduced as the simplest extension of LDA to inhomogeneous systems. In this case, not only the local density but also its local gradient are used to incorporate more information about the electron gas. The generalized-gradient approximation (GGA) denotes a variety of ways proposed for functions that modify the behavior at large gradients in a way to preserve the desired properties. Thus, the exchange-correlation functional is expressed as follows:

$$E_{xc}^{GGA}[n(\mathbf{r})] = \int d^3 r n(\mathbf{r}) \epsilon_{xc}^{homo}(n(\mathbf{r})) F_{xc}(n(\mathbf{r}), |\nabla n(\mathbf{r})|), \tag{2.10}$$

where F_{xc} is an enhancement factor that is expressed in terms of the average distance between electrons r_s and a dimensionless reduced density gradient $s(\mathbf{r})$:

$$F_{xc}(n(\mathbf{r}), |\nabla n(\mathbf{r})|) \to F_{xc}(\mathbf{r}_s, s), \tag{2.11}$$

and

$$s(\mathbf{r}) = \frac{|\nabla n(\mathbf{r})|}{2k_F n(\mathbf{r})}. \tag{2.12}$$

The three most widely used forms of expressing F_{xc} have been proposed by Becke (B88) [Becke 1988], Perdew and Wang (PW91) [Perdew 1992], and Perdew, Burke, and Enzerhof (PBE) [Perdew 1996]. The behavior of GGA functionals relative to LDA can be understood on the basis of many comparative studies that have been done and whose results yield the following: (1) GGA improves the ground-state properties of atoms due to the lowered exchange energies that lead to the reduction of the binding energies and corrects the LDA over-binding. (2) Many properties of transition metals are improved [Ozolins 1993]. (3) In general, the structural properties are improved despite that GGAs sometimes overcorrect the LDA errors in lattice parameters [Proynov 1995]. (4) The description of Mott-Hubbard insulators is not significantly improved over the LDA [Terakura 1984, Pickett 1989].

As a matter of fact, both LDA and GGA functionals break down in treating materials in which electrons are localized and strongly interacting such as transition metal oxides and rare earth elements [Pickett 1989]. These systems contain localized atomic-like electronic states, originating from d or f atomic states, together with delocalized band-like states, originating from s and p states. The correct description of both set of states is problematic as LDA and GGA provide orbital-independent potentials that may produce incorrect occupancy of localized states leading to an incorrect description of the properties of such materials. Therefore, several methods have been developed beyond the functional approach to incorporate strong electron-electron correlations such as the self-interaction corrections (SIC) [Perdew 1981a] and LDA+U method [Anisimov 1997]. In the framework of this thesis the LDA+U approach was used and is addressed in the following section.

2.2.3 The LDA+U method

The LDA+U is an orbital-dependent method where the electrons are classified into two classes: delocalized s and p which can be well described by the usual LDA or GGA, and localized d or f electrons for which an orbital-dependent term should be used to account for the Coulomb d-d and f-f interactions known as the Hubbard-type interaction:

$$H = \frac{1}{2} U \sum_{i \neq j} n_i n_j, \tag{2.13}$$

where

$$U = E(d^{n+1}) + E(d^{n-1}) - 2E(d^n) \tag{2.14}$$

is the Hubbard parameter representing the Coulomb energy cost to place two electrons at the same site. The generalized LDA+U functional is defined as follows:

$$E^{LDA+U}[n(\mathbf{r}), \hat{n}] = E^{LDA}[n(\mathbf{r})] + E^{U}[\hat{n}] - E_{dc}[\hat{n}], \tag{2.15}$$

where $\hat{n}$ is the density matrix for d or f electrons. The first term in Eq. 2.15 is the standard LDA energy functional and the second is the electron-electron

Coulomb interaction energy given by:

$$\begin{aligned} E^U[\hat{n}] =& \frac{1}{2}\sum_{m,\sigma}\langle m,m''|V_{ee}|m',m'''\rangle n^{\sigma}_{m,m'} n^{-\sigma}_{m''',m'''} - (\langle m,m''|V_{ee}|m',m'''\rangle) \\ & -(\langle m,m''|V_{ee}|m''',m'\rangle) n^{\sigma}_{mm'} n^{\sigma}_{m''m'''}, \end{aligned} \tag{2.16}$$

where m denotes the magnetic quantum number and V_{ee} is the screened Coulomb interaction among localized electrons. The third term is the energy that corrects the double counting and is given by:

$$E_{dc}[\hat{n}^{\sigma}] = \frac{1}{2}UN(N-1) - \frac{1}{2}J[N^{\uparrow}(N^{\uparrow}-1) + N^{\downarrow}(N^{\downarrow}-1)], \tag{2.17}$$

where $N^{\sigma} = Tr(n^{\sigma}_{mm'})$ and $N = N^{\uparrow} + N^{\downarrow}$ while U and J are the screened Coulomb and exchange parameters respectively. In this case, the effective single particle Hamiltonian is:

$$\hat{H} = \hat{H}_{LDA} + \sum_{mm'} |inlm\sigma\rangle V^{\sigma}_{mm'} \langle inlm'\sigma|, \tag{2.18}$$

where i denotes the site, n the main quantum number, and l the orbital quantum number while the effective single-particle potential is expressed as:

$$\begin{aligned} V^{\sigma}_{mm'} =& \sum_{\hat{m}} \langle m,m''|V_{ee}|m',m'''\rangle n^{-\sigma}_{m''m'''} - (\langle m,m''|V_{ee}|m',m'''\rangle) \\ & - \langle m,m''|V_{ee}|m''',m'\rangle) n^{\sigma}_{m''m'''} - U(N-\frac{1}{2}) + J(N^{\sigma}-\frac{1}{2}). \end{aligned} \tag{2.19}$$

The matrix elements of V_{ee} can be expressed in terms of complex spherical harmonics and effective Slater integrals F^k as follows:

$$\langle m,m''|V_{ee}|m',m'''\rangle = \sum_{k} a_k(m,m',m'',m''')F^k, \tag{2.20}$$

where $0 \leq k \leq 2l$ and

$$a_k(m,m',m'',m''') = \frac{4\pi}{2K+1}\sum_{q=-k}^{k} \langle lm|Y_{kq}|lm'\rangle \langle lm''|Y^{*}_{kq}|lm'''\rangle. \tag{2.21}$$

The relations between the slater integrals and the Coulomb U and exchange J parameters for $3d$ or $4d$ systems are:

$$U = F^0, J = \frac{F^2+F^4}{14}, \tag{2.22}$$

while for $4f$ or $5f$ systems:

$$J = \frac{286F^2 + 195F^4 + 250F^6}{6435}. \tag{2.23}$$

2.2.4 Solving Kohn-Sham Equations

The Kohn-Sham equations, with the underlying independent-particle approach, provide a way to obtain the exact ground state density along with a self-consistency requirement. In solids, a further simplification is provided by Bloch's theorem as the charge density and consequently the single-particle Kohn-Sham Hamiltonian has the periodicity of the lattice. Thus, the Kohn-Sham orbitals with different Bloch momenta are coupled through the density-dependent potential. Accordingly, the single particle Kohn-Sham equations may be solved separately on a grid of sampling points in the symmetry irreducible wedge of the Brillouin zone, and the resulting orbitals are used to construct the charge density. Indeed, there are several electronic structure schemes used to solve the Kohn-Sham equations providing different representations of the charge density, potential, and the Kohn-Sham orbitals. In the following we give a quick overview of these approaches.

1. Planewave pseudopotentials

   In this method, the Kohn-Sham orbitals are expanded in a complete set of planewaves $e^{i\mathbf{k}.\mathbf{r}}$ while the strong core potential is replaced by a pseudopotential whose ground state wave function mimics the all-electron valence wave function outside a selected core radius. A pseudopotential can be generated in an atomic calculation and then used to compute properties of valence electrons in molecules or solids since the core states remain almost unchanged [Singh 2006]. In fact, since pseudopotentials are not unique, this allows the freedom to choose forms that simplify the calculations and the interpretation of the resulting electronic structure. Many of these ideas originated in the orthogonalized plane-wave (OPW) approach [Callaway 1955] that handles the eigenvalue problem in terms of a smooth part of the valence wave function plus core or core-like wave functions. Later, the OPW method was brought into the modern framework of energy functionals by the projector augmented wave (PAW) [Blochl 1994] approach which uses pseudopotential operators while keeping the full core wave functions.

2. Localized atomic-(like) orbitals

   The basic idea of these methods is to use atomic orbitals as the basis set to expand the single-electron wave function in the Kohn-Sham equations. The well-known method in this class is the linear combination of atomic orbitals (LCAO) where the semi-empirical tight-binding method, associated with Slater and Koster, is considered to be simple and instructive since one needs only the matrix elements of the overlap and Hamiltonian [Slater 1954]. Besides, full potential calculations are done with localized bases such as gaussians, Slater-type orbitals, and numerical radial atomic-like orbitals. The full potential non-orthogonal local orbital (FLPO) method [Eschrig 1987] uses, in addition to the spherical average of the crystal potential, the so-called confining potential to compress the long range tail of the local orbitals.

3. Atomic-sphere methods

   The basic idea is to divide the electronic structure problem providing efficient representation of atomic-like features that are rapidly varying near the nucleus and smoothly varying functions between the atoms. Methods in the class can be considered as a combination of plane-wave method and localized atomic orbitals where localized atomic orbitals are employed near the nuclei and plane waves in the interstitial region. The heart of the augmented plane wave (APW) [Slater 1953] and Green's function Korringa-Kohn-Rostoker (KKR) [Korringa 1947, Kohn 1954] method is that smooth functions are augmented near each nucleus by solving Schrödinger equation in the sphere at each energy and matching to the outer wave function. Indeed, the APW and KKR methods suffer from the fact that they require solution of nonlinear equations. Accordingly, advances made use of the linearization of the equations around reference energies which allows any of the augmented methods to be written in the form of secular equation linear in energy involving an energy independent Hamiltonian and overlap matrix. This simplification led to further advances, such as developing full-potential methods (e.g. LAPW [Singh 2006] and LMTO [Andersen 1975]).

2.3 Projector augmented wave method

The projector augmented wave (PAW) method [Blochl 1994] is an approach that combines the flexibility of LAPW method and the simplicity of the plane wave pseudopotential approach bringing out the most general augmentation scheme. Being an all electron method, the extracted matrix elements and expectation values correspond to the all-electron state subjected to the full all-electron potential. Indeed, PAW utilizes the frozen core approximation where the core states are imported from the isolated atom since they are slightly affected upon bond formation.

2.3.1 Decomposition of the wave function

In materials, wave functions have different signatures in different regions of space: they vary smoothly between the atoms due to the weak potential while they rapidly oscillate near the nuclei since the electrons feel the large attractive potential of the nuclei. Consequently, a reasonable treatment of the wave function requires dividing the space into two regions which is the heart of the augmented wave methods.

- Augmentation region consists of non-overlapping atom-centered spheres of radius r_c^a where a is the atom index.
- Interstitial region which covers the space between the augmented spheres.

Accordingly, the idea is to the expand the wave function of the valence electrons into different basis: plane waves in the interstitial region and atomic-like partial waves in the augmentation region. Indeed, the dual representation of the wave function together with its derivative should be assured to be continuous at the boundaries of the spheres.

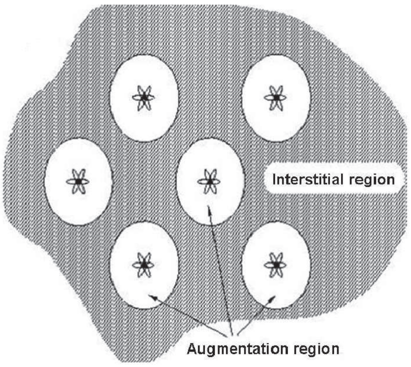

Figure 2.1: Illustration of the dual representation of the space: interstitial region and augmentation region.

The PAW formalism is based on a linear transformation $\hat{T}$ that transforms the physically relevant all-electron wave function $|\psi_n\rangle$ onto fictitious pseudo wave function $|\tilde{\psi}_n\rangle$:

$$|\psi_n\rangle = \hat{T}|\tilde{\psi}_n\rangle, \tag{2.24}$$

where the index n resembles the band and the **k** vector indices. The transformation operator $\hat{T}$ is defined as follows:

$$\hat{T} = 1 + \sum_a \hat{T}^a, \tag{2.25}$$

such that $\hat{T}^a$ are local atom-centered contributions each of which acts only within an augmentation region Ω^a. This implies that the all-electron and the pseudo- wave functions coincide outside the augmentation regions. In fact, to define the local terms $\hat{T}^a$, the all-electron wave function is expanded into all-electron partial waves ϕ_i^a, within Ω^a, to each of which is defined a smooth pseudo partial wave $|\tilde{\phi}_i^a\rangle$ such that:

$$|\phi_i^a\rangle = (1 + \hat{T}^a)|\tilde{\phi}_i^a\rangle. \tag{2.26}$$

Each all-electron partial wave $|\phi_i^a\rangle$ is identical to its smooth counterpart $|\tilde{\phi}_i^a\rangle$ outside the augmentation region. Besides, these pseudo partial waves should also form a complete set within the augmentation region so that every pseudo wave function can be expanded into pseudo partial waves:

$$|\tilde{\psi}_n\rangle = \sum_i c_{i,n}^a |\tilde{\phi}_{i,n}^a\rangle, \ \textit{within}\ \Omega^a, \tag{2.27}$$

where $c_{i,n}^a$ are some expansion coefficients to be determined. Since $|\phi_i^a\rangle = \hat{T}|\tilde{\phi}_i^a\rangle$, the corresponding all-electron wave function which is expressed as:

$$|\psi_n\rangle = \hat{T}|\tilde{\psi}_n\rangle = \sum_{i,n} c_{i,n}^a |\phi_i^a\rangle, \ \textit{within}\ \Omega^a, \tag{2.28}$$

has the same expansion coefficients $c_{i,n}^a$. Indeed, the transformation $\hat{T}$ is required to be linear, which implies that the coefficients $c_{i,n}^a$ should be linear functionals of the pseudo wave function $|\tilde{\psi}_n\rangle$. Hence,

$$c_{i,n}^a = \langle \tilde{p}_i^a | \tilde{\psi}_n \rangle, \tag{2.29}$$

where $|\tilde{p}_i^a\rangle$ are some fixed functions termed projector functions such that there is exactly one projector function for each pseudo partial wave. In the augmentation region, the projector functions must fulfill the condition:

$$\sum_{i,a} |\tilde{\phi}_i^a\rangle\langle\tilde{p}_i^a| = 1, \tag{2.30}$$

which implies that

$$\langle \tilde{p}_i^a | \tilde{\phi}_j^a \rangle = \delta_{i,j}. \tag{2.31}$$

In principle, there are no restrictions on the choice of the projector functions outside the augmentation regions but for convenience they are chosen to be localized in the augmentation regions.
As a consequence, the linear transformation between the valence wave functions and the pseudo wave functions is written as:

$$\hat{T} = 1 + \sum_{i,a} (|\phi_i^a\rangle - |\tilde{\phi}_i^a\rangle)\langle \tilde{p}_i^a|. \tag{2.32}$$

Thereby, by using this transformation the all-electron Kohn-Sham wave function is obtained from the pseudo wave function as follows:

$$|\psi_n\rangle = |\tilde{\psi}_n\rangle + \sum_{i,a} (|\phi_i^a\rangle - |\tilde{\phi}_i^a\rangle)\langle \tilde{p}_i^a|\tilde{\psi}_n\rangle. \tag{2.33}$$

Thus, the transformation is determined by: the all-electron partial waves $|\phi_i\rangle$ which are determined by solving the radial Schrödinger equation for the isolated atom and orthogonalized to the core states, the pseudo partial waves $|\tilde{\phi}_i\rangle$ which are expanded into planewaves, and a projector function $|\tilde{p}_i\rangle$ which is localized within the augmentation region associated with each pseudo partial wave. The projectors are calculated as a radial function multiplied by spherical harmonics but are then transformed into planewave representation.

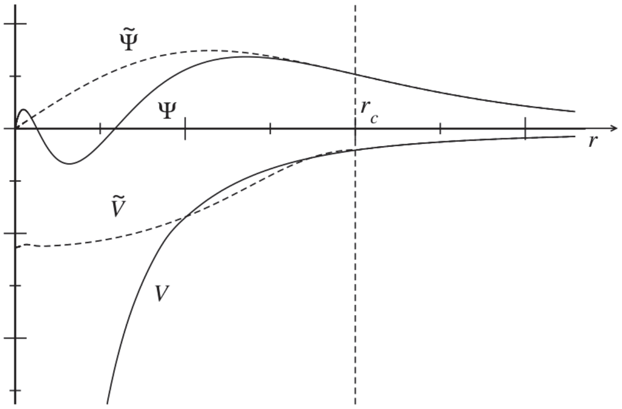

Figure 2.2: Comparison of the real Ψ to the pseudo $\tilde{\Psi}$ wave function and the real V to the pseudo potential $\tilde{V}$.

2.3.2 Expectation values of operators

In the PAW method, the pseudo wave functions are the variational parameters instead of the all-electron wave function. As a consequence, the observables must be given in the form of expectation values of the pseudo wave functions which requires transforming the operators into pseudo operators. The expectation value of some operator $\langle A \rangle$ is defined as,

$$\langle A \rangle = \sum_n f_n \langle \psi_n | A | \psi_n \rangle, \tag{2.34}$$

where f_n is the occupation of the state and n is the band index. Using the definition of the transformation $\hat{T}$,

$$\langle A \rangle = \sum_n f_n \langle \tilde{\psi}_n | \tilde{A} | \tilde{\psi}_n \rangle. \tag{2.35}$$

In the case of local operators, the pseudo operator is expressed as:

$$\begin{aligned} \tilde{A} &= \hat{T}^{\dagger} A \hat{T} \\ &= A + \sum_{i,j} |\tilde{p}_i\rangle \left(\langle \phi_i | A | \phi_j \rangle - \langle \tilde{\phi}_i | A | \tilde{\phi}_j \rangle \right) \langle \tilde{p}_j |. \end{aligned} \tag{2.36}$$

Indeed, for nonlocal operators an additional term ΔA is added to the expression:

$$\Delta A = \sum_i |\tilde{p}_i\rangle (\langle \phi_i | - \langle \tilde{\phi}_i |) A (1 - \sum_j |\tilde{\phi}_j\rangle \langle \tilde{p}_j |) + (1 - |\tilde{p}_j\rangle \langle \tilde{\phi}_j |) A (|\phi_i\rangle - |\tilde{\phi}_i\rangle) \langle \tilde{p}_i |. \tag{2.37}$$

2.3.3 Charge density

In DFT the charge density is obviously a very important quantity where all observables are calculated being functionals of it. In fact, to obtain the charge density at a point $\mathbf{r}$ in space, the expectation value of the real space projection operator $|\mathbf{r}\rangle\langle\mathbf{r}|$ must be determined:

$$n(\mathbf{r}) = \sum_n f_n \langle \psi_n | \mathbf{r} \rangle \langle \mathbf{r} | \psi_n \rangle. \tag{2.38}$$

According to Eq.2.36 , $n(\mathbf{r})$ is written as:

$$n(\mathbf{r}) = \tilde{n}(\mathbf{r}) + n^1(\mathbf{r}) - \tilde{n}^1(\mathbf{r}), \tag{2.39}$$

where

$$\tilde{n}(\mathbf{r}) = \sum_n f_n \langle \tilde{\psi}_n | \mathbf{r} \rangle \langle \mathbf{r} | \tilde{\psi}_n \rangle, \tag{2.40}$$

and

$$n^1(\mathbf{r}) = \sum_{i,j,n} f_n \langle \tilde{\psi}_n | \tilde{p}_i \rangle \langle \phi_i | \mathbf{r} \rangle \langle \mathbf{r} | \phi_j \rangle \langle \tilde{p}_j | \tilde{\psi}_n \rangle, \tag{2.41}$$

and

$$\tilde{n}^1(\mathbf{r}) = \sum_{i,j,n} f_n \langle \tilde{\psi}_n | \tilde{p}_i \rangle \langle \tilde{\phi}_i | \mathbf{r} \rangle \langle \mathbf{r} | \tilde{\phi}_j \rangle \langle \tilde{p}_j | \tilde{\psi}_n \rangle. \tag{2.42}$$

In other words, a smooth pseudo core density is constructed which is identical to the core density outside the augmentation region and has a smooth continuation inside, such that n^1 contains the core states contribution while $\tilde{n}$ and $\tilde{n}^1$ contain the contribution of the pseudo core states.

2.3.4 Total energy

In the DFT, the total energy of a system which is the expectation value of total Hamiltonian is given by:

$$\begin{aligned} E[n] =& \frac{1}{2} \sum_n f_n \langle \psi_n | -\nabla^2 | \psi_n \rangle + \frac{1}{2} \int d^3r d^3r' \frac{[n(\mathbf{r}) + n^Z(\mathbf{r})][n(\mathbf{r}') + n^Z(\mathbf{r}')]}{|\mathbf{r} - \mathbf{r}'|} \\ &+ \int d^3r n(\mathbf{r}) \epsilon_{xc}(n(\mathbf{r})). \end{aligned} \tag{2.43}$$

This expression contains, respectively, the terms resembling: the kinetic energy of the electrons, the Coulomb interaction among the charges i.e. electrons and nuclei (Z), and the exchange-correlation energy.

Based on the PAW formalism, the energy expression can be rewritten in the form:

$$E = \tilde{E} + E^1 - \tilde{E}^1. \tag{2.44}$$

$\tilde{E}$ is the smooth part which is evaluated on regular grids in the real or Fourier space while E^1 and $\tilde{E}^1$ are sum of atomic contributions evaluated on radial grids in angular momentum representation.

On these bases, the decomposition of the terms in the total energy expression are described below.

1. The kinetic energy is written as:

$$E_k = \tilde{E}_k + E_k^1 - \tilde{E}_k^1, \tag{2.45}$$

where

$$\tilde{E}_k = \frac{1}{2}\sum_n f_n \langle\tilde{\psi}_n| - \nabla^2|\tilde{\psi}_n\rangle, \tag{2.46}$$

and

$$E_k^1 = \frac{1}{2}\sum_{i,j,n} f_n \langle\tilde{\psi}_n|\tilde{p}_i\rangle\langle\phi_i| - \nabla^2|\phi_j\rangle\langle\tilde{p}_j|\tilde{\psi}_n\rangle, \tag{2.47}$$

and

$$\tilde{E}_k^1 = \frac{1}{2}\sum_{i,j,n} f_n \langle\tilde{\psi}_n|\tilde{p}_i\rangle\langle\tilde{\phi}_i| - \nabla^2|\tilde{\phi}_j\rangle\langle\tilde{p}_j|\tilde{\psi}_n\rangle. \tag{2.48}$$

2. The exchange-correlation energy is obtained straightforward using the previously shown decomposition of the charge density in Eq.(2.39):

$$\begin{aligned} E_{xc} &= \tilde{E}_{xc} + E_{xc}^1 - \tilde{E}_{xc}^1 \\ &= \int d^3r\tilde{n}(\mathbf{r})\epsilon_{xc}(n(\mathbf{r})) + \int d^3rn^1(\mathbf{r})\epsilon_{xc}(n^1(\mathbf{r})) - \int d^3r\tilde{n}^1(\mathbf{r})\epsilon_{xc}(\tilde{n}^1(\mathbf{r})) \end{aligned} \tag{2.49}$$

3. The Hartree term is both nonlocal and nonlinear, which requires more care while introducing the PAW transformation into its expression. To this extent, a compensation charge density $\hat{n}$ which is localized in the augmentation region is introduced to treat the long range interaction between the charges within the augmentation region and those outside. In fact, this compensation charge density is added to pseudo charge density and its one-center expansion such that the difference between the all-electron and pseudo one-center contributions to the charge density has vanishing electrostatic multipole moments. Thus, the total charge density is expressed as:

$$n + n^Z = (\tilde{n} + \hat{n}) + (n^1 + n^Z) - (\tilde{n}^1 + \hat{n}) \tag{2.50}$$

The compensation charge density is given as a summation of atomic contributions $\hat{n} = \sum_a \hat{n}^a$ where:

$$\hat{n}^a(\mathbf{r}) = \sum_L Q_L^a g_L^a(\mathbf{r}). \tag{2.51}$$

The function g_L^a is localized within the augmentation region and expressed as generalized Gaussians:

$$g_L^a(\mathbf{r}) = C_l|\mathbf{r} - \mathbf{R}^a|^l Y_L(\mathbf{r} - \mathbf{R}^a)e^{-(\frac{|\mathbf{r}-\mathbf{R}^a|}{r_c^a})^2}, \tag{2.52}$$

where the normalization constant C_l is determined such that its multipole moment is unity:

$$\int d^3r|\mathbf{r}-\mathbf{R}^a|^l Y_L(\mathbf{r}-\mathbf{R}^a) g_L^a(\mathbf{r}-\mathbf{R}^a) = 1, \tag{2.53}$$

and Y_L is a spherical harmonic function with $L = (l, m)$ being the angular momenta in spherical harmonics expansion while $\mathbf{R}^a$ stands for the nuclear positions. The multipole moments are given by:

$$Q_L^a = \int d^3r|\mathbf{r}-\mathbf{R}^a|^l Y_L^*(\mathbf{r}-\mathbf{R}^a)[n^{a,1}(\mathbf{r}) + n^{a,Z}(\mathbf{r}) - \tilde{n}^{a,1}(\mathbf{r})]. \tag{2.54}$$

To obtain the expression of the Hartree energy, one should evaluate the following term as:

$$\begin{aligned}
[n(\mathbf{r}) + n^Z(\mathbf{r})][n(\mathbf{r}') + n^Z(\mathbf{r}')] = {} & [\tilde{n}(\mathbf{r}) + \hat{n}(\mathbf{r})][\tilde{n}(\mathbf{r}') + \hat{n}(\mathbf{r}')] \\
& + [n^{(1)}(\mathbf{r}) + n^Z(\mathbf{r})][n^{(1)}(\mathbf{r}') + n^Z(\mathbf{r}')] \\
& - [\tilde{n}^{(1)}(\mathbf{r}) + \hat{n}(\mathbf{r})][\tilde{n}^{(1)}(\mathbf{r}') + \hat{n}(\mathbf{r}')] \\
& + [n^{(1)}(\mathbf{r}) + n^Z(\mathbf{r}) - \tilde{n}^{(1)}(\mathbf{r}) - \hat{n}(\mathbf{r})][\tilde{n}(\mathbf{r}) - \tilde{n}^{(1)}(\mathbf{r})] \\
& + [n^{(1)}(\mathbf{r}') + n^Z(\mathbf{r}') - \tilde{n}^{(1)}(\mathbf{r}') - \hat{n}(\mathbf{r}')][\tilde{n}(\mathbf{r}') - \tilde{n}^{(1)}(\mathbf{r}')].
\end{aligned} \tag{2.55}$$

Indeed, $\tilde{n} = \tilde{n}^{(1)}$ within the augmentation region while $n^{(1)} = \tilde{n}^{(1)}$ and $n^Z = \hat{n}$ outside the augmentation region. Consequently, equation simplifies into:

$$\begin{aligned}
[n(\mathbf{r}) + n^Z(\mathbf{r})][n(\mathbf{r}') + n^Z(\mathbf{r}')] = {} & [\tilde{n}(\mathbf{r}) + \hat{n}(\mathbf{r})][\tilde{n}(\mathbf{r}') + \hat{n}(\mathbf{r}')] \\
& + [n^{(1)}(\mathbf{r}) + n^Z(\mathbf{r})][n^{(1)}(\mathbf{r}') + n^Z(\mathbf{r}')] \\
& - [\tilde{n}^{(1)}(\mathbf{r}) + \hat{n}(\mathbf{r})][\tilde{n}^{(1)}(\mathbf{r}') + \hat{n}(\mathbf{r}')].
\end{aligned} \tag{2.56}$$

Thus, the three components of the Hartree energy term are:

$$\tilde{E}_H = \frac{1}{2}\int d^3r d^3r' \frac{[\tilde{n}(\mathbf{r}) + \hat{n}(\mathbf{r})][\tilde{n}(\mathbf{r}') + \hat{n}(\mathbf{r}')]}{|\mathbf{r}-\mathbf{r}'|} \tag{2.57}$$

$$E_H^{(1)} = \frac{1}{2}\int d^3r d^3r' \frac{[n^{(1)}(\mathbf{r}) + n^Z(\mathbf{r})][n^{(1)}(\mathbf{r}') + n^Z(\mathbf{r}')]}{|\mathbf{r}-\mathbf{r}'|} \tag{2.58}$$

$$\tilde{E}_H^{(1)} = \frac{1}{2}\int d^3r d^3r' \frac{[\tilde{n}^{(1)}(\mathbf{r}) + \hat{n}(\mathbf{r})][\tilde{n}^{(1)}(\mathbf{r}') + \hat{n}(\mathbf{r}')]}{|\mathbf{r}-\mathbf{r}'|} \tag{2.59}$$

Summing up all the energy contributions , the Kohn-Sham total energy can be separated into a part calculated on smooth functions and some atomic corrections involving quantities localized around the nuclei. Indeed, both the forces and the Hamiltonian can be derived from the total energy functional which is discussed in the following subsections.

2.3.5 The transformed Kohn-Sham equation

In the PAW formalism, the pseudo wave function is the variational quantity from which other quantities are determined. To obtain the pseudo wave function one needs to solve the eigenvalue equation:

$$\tilde{H}\tilde{\psi}_n(\mathbf{r}) = \epsilon_n \tilde{O}\tilde{\psi}_n(\mathbf{r}). \tag{2.60}$$

2.3.5.1 Overlap operator

In the all-electron representation, the overlap matrix is given by the matrix elements of the unity operator:

$$O_{ij} = \langle i|j\rangle. \tag{2.61}$$

Besides, the all-electron wave function is characterized by the following orthogonality relation:

$$\langle \psi_n|\psi_m\rangle = \delta_{n,m}. \tag{2.62}$$

However, in the pseudo representation and using Eq.(2.36), the unity operator transforms to a nonlocal operator of the form:

$$\tilde{O} = 1 + \sum_{i,j} |\tilde{p}_i^a\rangle[\langle\phi_i^a|\phi_j^a\rangle - \langle\tilde{\phi}_i^a|\tilde{\phi}_j^a\rangle]\langle\tilde{p}_j^a|. \tag{2.63}$$

Indeed, the pseudo overlap operator differs from unity but it reduces to unity if the norm-conserving condition is imposed ($\langle\phi_i^a|\phi_j^a\rangle = \langle\tilde{\phi}_i^a|\tilde{\phi}_j^a\rangle$).

2.3.5.2 Hamiltonian Operator

The Hamiltonian operator is determined as the first derivative of the total energy functional with respect to the density operator. Meanwhile, the pseudo Hamiltonian operator is constructed from the pseudo density operator $\tilde{\rho}$ as:

$$\tilde{H} = \frac{\partial E}{\partial \tilde{\rho}}, \tag{2.64}$$

with,

$$\tilde{\rho} = \sum_n f_n |\tilde{\psi}_n\rangle\langle\tilde{\psi}_n|, \tag{2.65}$$

where the pseudo wave functions obey the orthogonality condition. To obtain the pseudo Hamiltonian, the transformation is straight forward for the local parts of the Hamiltonian. To determine the nonlocal part, we make use of:

$$\frac{\partial E}{\partial\langle\tilde{\psi}_n|} = f_n \tilde{H}|\tilde{\psi}_n\rangle, \tag{2.66}$$

to write down the expression of the pseudo Hamiltonian:

$$\tilde{H} = -\frac{1}{2}\nabla^2 + \tilde{V}_{eff}(\mathbf{r}) + \sum_{a,i,j} |\tilde{p}_i^a\rangle D_{ij}^a \langle\tilde{p}_j^a|, \tag{2.67}$$

where the last term resembles the nonlocal part of the pseudo Hamiltonian while

$$\tilde{V}_{eff}(r) = V_H[\tilde{n} + \tilde{n}^{a,Z}] + V_{xc}[\tilde{n}]. \tag{2.68}$$

is the local part of the potential.

2.3.6 Forces

In the ground state, the forces on each nucleus $\mathbf{F}^a$ can be calculated as the derivative of the total energy with respect to the atomic position $\mathbf{R}^a$:

$$\begin{aligned}\mathbf{F}^a &= -\frac{dE}{d\mathbf{R}^a} \\ &= -\left(\frac{\partial E}{\partial \mathbf{R}^a}\right)_{\tilde{\psi}} - \left[\sum_n \left(\frac{\partial E}{\partial|\tilde{\psi}_n\rangle}\right)_{\mathbf{R}^b} \left(\frac{\partial|\tilde{\psi}_n\rangle}{\partial \mathbf{R}^a}\right)_{\mathbf{R}^b} + h.c.\right],\end{aligned} \tag{2.69}$$

where $h.c$ denotes the hermitian conjugate. While the second term is purely of quantum origin, the first term represents the variation of the total energy for an infinitesimal displacement of the atomic position $\mathbf{R}^a$ and is written as:

$$\left(\frac{\partial E}{\partial \mathbf{R}^a}\right)_{\tilde{\psi}} = \sum_n f_n \langle\tilde{\psi}_n|\nabla^a \tilde{H}|\tilde{\psi}_n\rangle. \tag{2.70}$$

In fact, the forces resulting from an infinitesimal change in the wave functions due to the displacement of atomic positions are called Pulay forces that resemble the forces on the electrons that are dragged along with the nucleus due to the position-dependent basis-set. Within the frozen core approximation employed in the PAW method, one should consider both the Pulay forces from the frozen-core electrons that shift rigidly with the nucleus as well as the contribution from the augmentation region. Besides, an infinitesimal change in the atomic positions is necessarily accompanied by a change in the wave functions which restores the orthogonality. However, the new occupied wave functions are required to span the same portion of the Hilbert space that was occupied before the atomic displacement such that the new wave function can be expressed as a linear combination of the pseudo wave functions with the undisplaced atomic positions:

$$|\tilde{\psi}_n(\mathbf{R}^a + d\mathbf{R}^a)\rangle = |\tilde{\psi}_n(\mathbf{R}^a)\rangle + \sum_m |\tilde{\psi}_m(\mathbf{R}^a)\rangle \mathbf{\Lambda}_{nm} d\mathbf{R}^a. \tag{2.71}$$

$\mathbf{\Lambda}_{nm}$ is matrix composed of a hermitian $\mathbf{h}_{nm}$ and an antihermitian part $\mathbf{a}_{nm}$ such that:

$$\begin{aligned} \mathbf{\Lambda}_{nm} &= \mathbf{h}_{nm} + \mathbf{A}_{nm} n \\ \mathbf{h}_{nm} &= \frac{1}{2}(\mathbf{\Lambda}_{nm} + \mathbf{\Lambda}^{\dagger}_{nm}) \\ \mathbf{A}_{nm} &= \frac{1}{2}(\mathbf{\Lambda}_{nm} - \mathbf{\Lambda}^{\dagger}_{nm}) \end{aligned} \tag{2.72}$$

Indeed, the orthogonality condition to linear order in the displacement $d\mathbf{R}^a$ applies to the new wave functions:

$$\langle\tilde{\psi}_n(\mathbf{R}^a + d\mathbf{R}^a)|\tilde{O}(\mathbf{R}^a + d\mathbf{R}^a)|\tilde{\psi}_m(\mathbf{R}^a + d\mathbf{R}^a)\rangle = \delta_{nm}, \tag{2.73}$$

where

$$\tilde{O}(\mathbf{R}^a + d\mathbf{R}^a) = \tilde{O}(\mathbf{R}^a) + \left(\frac{\partial \tilde{O}(\mathbf{R}^a)}{\partial \mathbf{R}^a}\right) d\mathbf{R}^a. \tag{2.74}$$

Consequently, the hermitian part of the matrix $\mathbf{\Delta}_{nm}$ is written as:

$$\mathbf{h}_{nm} = -\frac{1}{2}\langle\tilde{\psi}_n(\mathbf{R}^a)| \left(\frac{\partial \tilde{O}(\mathbf{R}^a)}{\partial \mathbf{R}^a}\right) |\tilde{\psi}_m(\mathbf{R}^a)\rangle. \tag{2.75}$$

Hence, the derivative of the wave function with respect to the atomic positions can be expressed as:

$$\frac{\partial|\tilde{\psi}_n\rangle}{\partial \mathbf{R}^a} = -\frac{1}{2}\sum_m |\tilde{\psi}_m(\mathbf{R}^a)\rangle\langle\tilde{\psi}_m(\mathbf{R}^a)| \left(\frac{\partial \tilde{O}(\mathbf{R}^a)}{\partial \mathbf{R}^a}\right) |\tilde{\psi}_n(\mathbf{R}^a)\rangle + \sum_m |\tilde{\psi}_m(\mathbf{R}^a)\rangle A_{nm}. \tag{2.76}$$

Besides,

$$\left(\frac{\partial E}{\partial|\tilde{\psi}_n\rangle}\right)_{R^a} = f_n\langle\tilde{\psi}_n|\tilde{H}. \tag{2.77}$$

Therefore, the expression of the total force including the force on the nucleus and the Pulay force becomes:

$$\begin{aligned}\mathbf{F}^a = & -\sum_n f_n\langle\tilde{\psi}_n|\nabla^a\tilde{H}|\tilde{\psi}_n\rangle + \sum_{n,m}\frac{f_n - f_m}{2}A_{nm}\langle\tilde{\psi}_n|\tilde{H}|\tilde{\psi}_m\rangle \\ & + \sum_{n,m}\frac{f_n + f_m}{2}\langle\tilde{\psi}_m|\frac{\partial\tilde{O}(\mathbf{R}^a)}{\partial\mathbf{R}^a}|\tilde{\psi}_n\rangle\langle\tilde{\psi}_n|\tilde{H}|\tilde{\psi}_m\rangle.\end{aligned} \tag{2.78}$$

2.4 Conclusion

In this chapter, we have provided a short review of the density functional theory and we elaborate on the projector augmented wave (PAW) method which is used in the framework of this thesis to calculate the electronic structure. In fact, the PAW method bridges the gap between the augmented wave methods and the pseudopotential methods and underscores the relation between these two approaches. It is capable of handling even the most difficult case, such as strong magnetic moments and large electronegativity differences, with remarkable precision [Kresse 1999] which proves its reliability and efficiency in electronic structure calculations. In this work, we have used the PAW formalism as implemented in Vienna *ab initio* simulation package (VASP).

Chapter 3

Relativistic effects

Contents

3.1 Introduction

Despite its wide applicability in determining the electronic structure of most materials, the non-relativistic density functional theory remains insufficient to explain many phenomena related to magnetism and optical properties. One prominent example is the position of the optical absorption edge of gold [Christensen 1971]. In fact, relativistic effects, in particular spin-orbit coupling (SOC), influence the electronic structure of magnetic solids giving rise to a variety of effects such as the magneto-optical Kerr effect, Faraday effect, and magnetic dichroism [Schutz 1987]. Those phenomena are the consequences of the lowered symmetry and the lifted energetic degeneracies caused by coupling the spin and orbital degrees of freedom. Besides, including spin-orbit interactions adds an orbital contribution to the magnetic moment [Ebert 1988] where the scalar product of the spin and orbital moment involves the presence of an angle between the crystallographic and the magnetization axis. This gives rise to the phenomena of magneto-crystalline anisotropy, which is the dependence of the energy on the magnetization orientation.

To incorporate relativistic effects into electronic structure calculations, quantum electrodynamics supplies a proper framework for a relativistically consistent density functional theory based on Dirac equation. Nevertheless, for many cases it is well justified to deal with relativistic effects by introducing corrections to the Schrödinger equation using the second variational technique. In this chapter we give a brief review of the relativistic density functional theory and the scalar relativistic approximation for the spin orbit coupling. Then, we define the magnetocrystalline anisotropy and the ways of treating it; special attention is paid to the force theorem.

3.2 Relativistic density functional theory

In fully relativistic calculations, the Dirac equation is employed where the spin angular momentum and its coupling to the orbital angular momentum arises naturally. By constructing a set of 4 × 4 matrices, Dirac was able to construct a relativistic energy operator and to outline its properties. In relativistic DFT, one solves the following Kohn-Sham-Dirac equation [Rajagopal 1973]:

$$\left[c\alpha.\left(\frac{\hbar}{i}\nabla+\frac{e}{c}\mathbf{A}_{eff})\right)+\beta mc^2+V_{eff}(r)\right]\psi_i(r)=\varepsilon_i\psi_i(r) \tag{3.1}$$

where $\psi_i(r)$ is the four-component Dirac wave function with the corresponding single-particle energies ε_i. The α matrix is a defined to be $\alpha=\alpha_x\hat{x}+\alpha_y\hat{y}+\alpha_z\hat{z}$ where:

$$\alpha_x=\begin{pmatrix}0&\sigma_x\\ \sigma_x&0\end{pmatrix}\quad \alpha_y=\begin{pmatrix}0&\sigma_y\\ \sigma_y&0\end{pmatrix}\quad \alpha_z=\begin{pmatrix}0&\sigma_z\\ \sigma_z&0\end{pmatrix} \tag{3.2}$$

where the two-component Pauli matrices are defined as:

$$\sigma_x=\begin{pmatrix}0&1\\ 1&0\end{pmatrix}\quad \sigma_y=\begin{pmatrix}0&-i\\ i&0\end{pmatrix}\quad \sigma_z=\begin{pmatrix}1&0\\ 0&-1\end{pmatrix} \tag{3.3}$$

The β Dirac matrix is scalar defined as:

$$\beta=\begin{pmatrix}\mathbf{I}_2&0\\ 0&-\mathbf{I}_2\end{pmatrix}\quad where\quad I_2=\begin{pmatrix}1&0\\ 0&1\end{pmatrix} \tag{3.4}$$

In fact, the effective scalar V_{eff} and vector potential $\mathbf{A}_{eff}$ are expressed as:

$$V_{eff}=-e\left[A^0_{ext}(r)+\frac{1}{c}\int d^3r'\frac{J^0(r')}{|r-r'|}+c\frac{\partial E_{xc}[J^\mu]}{\partial J^0(r)}\right] \tag{3.5}$$

$$A_{eff} = -e\left[A_{ext}(r) + \frac{1}{c}\int d^3r'\frac{J(r')}{|r-r'|} + c\frac{\partial E_{xc}[\mathbf{J}^\mu]}{\partial \mathbf{J}(r)}\right]. \tag{3.6}$$

Obviously, the central quantity that determines the properties of the system is the four-component current J^μ which is defined by:

$$J^0 = -ec\sum_i \psi_i^\dagger \psi_i \tag{3.7}$$

$$J^\mu = -ec\sum_i \psi_i^\dagger \beta\alpha^\mu \psi_i \tag{3.8}$$

where J^0/c is identical to the usual electronic charge density ρ while the other components J^μ give the spatial components of the electronic current density. To simplify this general scheme, an approximate relativistic approach is usually employed by performing the Gordon decomposition of the spatial current density into its orbital and spin parts [Eschrig 1985, Ebert 2000]:

$$\mathbf{J} = \frac{1}{2m}\psi^\dagger\beta[-i\overleftarrow{\nabla} + i\nabla + 2e\mathbf{A}]\psi + \frac{1}{2m}\nabla\psi^\dagger\beta\sigma\psi \tag{3.9}$$

The first term in Eq.(3.9) represents the orbital current density while the second is the spin current density. The spin current density is the current of a corresponding spin magnetization density $\mathbf{m}$ defined as:

$$\mathbf{m} = -\mu_B\sum_i \psi_i^\dagger\beta\sigma\psi_i \tag{3.10}$$

In fact, one can see that the spin dependent DFT arises naturally from the general four-current Kohn-Sham-Dirac equation, as by ignoring the orbital current density contribution one arrives at an equation that is analogous to the non-relativistic spin dependent DFT Schrödinger equation.

3.3 Scalar relativistic approximation and SOC

Accounting for SOC in a full-relativistic calculation is quite computer demanding. However, this difficulty can be avoided by exploiting the fact that SOC is generally a small effect, especially in light elements, which provides the possibility of treating it by perturbation theory. In fact, the second variational method for relativistic calculations is derived from the scalar relativistic approximation as proposed by Koelling and Harmon [Koelling 1977]. Thus, as a first step, the scalar relativistic bands where SOC is neglected should be calculated.

In the scalar relativistic approximation, the Kohn-Sham-Dirac Eq.(3.1) is solved considering the potential to be spherical V(r). The solution is a four-component spinor of the form:

$$\psi = \begin{pmatrix} g_\kappa(r)\chi_{\kappa\mu} \\ if_\kappa(r)\chi_{-\kappa\mu} \end{pmatrix} \tag{3.11}$$

where $f_\kappa(r)$ and $g_\kappa(r)$ satisfy the following coupled radial equations:

$$\begin{aligned} c\left(\tfrac{df_\kappa}{dr} + \tfrac{1-\kappa}{r} f_\kappa\right) &= -(\varepsilon - V - mc^2) g_\kappa \\ c\left(\tfrac{dg_\kappa}{dr} + \tfrac{1+\kappa}{r} g_\kappa\right) &= (\varepsilon - V + mc^2) f_\kappa \end{aligned} \tag{3.12}$$

$\chi_{\kappa\mu}$ are spherical spinors that are analogous to the spherical harmonics where κ represents the relativistic quantum number giving both l and j and its the eigenvalue of $\mathbf{K}$ defined by:

$$\mathbf{K} = \begin{pmatrix} \sigma \cdot \mathbf{L} + 1 & 0 \\ 0 & -(\sigma \cdot \mathbf{L} + 1) \end{pmatrix} \tag{3.13}$$

Using the coupled equations in Eq.(3.12), we arrive at:

$$\begin{aligned} -\frac{\hbar^2}{2Mr^2}\frac{d}{dr}\left(r^2\frac{dg_\kappa}{dr}\right) + [V + \frac{h^2\kappa(\kappa+1)}{2Mr^2} g_\kappa - \frac{h^2}{4M^2c^2}\frac{dV}{dr}\frac{dg_\kappa}{dr} \\ - \frac{h^2}{4M^2c^2}\frac{dV}{dr}\frac{1+\kappa}{r} g_\kappa = (\varepsilon - mc^2) g_\kappa \end{aligned} \tag{3.14}$$

where $M = m + \frac{\varepsilon - mc^2 - V}{2c^2}$. Since $\kappa(\kappa+1) = l(l+1)$, the first two terms in Eq.(3.14) will resemble the non-relativistic contribution, while the third term is the Darwin term. Indeed, the last term is the only one that depends on the sign of κ and it represents the spin-orbit interaction. The scalar-relativistic approximation removes this term so that to obtain an orbital equation which is decoupled from the spin and thus keeping the spin as a good quantum number.

After solving the scalar relativistic equation with the SOC term dropped, a second variational secular equation is set up using the lowest scalar relativistic orbitals as basis functions. Further, in the second variation bases, the overlap S is diagonal and the Hamiltonian is just the SOC term plus the scalar relativistic eigenvalues on the diagonal:

$$H_{ij} = \varepsilon_i \delta_{ij} + H_{ij}^{SO} \tag{3.15}$$

where i and j indices run over spins and the bands that are included in the second variation while $S_{ij} = \delta_{ij}$ for the low lying bands. Moreover, the spin-orbit contribution to the Hamiltonian is expressed as:

$$H^{SO} = \frac{\hbar^2}{2M^2c^2}\frac{1}{r}\frac{dV}{dr}\mathbf{L}\cdot\sigma \tag{3.16}$$

This term is straightforward to calculate in the second variational basis since it originates deep in the core near the nucleus (where $\frac{1}{r}\frac{dV}{dr}$ is large). As a consequence, it is negligible outside the augmentation region, while inside it can be, to a very good approximation, calculated as if the atoms where spherical.

3.4 Magneto-crystalline anisotropy

Magneto-crystalline anisotropy is one of the most important intrinsic properties of magnetic materials from both a technological and fundamental point of view. In fact, magnetic materials exhibit intrinsic easy and hard directions of the magnetization with respect to the crystalline axis and the external shape of the body. The preferred orientation of the magnetization is determined by the magneto-crystalline anisotropy energy (MAE) which is the change in the free energy upon rotation of magnetization. MAE is typically of the order of 10^{-6} to 10^{-3} eV/atom thus it is a very small correction to the total magnetic energy [Bruno 1993]. It actually arises form the relativistic corrections to the Hamiltonian which breaks the rotational invariance with respect to the spin quantization axis. The magneto-crystalline anisotropy originates from spin-orbit coupling while the shape anisotropy energy originates from dipole-dipole interaction present in the Breit term [Jansen 1988].

Following the proposal of van Vleck [Vleck 1937] that spin orbit coupling induces magneto-crystalline anisotropy, many calculations, pioneered by Brooks [Brooks 1940] and Fletcher [Fletcher 1954], have been done using simplified tight-binding and perturbation methods to calculate the MAE for Fe and Ni. Later, calculations were based on more realistic electronic structures using the precise first principle methods [Daalderop 1990]. Indeed, since MAE is usually a very tiny quantity which is often calculated by subtracting two energy values, it is thus quite sensitive to fine electronic structures and requires careful convergence tests of the k-mesh and basis sets. Besides, the exchange-correlation functionals influence the MAE values [Trygg 1995, Yang 2001].

While the SOC can be dealt with by either the four-component full-relativistic scheme or second variational procedure, calculating the MAE can be done by three different methods: total energy, force theorem, or the torque method [Wang 1996b]. In the framework of this thesis, we have used the first two methods to calculate the MAE. As the calculation of the full-relativistic total energies is quite computationally demanding, the use of the force theorem becomes reasonable considering the fact of the usually weak SOC in $3d$ transition metals. An overview of the force theorem is given in the following paragraph.

3.4.1 The Force theorem

The force theorem, as proposed in [Weinert 1985, Wang 1996a], relates small changes in the total energy to changes in the eigenvalues upon the variation of the magnetization orientation. This assumption is based on scalar relativistic treatment of SOC beside a frozen-potential approximation. In this later, the same potential is used in different calculations for different magnetization orientation to obtain the respective eigenvalue sums.
For an unperturbed system the total energy is expressed as:

$$E = T_0[n(\mathbf{r})] + \int d\mathbf{r} V_{ext}(\mathbf{r}) n(\mathbf{r}) + \int d^3\mathbf{r} d^3\mathbf{r}' \frac{n(\mathbf{r}) \cdot n(\mathbf{r}')}{|\mathbf{r} - \mathbf{r}'|} + E_{xc}[n(\mathbf{r})] \tag{3.17}$$

In scalar relativistic treatment, SOC is considered a perturbation that is introduced as a change in the total energy to the first order in the charge density:

$$\begin{aligned} \delta E =& \delta T_0[n(\mathbf{r})] + \int d^3\mathbf{r} V_{ext}(\mathbf{r}) \delta n(\mathbf{r}) + \int d^3\mathbf{r} d^3\mathbf{r}' \frac{n(\mathbf{r}) \cdot \delta n(\mathbf{r}')}{|\mathbf{r} - \mathbf{r}'|} \\ &+ \int d^3\mathbf{r} \varepsilon_{xc}[n(\mathbf{r})] \delta n(\mathbf{r}) + O(\delta n^2) \end{aligned} \tag{3.18}$$

Meanwhile, the total Kohn-Sham potential V_{eff} can be written as:

$$V_{eff} = V_{ext} + V_H + V_{xc} \tag{3.19}$$

where $V_{xc}(\mathbf{r}) = n(\mathbf{r}) \frac{\delta \varepsilon_{xc}[n(\mathbf{r})]}{\delta n(\mathbf{r})} + \varepsilon_{xc}[n(\mathbf{r})]$. Indeed, according to the Kohn-Sham equations the kinetic energy term can be expressed in terms of the one-particle energies ε_i as follows:

$$T_0[n(\mathbf{r})] = \sum_i \varepsilon_i - \int d^3\mathbf{r} V_{eff}(\mathbf{r}) n(\mathbf{r}) \tag{3.20}$$

Thus, one obtains:

$$\delta T_0[n(\mathbf{r})] = \delta \sum_i \varepsilon_i - \int d^3\mathbf{r}\delta V_{eff}(\mathbf{r})n(\mathbf{r}) - \int d^3\mathbf{r}V_{eff}(\mathbf{r})\delta n(\mathbf{r}) \tag{3.21}$$

As mentioned before, the force theorem exploits the frozen potential approximation so that the expression of the perturbed energy simplifies to:

$$\delta E = \delta \sum_i \varepsilon_i \tag{3.22}$$

Consequently, the force theorem allows to obtain the total energy difference, in other words the MAE, as the difference between the sum of one-particle energies. The usual procedure for calculating MAE within the force theorem is to perform a self-consistent spin-polarized calculation for the scalar relativistic Hamiltonian followed by non self-consistent calculations including SOC for different magnetization orientations and finally taking the difference between the sums of the one-particle eigenvalues. Results reported on several materials have shown that the force theorem is reliable for evaluating MAE [Daalderop 1990, Daalderop 1991].

3.5 Conclusion

Small corrections to the Hamiltonian give rise to the important property of magnetic anisotropy. MAE is very subtle and depends on the band structure of the material in a complicated manner which makes its calculation difficult. Besides, its tiny values require high accuracy in the total energy calculations. In this respect, the force theorem provides a feasible method to evaluate MAE. Indeed, a better understanding of magnetic anisotropy beyond bare numbers requires investigating related quantities such as the orbital moment which is in turn due to SOC. In this sense, Bruno has demonstrated, using the second perturbation, that MAE is proportional to the orbital moment anisotropy [Bruno 1989]. His model works well for strong ferromagnets like Co where the spin up channel is completely occupied while later Wang [D.Wang 1993] and van der Laan [van der Laan 1998] derived a more exact model considering spin-flip processes. In this thesis, we explore the magnetic anisotropy of the bulk magnetoelectric GFO and MnPc/Co interface.

Chapter 4

Electronic, magnetic, and optical properties of Gallium ferrite

Contents

4.1 Introduction

Magnetoelectric materials, coupling both magnetic and electric properties, have received growing interests motivated by the possibility of integrating them in potential technological devices. Indeed, a few materials have been reported to exhibit a sizable magnetoelectric effect, among which $Ga_{2-x}Fe_xO_3$

(GFO) appears to be of considerable significance due to its features demonstrated experimentally; being ferrimagnetic at room temperature and exhibiting a large linear magnetoelectric effect. In the context of a better understanding of these properties, we have performed an ab-initio study, within different levels of approximation and including spin-orbit coupling, to investigate the electric, magnetic, anisotropy, and optical properties of bulk GFO with different iron concentrations. In the first part, we proceed by giving an overview that introduces GFO and its well-known properties and in the second part we show and discuss the results on the impact of the Fe concentration on the different properties of GFO. The third part addresses the optical properties where the basic theory is described followed by the optical properties of GFO. In particular, we show that the optical properties provide a good tool to determine the cationic site occupation in GFO which is proven to accommodate a high percentage of site disorder.

4.2 GFO the magnetoelectric ferrimagnet: An overview

The first Gallium ferrite crystals, $Ga_{2-x}Fe_xO_3$ with $0.7 \leq x \leq 1.4$, were synthesized by Remeika [Remeika 1960] who introduced it as a ferromagnetic piezoelectric material. Later, the structural characterization was preliminary determined by Wood and then confirmed by Abrahams *et al.* [Abrahams 1965]. GFO crystallizes in the orthorhombic space group $Pc2_1n$ with the following lattice parameters for $GaFeO_3$: $a = 0.87512 \pm 0.00008$ nm, $b = 0.93993 \pm 0.00003$ nm and $c = 0.50806 \pm 0.00002$ nm. The Fe and Ga cations occupy four different cationic sites: three irregular octahedral sites (Fe1, Fe2, Ga2), and a regular tetrahedral site oriented along b-axis: Ga1, while the O anions are positioned in six different sites forming a double hexagonal compact arrangement (*c.f.* Figure 4.1).

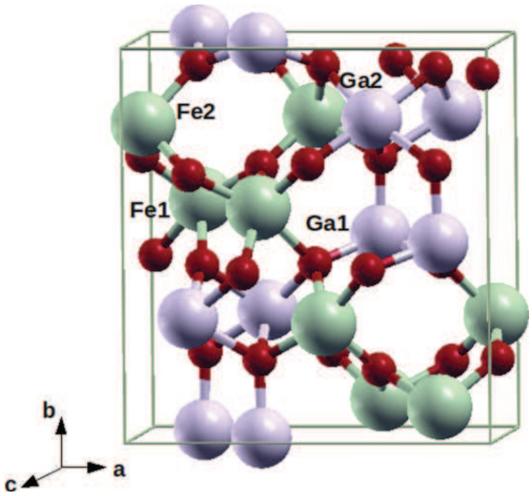

Figure 4.1: $GaFeO_3$ unit cell. Fe,Ga, and O atoms are represented by green, gray, and red balls respectively. The different atomic sites are also marked.

As for the magnetic order, Frankel *et al.* [Frankel 1965] were first to show the ferrimagnetic order in GFO using Mössbauer spectroscopy which was later confirmed by Bertaut *et al.* [Bertaut 2008] using neutron diffraction in addition. Ga1 and Fe1 sites are found to be antiferromagnetically coupled to Ga2 and Fe2 sites which in principle should result in an overall antiferromagnetism for $x = 1$. Nevertheless, a net magnetic moment is observed which proposes a possible existence of site disorder. An issue that was described in

Arima's *et al.* work [Arima 2004] which demonstrated a strong dependence of the magnetic properties of GFO on the Fe/Ga ratio that is in turn highly influenced by the preparation method. Indeed, the ferrimagnetism was interpreted as follows: the magnetic Fe cations occupying site Fe1 adopt magnetic moment which has antiparallel orientation to that of Fe cations positioned on sites Ga2 and Fe2 due to the super-exchange mechanism that favors an antiferromagnetic coupling. Besides, since the sum of Fe amount at the Fe2 and Ga2 sites is larger than the Fe amount on Fe1, antiferromagnetic alignment of the Fe moments causes the ferrimagnetic magnetization along the c-axis. Indeed, another interesting aspect of GFO, which has been demonstrated experimentally, is that its magnetic transition temperature could be tuned with the Fe/Ga ratio and increased with the Fe content to a value which is superior to room temperature for $x \geq 1.1$. Besides, a large linear magnetoelectric effect was measured for GFO single crystals which is larger by one order of magnitude than the value reported on Cr_2O_3.

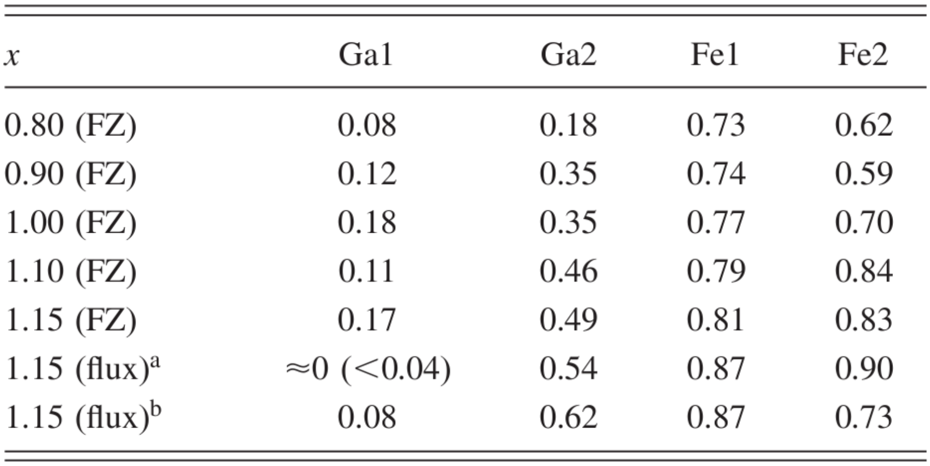

x	Ga1	Ga2	Fe1	Fe2
0.80 (FZ)	0.08	0.18	0.73	0.62
0.90 (FZ)	0.12	0.35	0.74	0.59
1.00 (FZ)	0.18	0.35	0.77	0.70
1.10 (FZ)	0.11	0.46	0.79	0.84
1.15 (FZ)	0.17	0.49	0.81	0.83
1.15 (flux)[a]	≈0 (<0.04)	0.54	0.87	0.90
1.15 (flux)[b]	0.08	0.62	0.87	0.73

Figure 4.2: Fe partial occupancies at the Ga1, Ga2, Fe1, and Fe2 sites as deduced by a Rietveld analysis of neutron powder diffraction of FZ-melt GFO samples at room temperature. The parameters for the flux-grown samples x=1.15 crystal are listed for comparison [Arima 2004] .

Despite several experimental reports investigating the properties of GFO, there are only few theoretical ones. Early theoretical first principle calculations reported on an ideal system revealed a stable antiferromagnetic state with a zero net spin and orbital moment [Han 2007]. More recently and based on previous x-ray and neutron diffraction experiments [Arima 2004] revealing cation site disorder in GFO, Roy *et al.* [Roy 2011] demonstrated that interchanged Fe and Ga cation sites is at the origin of altering the magnetic moments on the Fe sites thereby leading to the overall ferrimagnetism. Although this site disorder is not spontaneous at the ground state, it might be driven by thermal energy. This finding is consistent with experimental demonstrations that the magnetic properties of GFO are highly influenced by the preparation method [Arima 2004]. Although, to some extent, demonstrated experimentally [Arima 2004, Trassin 2009, Mukherjee 2011], we are not aware of any theoretical study of GFO with variable iron composition. For instance, the dependence of the lattice parameters and the Ga/Fe partial occupancies on the Fe composition were deduced by Rietveld analysis of synchrotron x-ray diffraction at room temperature as demonstrated in [Arima 2004] and shown in Table 4.2. In fact, studying GFO with variable iron composition interestingly addresses the evolution of the properties of GFO via tuning the Ga/Fe ratio which seems to be promising precisely in terms of the magnetic properties. This is the subject of our results that are discussed in what follows.

4.3 Impact of Fe concentration on the properties of GFO

4.3.1 Calculation details

Our density functional-based calculations were carried out using the VASP package [vas], [Kresse 1999] by employing the projector augmented wave method [Blochl 1994] to solve the Kohn-Sham equations. The noncollinear spin-orbit coupling is included in the calculations as implemented in VASP [Hobbs 2000]. The GFO system was modeled by 8 formula-unit supercell. For all the considered configurations; i.e. ideal and Fe-excess; we have performed both atomic and volume relaxation. This was done by employing the Quasi-Newton method (as implemented in VASP) and for a large plane wave cutoff of 550 eV until the pressure on each atom reaches zero and Hellmann-Feynman forces are less than 0.1 meV/Å . As for the k-space integrations, we have found that 441 k points in the irreducible Brillouin zone are needed to converge the ground state energy and the magnetocrystalline anisotropy energy to within 10 μeV. We have performed our calculations within both the local density approximation (LDA) as parametrized by Perdew and Zunger [Perdew 1981b] and the generalized gradient approximation GGA as parametrized by Perdew, Becke and Ernzerhof [Perdew 1996] to investigate the influence of different types of exchange-correlation energies on the electronic and magnetic properties of GFO and examine how robust the results are. The LDA calculations failed to describe the properties of GFO as compared to experimental results: a narrow band gap (0.53 eV), reduced magnetic moment (3.5 μ_B), and wrong magnetization easy axis (b-axis) are obtained. Such a failure of the LDA is expected in correlated systems as transition metal oxides [Anisimov 1997]. Thereby, to account for the strong on-site Coulomb repulsion among the localized Fe 3d electrons, we have used the rotationally invariant LDA+U formalism as described in [Liechtenstein 1995] represented by the Hubbard-like term U and the exchange term J which led to an improvement of the ground state properties such as the band gap and the magnetic moments. The value of J was set to 1 eV. Meanwhile, the Coulomb repulsion parameter U was varied over a wide range starting from $U = 2eV$ and reaching $U = 8eV$ in order to observe at what stage do the ground state properties compare well to experimental ones at the level of the band gap and the magnetic moment.

Figure 4.3 shows the variation of the band gap E_g and the magnetic moment of the iron site in a GaFeO$_3$ unit cell as a function of the U. It can be noticed that both the LDA+U and GGA+U yield a band gap (3.2 eV) and a magnetic moment (4.4 $\mu_B/Fe2$) at $U = 8eV$; which is not far away from the experimental values.

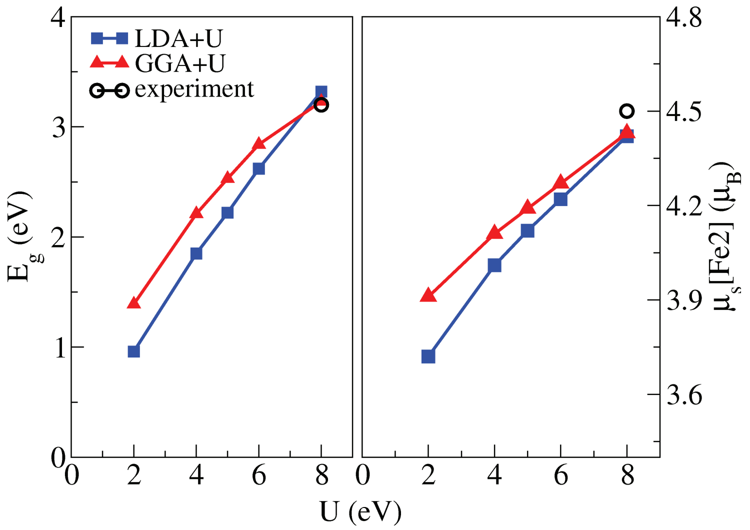

Figure 4.3: Variation of the band gap and the magnetic moment on the Fe2 site as a function of increasing the Coulomb repulsion parameter U obtained within both LDA+U and GGA+U.

The on-site Coulomb interaction of transition metals is usually very large in insulating oxides due to the poor screening. In fact, the constrained LDA of the Coulomb interaction of Fe in LaFeO$_3$ to be used in the standard LDA +U showed that U is about 7.8 and 9.2 eV for Fe^2+ and Fe^{3+}, respectively[Solovyev 1995]. However, the J_0 values for the trivalent M^{3+} are found to be about 1 eV for all 3d transition metals M in LaMO$_3$. Similar results are found for the magnetite [Madsen 2005]. On the other hand, Bulut, Scalapino, and White [Bulut 1993] showed that the renormalization of the Coulomb interaction depends on the type of model employed. Since the local density approximation is not a diagrammatic method, we do not know what type of renormalization is the most appropriate for the LDA +U model. In the so-called LDA +U_2 based on the assumption that only 3d states of t_{2g} symmetry are localized and the e_g are itinerant, and participate therefore to the screening of the localized t_{2g} electrons, significant lower values of $U_{t_{2g}}$ are found. This second approach confirms the view of Bulut et al. [Bulut 1993].

This approach will not work for GFO where a strong distortion of the Fe octahedra and tetrahedra strongly mix the e_g and t_{2g} states. It is therefore clear that using the effective Coulomb interaction U as an adjustable parameter is a valuable approach. We believe that the U used in the model calculation is just an effective Coulomb interaction and cannot be directly compared to the one obtained from experimental photoemission data. Finally, to assess the effect of relaxation on GFO's properties, calculations have been performed, within both approximations LDA+U and GGA+U with both values of U, using the experimental parameters and positions reported in [Arima 2004].

4.3.2 Properties of ideal GaFeO$_3$

In this section, we present the electronic and magnetic properties of an ideal-composition GaFeO$_3$ unit cell. The structural optimization of the system based on energy minimization revealed a stable antiferromagnetic coupling between the Fe ions occupying Fe1 and Fe2 sites. It can be noticed from Figure 4.3 that for $U = 8eV$ the LDA+U and GGA+U yield an energy band gap of 3.32 eV and 3.23 eV respectively which is not far away from the experimental value (3.2 eV) estimated from optical measurements [Kalashnikova 2005]. Meanwhile, using the experimental parameters without relaxation resulted in band gap values that are coincident to those of a relaxed unit cell and the same applies for the magnetic moments hereafter. The spin magnetic moments obtained for the ideal GaFeO$_3$ result in a net vanishing magnetization of the unit cell which describes a perfect antiferromagnetism where a local spin moment on the Fe ions of about 4.01 $\mu_B/Fe2$ is calculated within LDA+U and 4.1

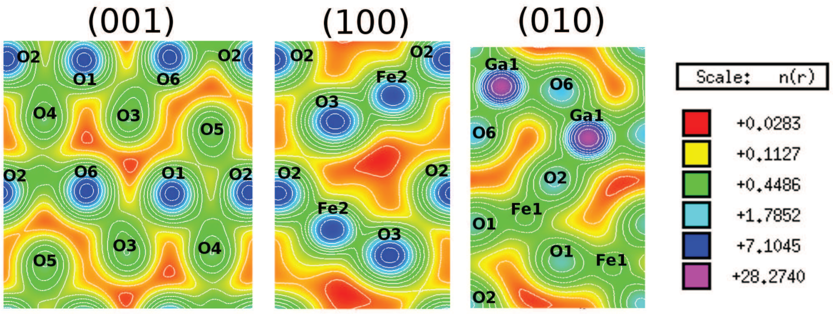

Figure 4.4: LDA+U (U=4 eV) charge distribution plotted across the three crystallographic directions in GaFeO$_3$ unit cell using a logarithmic scale.

$\mu_B/Fe2$ within GGA+U for $U = 4eV$. Interestingly, both the LDA+U and GGA+U gave a corresponding value of 4.4 $\mu_B/Fe2$ using $U = 8eV$ which is close to the experimental value of 4.5 $\mu_B/Fe2$. The value of the local orbital moment calculated is 0.026 $\mu_B/Fe2$ within LDA+U and 0.022 $\mu_B/Fe2$ within GGA+U for $U = 4eV$, whereas using $U = 8eV$ values of 0.018 $\mu_B/Fe2$ and 0.016 $\mu_B/Fe2$ are obtained respectively. These values are comparable to the one obtained experimentally at 190 K from XMCD sum rules (0.017 μ_B/Fe) [Kim 2006]. The net orbital moment of the unit cell vanishes as the spin moment. Those results are consistent with the previous work in [Roy 2011]. However, experiments have reported the dependence of GFO's magnetic properties on the Ga to Fe ratio [Arima 2004]; more precisely an enhancement of the magnetic properties as the iron concentration increases. In this sense, we have investigated the electronic and magnetic properties of $Ga_{2-x}Fe_xO_3$ with different Fe-compositions.

4.3.3 Structural properties

We have concentrated our study on three different compositions with: one, two, and three excess Fe ions corresponding respectively to: $x = 1.1$, 1.2, and 1.4 compositions. Following the procedure described earlier, we relaxed each composition with all its possible configurations in terms of the site occupation that the excess Fe ions might adopt and the kind of magnetic coupling to the surrounding ions. The relaxed lattice parameters relative to the different values of x obtained within LDA+U and GGA+U using $U = 4eV$ and $U = 8eV$ are plotted and compared to the experimental values in Figure 4.5. As compared to the experimental values reported previously in [Arima 2004] and more recently in [Mukherjee 2011], LDA+U underestimates the lattice parameters whereas GGA+U overestimates it. It seems that the relaxation is highly affected by the value of U. For instance, within LDA+U the higher value of U yields more underestimated a and b parameters despite a better value of c. This, as shown in 4.5, results in a more underestimated volume of the unit cell. On the other hand, GGA+U behaves just the opposite resulting in a less overestimated volume obtained using $U = 8eV$.

Indeed, an isotropic change of the a and b lattice parameters with the increase in the Fe content is observed, within both approximations, which is similar to the experimental behavior. This is attributed to the different ionic radius of

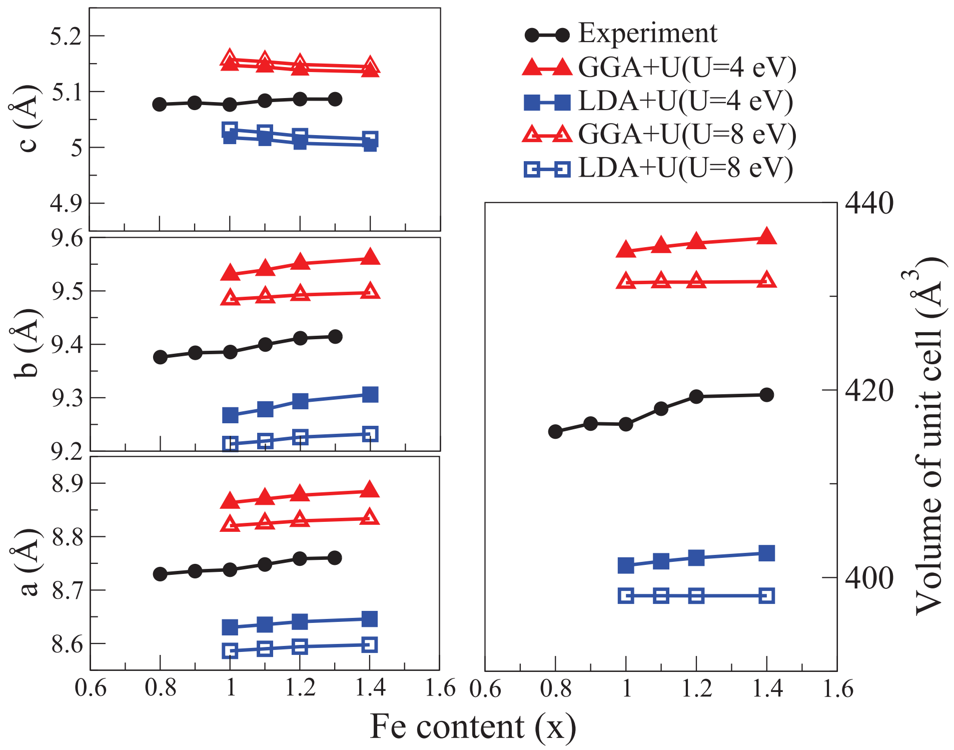

Figure 4.5: Variation of the lattice parameters, calculated within LDA+U and GGA+U for $U = 4eV$ and $U = 8eV$, in the GFO unit cell as a function of the variable Fe content as compared to the experimental values reported in [Mukherjee 2011].

Fe^{3+} and Ga^{3+} which drives the elongation of the bonds in the case where an Fe ion occupies the Ga site. As for the lattice parameter in the c-direction, the relatively smaller increase reported by experiment couldn't be reproduced by either approximations in our calculations. Figure 4.6 display the different octahedral sites in a unit cell of GFO with the bond lengths as obtained from the LDA+U and GGA+U calculations for both values of U. The off-center shift of the Fe ion from the center of the oxygen octahedron along the b-axis is highlighted in red color. Compared to the experimental values where a displacement of +0.2 Å is observed for Fe1 site and −0.1 Å for Fe2 site [Arima 2004], it can be seen that using a value of $U = 4eV$ underestimates the Fe1 displacement but overestimates that of Fe2. Nevertheless, calculations with $U = 8eV$ results in less distorted sites compared to $U = 4eV$. On the other hand, the Ga2 octahedral site appears to be more regular than the Fe-sites. We come back later to those aspects in the context of discussing the

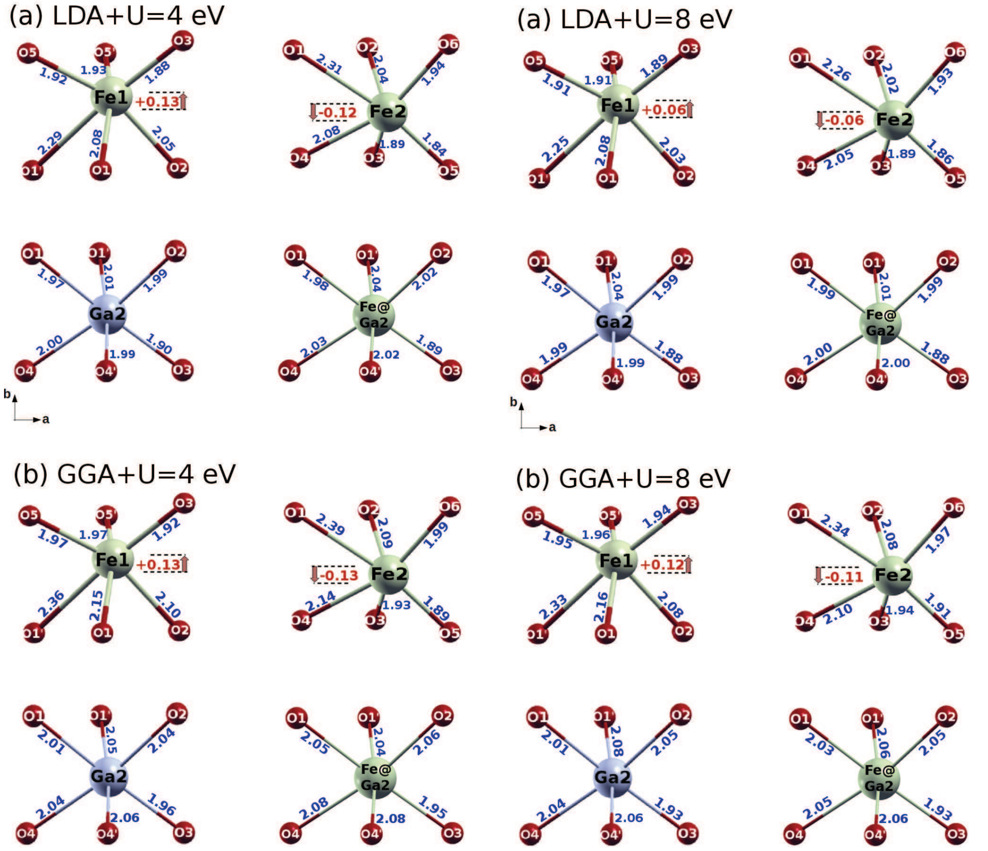

Figure 4.6: The different octahedral sites (Fe1, Fe2, Ga2) in GFO unit cell with the bond lengths displayed in units of Å as obtained from (a) LDA+U and (b) GGA+U calculations for $U = 4eV$ (Left panel) and $U = 8eV$ (Right panel). The red arrows represent the off-center movement of the Fe1 and Fe2 ions from the center of the oxygen octahedra; whereas the Ga2 octahedron is less distorted.

magnetic anisotropy of GFO.

Afterward, a self-consistent static calculation was performed to obtain the ground state properties. By comparing the different ground state energies we come out with two conclusions that are consistent with the experimental observations [Arima 2004] and previous theoretical results [Roy 2011]. First, the excess Fe ions are more likely to occupy the Ga2 sites than the Ga1 ones. Meanwhile, the energy minimization favors an antiferromagnetic coupling between the excess Fe ions occupying Ga2 sites and the Fe ions at Fe1.

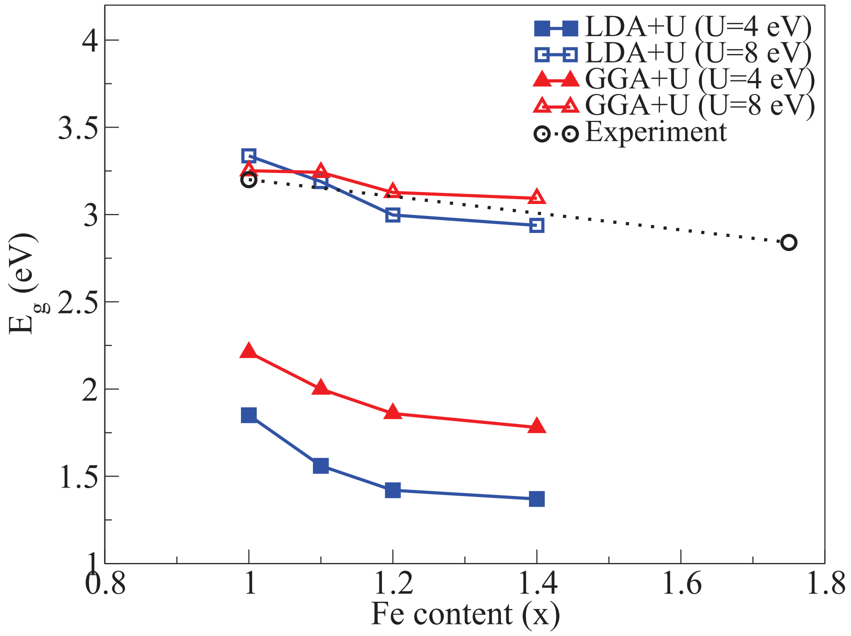

Figure 4.7: The variation of the energy band gap E_g as a function of increasing the Fe content in GFO unit cell as obtained from both LDA+U and GGA+U for $U = 4eV$ and $U = 8eV$. Experimental values, as reported in [Kalashnikova 2005, Kalashnikova 2009], are also shown for comparison.

4.3.4 Electronic properties

Now we discuss the impact of the excess Fe on the electronic properties in terms of the band gap and density of states. As the Fe content is increased, the band gap decreases, as it can be seen from Figure 4.7. Such behavior seems to be independent of the approximation and the U value. This decrease of the energy band gap as x increases is consistent with the experimental results revealing a decrease reaching a value of 2.84 eV for $x = 1.75$ [Kalashnikova 2009]. This behavior is emphasized by comparing the density of states; at this stage we choose to proceed the interpretation within the LDA+U and remark that GGA+U calculations yielded the same behavior. The total density of states corresponding to different iron content x are plotted as well as the d-states contribution of the Fe projected density of states (Figure 4.8 (b)) for both values of U. Before going into details we shall point out that, as expected from the LDA+U formalism [Anisimov 1997], the increased U value pushes the occupied d-states of Fe lower in energy unlike the unoccupied ones which are shifted upward. Rather than this fact, the following discussion applies for

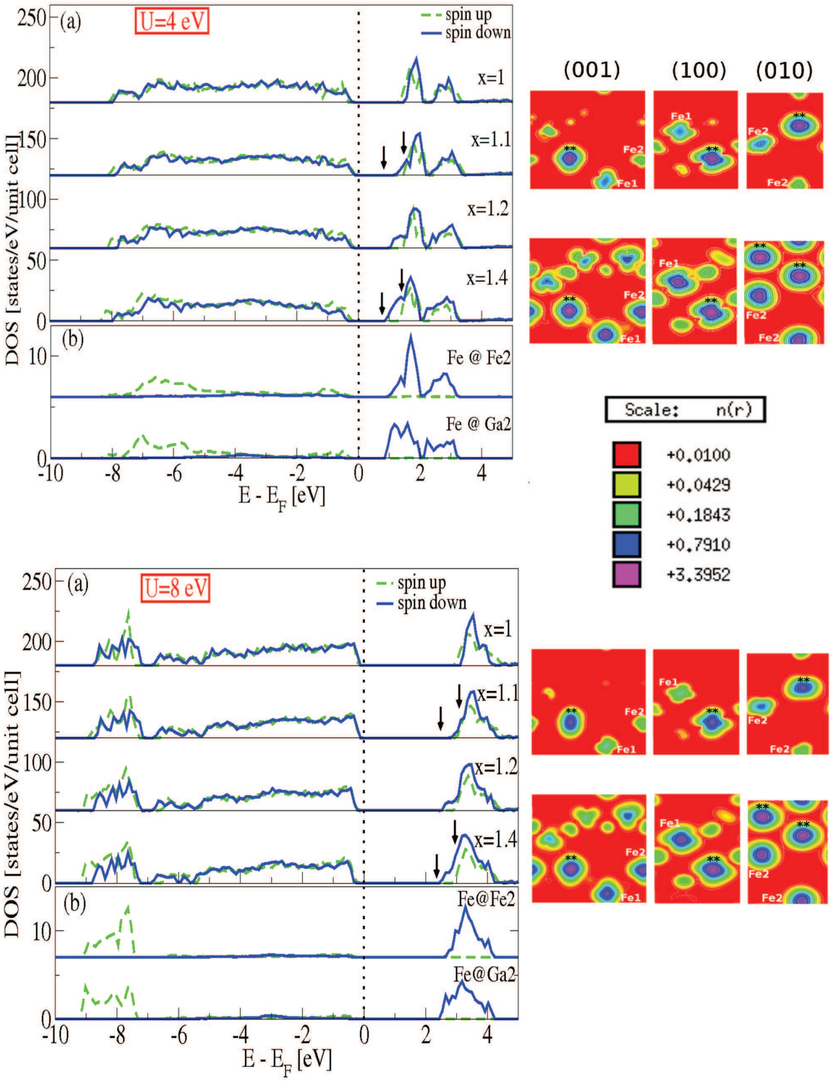

Figure 4.8: Left panel: (a) LDA+U total density of states for variable Fe content in $Ga_{2-x}Fe_xO_3$, (b) PDOS of the Fe excess Fe ion at Ga2 site and Fe ion at Fe2 site. Right panel: LDA+U partial charge distribution over the energy range marked in (a) by arrows, drawn with a logarithmic scale along the three crystallographic directions of the GFO unit cell and for varied Fe content. The Fe ion placing the Ga2 site is marked by stars. (The results are shown for both values of U).

both values of U.

By comparing the Fe PDOS of the excess Fe ion occupying Ga2 to that occupying Fe2 site, it can be observed that the unoccupied states of the former are closer to the Fermi level. Consequently, the effect of the excess Fe is to enhance the d-symmetry character of the bottom of the unoccupied states and hence reducing the energy band gap. A better understanding of this change in the density distribution upon increasing the Fe-composition is provided by plotting the partial charge distribution shown in right panel of Figure 4.8 over the energy interval corresponding to the change in the band gap (marked by arrows in Figure 4.8 (a)). It can be observed that all the Fe ionic sites contribute to the states appearing at the bottom of the unoccupied band, while the largest contribution seems to be that of the excess Fe ion. Meanwhile, all the Fe ionic sites show an increase in the states as the Fe-composition increases. The charge distribution plots along the different crystallographic directions in the GFO unit cell (Figure 4.4 and Figure 4.8) show a non-trivial degree of charge sharing between the ions; regardless of the value of U used. This precise observation is obtained using the logarithmic scale, unlike the previously reported results that showed insignificant degree of covalency by using a linear scale for the charge distribution plots [Roy 2011]. The validity of these preliminary observations has been tested by performing Bader charge analysis [Tang 2009] on the different Fe-composition GFO unit cells. We have converged our results with respect to a fine fft-grid $400 \times 432 \times 240$ within a relative error of $\pm 0.005 e^-$. The LDA+U ($U = 4eV$) obtained Bader charges on each ion are compiled in Table 4.1. It can be observed that these values are smaller than the former charges on each ion indicating a partial ionic bond-

	$x = 1$	$x = 1.1$	$x = 1.2$	$x = 1.4$
Ga1	+1.788	+1.8	+1.796	+1.798
Ga2	+1.832	+1.85	+1.847	+1.851
Fe1	+1.633	+1.646	+1.641	+1.638
Fe2	+1.631	+1.645	+1.644	+1.646
Fe at Ga2	- -	+1.659	+1.653	+1.657
O1	−1.21	−1.2	−1.179	−1.161
O2	−1.183	−1.183	−1.175	−1.168
O3	−1.091	−1.085	−1.069	−1.057
O4	−1.198	−1.206	−1.192	−1.186
O5	−1.028	−1.04	−1.038	−1.037
O6	−1.172	−1.179	−1.178	−1.179

Table 4.1: LDA+U ($U = 4eV$) calculated Bader charges per ion in GFO unit cell with variable Fe composition.

ing. Indeed, analyzing the Bader charges variation as a function of the Fe composition, one can point out that the Fe ion occupying the Ga2 site has a smaller Bader charge than the Ga ion occupying this site, i.e., the degree of covalency increases in the case of Fe-excess GFO unit cell which is consistent with the result of the band gap decrease. This decrease in the Bader charge is an implication of the increase in the Fe(@Ga2)-O bond lengths as compared to the Ga2-O by an average of 0.02 Å .

At this stage, we should mention that the calculations using $U = 8eV$ within either approximations yielded an increase of the Bader charge on the Fe ions by 0.1. This is interpreted by the smaller bond lengths obtained with the larger value of U (c.f. Figure 4.6). Such increase in the degree of ionicity is correlated to the wider band gap calculated for $U = 8eV$. Besides, the previous discussion on the evolution of the Bader charges as a function of the Fe-content for $U = 4eV$ also applies for larger value of U.

4.3.5 Magnetic properties

The issue of interest is the magnetic properties of such Fe-excess GFO systems. The spin and orbital moments of each Fe ion were obtained from the relativistic self-consistent calculations. Comparing the results for different Fe-content (Table 4.2), we observe almost the same behavior. The excess Fe ions occupying the Ga2 sites hold each a spin moment of about 4.08 μ_B (4.15 μ_B), obtained within LDA+U (GGA+U) for $U = 4eV$.

	$\mu_S[\mu_B]$	$x = 1$	$x = 1.1$	$x = 1.2$	$x = 1.4$
	Fe at Ga2	- -	4.08	4.08	4.08
LDA+U	Fe at Fe1	-4.02	-3.98	-3.97	-3.94
	Fe at Fe2	4.01	4.01	4.02	4.02
	Fe at Ga2	- - (4.7)	4.15	4.15	4.15
GGA+U	Fe at Fe1	-4.11 (-3.9)	-4.10	-4.08	-4.07
	Fe at Fe2	4.10 (4.5)	4.11	4.11	4.11

Table 4.2: Evolution of the spin moments on the different Fe ionic sites with the Fe content obtained within LDA+U and GGA+U for $U = 4eV$. The values in parentheses correspond to the spin moments estimated experimentally from Rietveld analysis [Arima 2004].

Comparing these calculated values to the ones estimated by Rietveld analysis performed on the experimental data of [Arima 2004], the consistency appears in the way that the Fe ion occupying the Ga2 site holds a spin moment larger than Fe2 by 1.8 % and 4.4 %, obtained from our calculation and experiment, respectively. On the other hand, a decrease of the spin moment with the increase of the number of excess iron ions is observed for the ones occupying the Fe1 sites being antiferromagnetically coupled to the irons occupying Fe2 and Ga2 sites. In an overall picture, Fe ions occupying Fe2 and Ga2 sites, on the one hand, are greater in number and hold spin moments higher than those occupying Fe1 sites. This difference among the atomic sites gives rise to a net non vanishing magnetization which is larger than that of the ideal unit cell. As for $U = 8eV$, the calculations show the same behavior as a function of increasing x despite that the spin moments are found to be larger (e.g. for $x = 1$: μ_S(Fe1)= $-4.44\mu_B$, μ_S(Fe2)= $4.44\mu_B$ while μ_S(Fe at Ga2)= $4.46\mu_B$). It is worthy to mention that using $U = 8eV$, both LDA+U and GGA+U gave almost identical values of spin moment per Fe site.

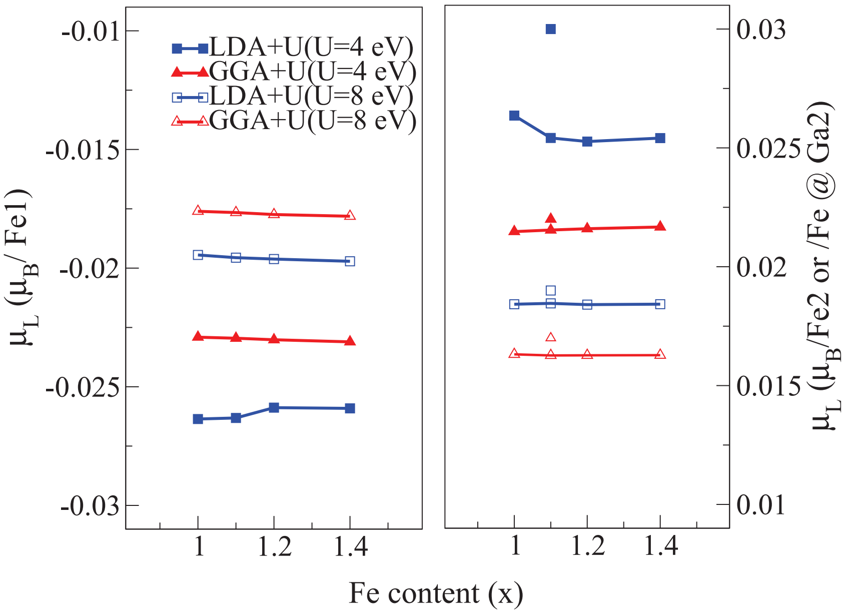

Figure 4.9: Evolution of the orbital moment per Fe site as a function of iron content x; calculated within both LDA+U and GGA+U shown for $U = 4eV$ and $U = 8eV$. The scattered symbols refer to the orbital moment per excess Fe ion occupying the Ga2 site.

A similar interpretation is ascribed to the orbital moment as our calculations show that the excess Fe ions occupying Ga2 site hold a larger orbital moment compared to the parent Fe sites and its preferentially antiferromagnetically coupled to Fe1 sites (Figure 4.9). Indeed, it turns out that increasing the on site Coulomb U energy, which further localizes the Fe-*3d* orbital, results in smaller values of the orbital moment. For instance, the orbital moment per Fe site decreases by about 23% within GGA+U ($U = 8eV$) as compared to ($U = 4eV$) and by 25% − 35% (depending on the Fe site) within LDA+U.

4.3.6 Magnetic anisotropy energy

We discuss now the magnetic anisotropy of GFO. To investigate the strong magnetic anisotropy observed experimentally, we carried out total energy calculations including the spin-orbit coupling in a self-consistent manner for a unit cell initialized with different orientations of the magnetic moments. Knowing that the magnetic anisotropy is the dependence of the system's total energy on the orientation of the magnetic moment, the magnetocrystalline anisotropy energy (MAE) is the difference in the total energies obtained for two different orientations of the magnetic moment. As the MAE is a quantity highly-sensitive to the k-point mesh, a fine sampling mesh is required to account for the numerical fluctuations. In this sense, we have performed several calculations for different numbers of k-points until a convenient convergence of the MAE value was reached (within a relative error of ±0.02). Figure 4.10 shows the convergence of the magnetocrystalline anisotropy energy for ideal GFO unit cell, calculated between the b and c-axis within LDA+U ($U = 4eV$), to a value around 2 meV.

In comparison, the GGA+U calculations yielded smaller magnetic anisotropy energy values. This difference found between the two approximations can be understood in the context of the orbital moment values; as the GGA+U favors smaller orbital moments compared to LDA+U. The left panel of Figure 4.11 shows the evolution of the MAE of a GFO unit cell with the Fe content obtained for $U = 4eV$ and $U = 8eV$. A decrease in the magnetic anisotropy energy, as x increases, is obvious in the results of both approximations and U values while all the different Fe-content systems conserve the positive sign of the MAE. Indeed, the relatively large value, in the order of meV, of the magnetic anisotropy energy indicates a strong anisotropy which favors the c-axis as the magnetization easy axis in a reasonable agreement with the experimental finding as reported for bulk [Arima 2004] and thin GFO films

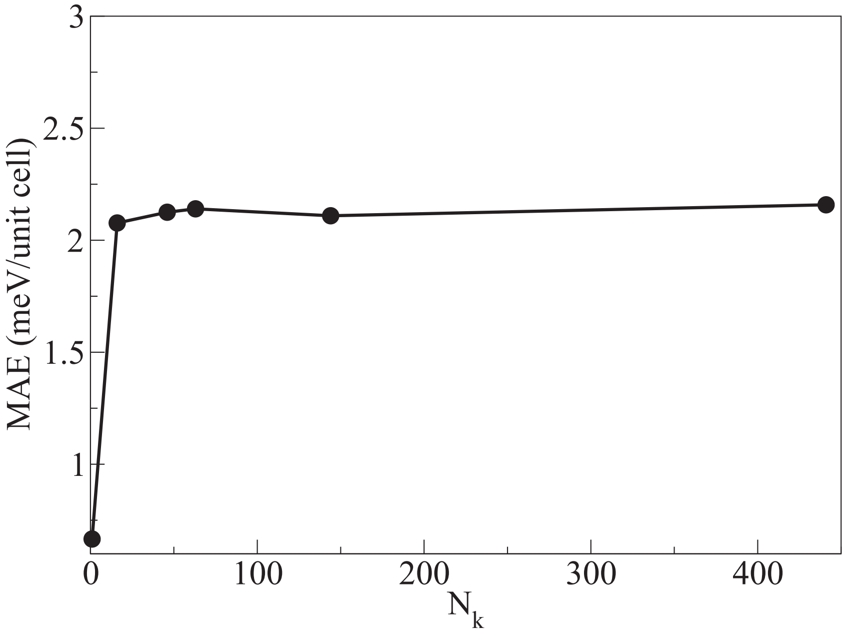

Figure 4.10: Magnetocrystalline anisotropy energy of GFO ($x = 1$) unit cell plotted as a function of the number of k-points in the Brillouin zone.

[Trassin 2009].

The direction of the magnetization easy axis is well explained by considering the direction of the octahedral distortions. From the bond lengths, one can distinguish that Fe1, Fe2, and Ga2 sites are distorted in the *ab* plane (Figure 4.6); though the degree of distortion is minimal for Ga2. This finding coincides with the argument provided by Kim *et al.* to explain the anisotropy in GFO [Kim 2006]. As the distortions are the largest along the b direction, this strengthens the hybridization and charge transfer along this axis. Thus, the resulting orbital moment and consequently magnetization easy axis is oriented along the c axis.

In the following we consider the reason driving the decrease of anisotropy with the increase of the iron content x. Based on the ground state optimization described earlier, the excess iron ion occupies the Ga2 site preferentially. As mentioned previously, the bond lengths obtained from the ground state show that the Fe1 and Fe2 octahedra are significantly more distorted (by one order of magnitude) than the Ga2 octahedron. Consequently, once the iron ion occupies the Ga2 site, it becomes less anisotropic than the parent Fe sites (Fe1 and Fe2); thereby the overall anisotropy of the unit cell decreases. This

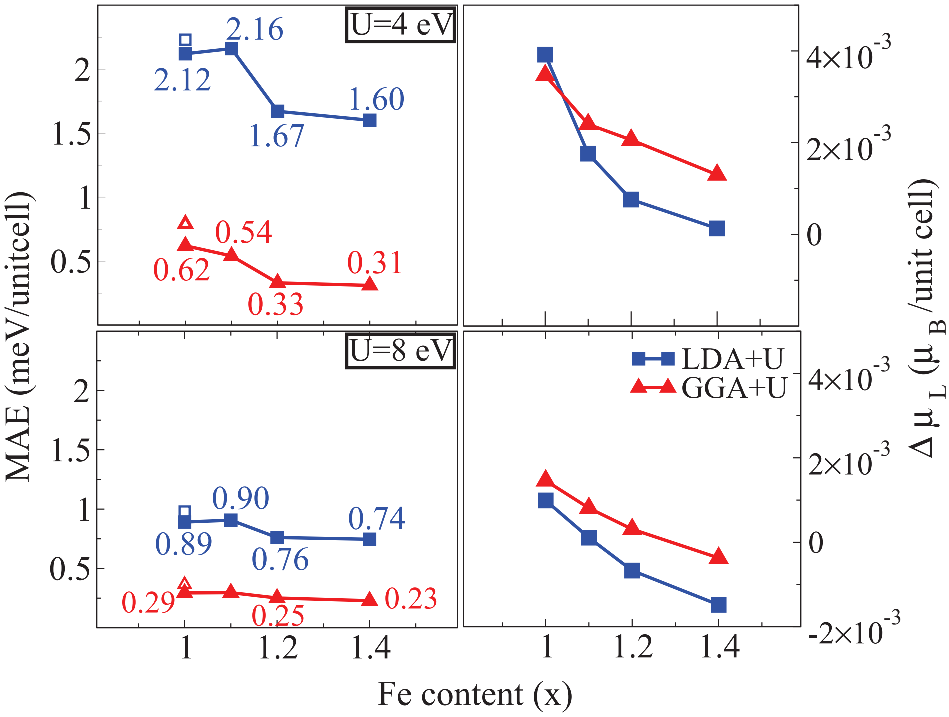

Figure 4.11: LDA+U and GGA+U variation of (left panel) magnetocrystalline anisotropy energy and (right panel) orbital moment anisotropy as a function of increasing the iron content in a GFO unit cell. The results are shown for both: $U = 4eV$ (upper panel) and $U = 8eV$ (lower panel). The scattered open symbols denote the MAE calculated using the experimental parameters of GFO ($x = 1$) unit cell.

idea is supported by the MAE value (1.7 meV) calculated for a GFO ($x = 1$) unit cell with site disorder; interchange between Fe2 site Ga2 site; which is smaller than the value in the ideal case (2 meV).

As a matter of fact, the MAE values calculated with either approximations are affected by the choice of the U value. It can be seen that increasing the U to 8 eV gives values of MAE which are lower than the ones obtained for $U = 4eV$ by about 58% and 53% within LDA+U and GGA+U respectively. This is interpreted by the fact, mentioned earlier, that $U = 8eV$ calculated orbital moments are lower than those obtained using $U = 4eV$.

In the context of analyzing these results on the magnetic anisotropy of GFO, we discuss its possible link to the changes in the spin and the orbital moments induced by the reorientation of the spin quantization axis. The spin moments obtained from both LDA+U and GGA+U are almost isotropic (the change is within 0.05% from LDA+U and 0.002 % from GGA+U). Meanwhile, the two approximations result in a similar decreasing behavior of the orbital-moment anisotropy, e.g., in case $x = 1$ the orbital moment reduces by about 4% upon passing from the easy to the hard magnetization axis. From a qualitative point of view, Figure 4.11 reveals that the MAE and orbital anisotropy follow the same trend as the Fe-content increases. Thus, one can conclude that the decreasing orbital anisotropy as a function of the Fe-content is at the origin of the obtained decreasing MAE values within both approximations. Indeed, the anisotropic behavior of the system is dominated by the Fe1 site which appears to be the more distorted one.

In sight of this discussion, it may be thought that the calculated MAE is very sensitive to the structural properties that are basically determined by the relaxation conditions. To know where our results lie with respect to the actual anisotropic state of GFO, we choose to do sort of reference calculation using the experimental parameters (available for $x = 1$) without performing any relaxation. As mentioned earlier, such calculations led to the same electronic (band gap) and magnetic properties (spin and orbital moments). Regarding the magnetic anisotropy energy, the values designated by open symbols in Figure 4.11 reveal that the relaxation affects the MAE values by about −7% and −20% within LDA+U and GGA+U respectively without affecting the favorable magnetization direction. Thus, we can conclude that the smaller MAE values obtained either with GGA+U or a higher value of the Coulomb repulsion are due to the improved level of approximation describing the interaction among the d-states rather than the difference in the structural distortions induced by relaxation.

4.4 Optical properties

Before going into the details of the optical properties of GFO, it is important to give an overview of the theory used to calculate the optical spectra within the framework of the density functional theory.

4.4.1 Theory behind optical spectra calculations

So far, we have discussed the ground state of a physical system that is at rest. Nevertheless, our knowledge of its electronic structure is represented in reproducing some theoretical observables that are measured in experiments. In particular, the response of a material to an external electromagnetic field is represented by evaluating the static and frequency-dependent dielectric response functions, such as absorption, reflectance, and electronic loss spectra. The evaluation of these quantities is important from theoretical point of view to interpret the measured optical properties of materials.

Indeed, it is now generally accepted that an accurate quantitative description requires a treatment beyond the independent-particle picture though a qualitative agreement between theory and experiment can often be achieved on the level of DFT, i.e. by using the Kohn-Sham eigenvalues and their eigenfunctions. In this chapter, we give an overview of the methodology of the linear response used within DFT formalism and in particular the optical response represented by the dielectric function.

4.4.1.1 Linear Response

Static response functions

Static response functions correspond to the response of electrons to static perturbations (e.g. strain or electric field) or to response at low frequencies that can be considered adiabatic. Thus, it is convenient to start from the perturbation theory where the Hamiltonian is expressed as:

$$H = H^{(0)} + \lambda \Delta H \tag{4.1}$$

where $H^{(0)}$ is the unperturbed Hamiltonian and ΔH represents the perturbation and it is expanded by organizing terms in powers of the parameter λ. For small perturbations, it is enough to employ an expansion to first order in ΔH whereas for higher order expansions the variation in the wave function must be determined such that for a many-body system it is expressed in terms of a sum over the excited states of the unperturbed Hamiltonian:

$$\Delta\Psi_i(\mathbf{r}_i) = \sum_{j\neq i} \Psi_j(r_i)\frac{\langle\Psi_j|\Delta H|\Psi_i\rangle}{E_i - E_j} \tag{4.2}$$

As for a ground state operator $\hat{O}$, the change in its expectation value upon perturbation is written as:

$$\Delta\langle\hat{O}\rangle = \sum_{j\neq i}\langle\Delta\Psi_j|\hat{O}|\Psi_i\rangle + c.c. = \sum_{j\neq i}\frac{\langle\Psi_i|\hat{O}|\Psi_j\rangle}{E_i - E_j} + c.c. \tag{4.3}$$

In the independent-particle approximation, the variation of the independent-particle orbitals $\Delta\psi_i(\mathbf{r})$ to the first order in the perturbation theory is written in terms of sum, over all the occupied and empty states, of the unperturbed effective Hamiltonian $H^{(0)}_{eff}$ as:

$$\Delta\psi_i(\mathbf{r}) = \sum_{j\neq i}\psi_j(\mathbf{r})\frac{\langle\psi_j|\Delta H_{eff}|\psi_i\rangle}{\epsilon_i - \epsilon_j} \tag{4.4}$$

Besides, $\Delta\hat{O}$ shall be expressed in terms of the independent-particle orbitals ψ_i and the variation of the effective Hamiltonian ΔH_{eff} such that:

$$\begin{aligned}\Delta\langle\hat{O}\rangle &= \sum_{i=1}^{occ}\langle\psi_i + \delta\psi_i|\hat{O}|\psi_i + \delta\psi_i\rangle \\ &= \sum_{i=1}^{occ}\sum_{j}^{empty}\frac{\langle\psi_i|\hat{O}|\psi_j\rangle\langle\psi_j|\Delta H_{eff}|\psi_i\rangle}{\epsilon_i - \epsilon_j} + c.c.\end{aligned} \tag{4.5}$$

The expression of the change in the density operator in response to a static perturbation follows from Eq.4.5 and is written as:

$$\Delta n(\mathbf{r}) = \sum_{i=1}^{occ}\sum_{j}^{empty}\psi_i^*(\mathbf{r})\psi_j(\mathbf{r})\frac{\langle\psi_j|\Delta V_{eff}|\psi_i\rangle}{\epsilon_i - \epsilon_j} + c.c. \tag{4.6}$$

The density response function to a perturbation $V_{eff}(\mathbf{r}')n(\mathbf{r}')$ is defined as the response to a variation of the effective potential:

$$\chi^0(r, r') = \frac{\delta n(\mathbf{r})}{\delta V_{eff}(\mathbf{r}')} = 2\sum_{i=1}^{occ}\sum_{j}^{empty}\frac{\psi_i^*(\mathbf{r})\psi_j(\mathbf{r})\psi_j^*(\mathbf{r}')\psi_i(\mathbf{r}')}{\epsilon_i - \epsilon_j} \tag{4.7}$$

For further simplification, it is yet more useful to use the Fourier transform of the response function:

$$\chi^0(\mathbf{q},\mathbf{q}') = \frac{\delta n(\mathbf{q}')}{\delta V_{eff}(\mathbf{q})} = 2\sum_{i=1}^{occ}\sum_{j}^{empty}\frac{M^*_{ij}(\mathbf{q})M_{ij}(\mathbf{q}')}{\epsilon_i - \epsilon_j} \tag{4.8}$$

where $M_{ij}(\mathbf{q}) = \langle\psi_i|e^{i\mathbf{q}\cdot\mathbf{r}}|\psi_j\rangle$.
The simplest treatment of the response function χ^0 is within approximations where electrons are considered to be non-interacting such that $\Delta V_{eff} = \Delta V_{ext}$ and χ_0 represents the response to an external perturbation. However, in Kohn-Sham theory where the effective mean-field theory is employed, the Hamiltonian must be found based on the self-consistent field approach in which many-electron system is described by a time-dependent interaction of a single electron with a self-consistent electromagnetic field. In this case, the total field depends upon the internal potential such that: $V_{eff} = V_{ext} + V_{int}[n]$ and the response to the external field is given to linear oder by:

$$\chi(\mathbf{q},\mathbf{q}') = \frac{\delta n(\mathbf{q})}{\delta V_{ext}(\mathbf{q}')} \tag{4.9}$$

or it can be rewritten as:

$$\chi = \frac{\delta n}{\delta V_{eff}}\frac{\delta V_{eff}}{\delta V_{ext}} = \chi^0\left[1 + \frac{\delta V_{int}}{\delta n}\frac{\delta n}{\delta V_{ext}}\right] = \chi^0(1 + K\chi) \tag{4.10}$$

where the kernel K is given by:

$$K(\mathbf{q},\mathbf{q}') = \frac{4\pi}{q^2}\delta_{\mathbf{q},\mathbf{q}'} + \frac{\delta^2 E_{xc}[n]}{\delta n(\mathbf{q})\delta n(\mathbf{q}')} \equiv V_C(q)\delta_{\mathbf{q},\mathbf{q}'} + f_{xc}(\mathbf{q},\mathbf{q}') \tag{4.11}$$

Many approximations for f_{xc} have been introduced one of which is the random phase approximation (RPA) where $f_{xc} = 0$ [Pines 1964]. Yet, the extension of the static response to dynamical response approaches more the description and understanding of electronic excitations.

Dynamic response

The basic ideas of linear response are derived starting from the classical harmonic oscillator [Martin 1968]. The response to a force $F(t) = F(\omega)e^{-i\omega t}$ with frequency ω is given by:

$$\chi(\omega) = \frac{x(\omega)}{F(\omega)} = \frac{1}{M}\frac{1}{\omega_0^2 - \omega^2 - i\omega\Gamma/M} \tag{4.12}$$

where x is the displacement and Γ is a damping term. Indeed, the Kramers-Kronig relations allow to derive the real and imaginary parts of the response function from one another as follows:

$$Re\chi(\omega) = -\tfrac{1}{\pi}\int_{-\infty}^{\infty} d\omega' \tfrac{Im\chi(\omega')}{\omega-\omega'} \quad Im\chi(\omega) = \tfrac{1}{\pi}\int_{-\infty}^{\infty} d\omega' \tfrac{Re\chi(\omega')}{\omega-\omega'} \tag{4.13}$$

When considering the non-interacting particle approximation, the response function can be written as a complex function with a small imaginary damping factor η:

$$\chi^0_{a,b}(\omega) = 2\sum_{i=1}^{occ}\sum_{j}^{empty}\frac{[M^a_{ij}]^* M^b_{ij}}{\epsilon_i - \epsilon_j + \omega + i\eta} \tag{4.14}$$

where $M^a_{ij} = \langle\psi_i|\hat{O}^a|\psi_j\rangle$ are the matrix elements of a given operator. Following the Kramers-Kronig relations, the real and imaginary part can be written explicitly as:

$$\begin{gathered} Re\chi^0(\omega)_{a,b} = \textstyle\sum_{i=1}^{occ}\sum_{j}^{empty}\frac{[M^a_{ij}]^* M^b_{ij}}{(\epsilon_i-\epsilon_j)^2-\omega^2} \\ Im\chi^0(\omega)_{a,b} = \textstyle\sum_{i=1}^{occ}\sum_{j}^{empty}[M^a_{ij}]^* M^b_{ij}\delta(\epsilon_j - \epsilon_i - \omega) \end{gathered} \tag{4.15}$$

The generalization of the independent-particle expressions to self-consistent field methods is straightforward except that the effective field is itself frequency-dependent ($V_{eff}(\omega)$). Thus, the expression of the kernel K in Eq.4.11 is generalized as to include the frequency-dependence:

$$K(\mathbf{q},\mathbf{q}',\omega) = V_C(q)\delta_{\mathbf{q},\mathbf{q}'} + f_{xc}(\mathbf{q},\mathbf{q}',\omega) \tag{4.16}$$

In this case, the Coulomb interaction is considered to be instantaneous. It follows, the dynamical generalization of the response function in Eq.4.10:

$$\chi(\omega) = \chi^0(\omega)[1 - \chi^0(\omega)K(\omega)]^{-1} \tag{4.17}$$

4.4.1.2 Dielectric functions

Dielectric tensor

Dielectric functions are one of the most important response functions in condensed matter physics. They can be defined in terms of currents and fields or densities and scalar potentials. The expressions follow from the Maxwell's equations so that to describe the interaction of matter with an external time-dependent field. In this case, the charges and currents are divided into an internal and external contribution such that the general expression of the internal current density is given to linear order in terms of the total electric field **E** in the material as:

$$\mathbf{j}_{int}(\mathbf{r},t) = \int d\mathbf{r}' \int dt' \sigma(\mathbf{r},\mathbf{r}',t-t')\mathbf{E}(\mathbf{r}',t') \tag{4.18}$$

where σ is the microscopic conductivity tensor. Indeed, for a time-dependent perturbation which is proportional $e^{i\omega t}$ the expression becomes:

$$\mathbf{j}_{int}(\mathbf{r},\omega) = \int d\mathbf{r}' \sigma(\mathbf{r},\mathbf{r}',\omega)\mathbf{E}(\mathbf{r}',\omega). \tag{4.19}$$

Thus, by applying the Maxwell's equations the total field is written as:

$$\mathbf{E}(\mathbf{r},\omega) = \int d\mathbf{r}' \varepsilon^{-1}(\mathbf{r},\mathbf{r}',\omega)\mathbf{D}(\mathbf{r}',\omega), \tag{4.20}$$

or one obtains the expression of the field which is only due to external sources **D**,

$$\mathbf{D}(\mathbf{r},\omega) = \int d\mathbf{r}' \varepsilon(\mathbf{r},\mathbf{r}',\omega) \cdot \mathbf{E}(\mathbf{r}',\omega) \tag{4.21}$$

where,

$$\varepsilon(\mathbf{r},\mathbf{r}',\omega) = \delta(\mathbf{r}-\mathbf{r}') + \frac{4\pi i}{\omega}\sigma(\mathbf{r},\mathbf{r}',\omega). \tag{4.22}$$

In this case, ε and σ are the response to the total field **E** and they satisfy the Kramers-Kronig relations.

4.4.1.3 Dielectric response for non-interacting particles

The general case of time-dependent electric and magnetic fields can conveniently be treated by calculating the current response to the the vector potential **A**. The perturbation can be written in terms of **A** as:

$$\Delta H(t) = \frac{1}{2m_e}\sum_i \left\{ \left[\mathbf{p}_i - \frac{e}{c}\mathbf{A}(t)\right]^2 - \mathbf{p}_i^2 \right\} \tag{4.23}$$

where $\mathbf{E}(t) = -\frac{1}{c}\frac{d\mathbf{A}}{dt}$ and $\mathbf{E}(\omega) = -\frac{i\omega}{c}\mathbf{A}(\omega)$. The response is the macroscopic average of current density:

$$\mathbf{j} = -e\langle \mathbf{v} \rangle = -\frac{e}{m}\langle \mathbf{p} + \frac{e}{c}\mathbf{A} \rangle \tag{4.24}$$

By using Eq.4.14 and 4.22, the expression of the dielectric tensor follows:

$$\varepsilon_{\alpha\beta}(\omega) = \delta_{\alpha\beta} - \frac{e^2}{m_e\Omega}\frac{1}{\omega^2}\sum_i \left[f_i\delta_{\alpha\beta} + \sum_j \frac{f_i - f_j}{\hbar m_e}\frac{\langle\psi_i|p_\alpha|\psi_j\rangle\langle\psi_j|p_\beta|\psi_i\rangle}{\epsilon_i - \epsilon_j + \omega + i\eta} \right] \tag{4.25}$$

where f_i are occupation numbers and η is a small damping factor. The p matrix elements do not vary rapidly as a function of the energy for transitions between each pair of bands of electronic states so that the imaginary part of $\varepsilon(\omega)$ directly reveals singularities in the density of states for optical transitions. In particular, in the case of independent-particle approximation, this is a joint density of states for transitions between pairs of filled and empty bands weighted by the matrix elements.

Dielectric functions in the self-consistent field theory

The general form of response functions in self-consistent field theories is expressed in terms of the non-interacting response functions χ^0 and the interaction kernel K as given in Eq.4.17. Indeed, in a periodic medium at any given point $\mathbf{q}$ in the Brillouin zone, χ^0 can be written as a matrix over reciprocal lattice vectors as [Adler 1962, Wiser 1963, Ehrenreich 1959]:

$$\begin{aligned}\chi^0_{\mathbf{G},\mathbf{G}'}(\mathbf{q},\omega) &= \frac{1}{\Omega}\sum_{n,n',\mathbf{k}} 2w_{\mathbf{k}}(f_{n'\mathbf{k}+\mathbf{q}} - f_{n\mathbf{k}}) \\ &\times \frac{\langle\psi_{n'\mathbf{k}+\mathbf{q}}|e^{i(\mathbf{q}+\mathbf{G})\mathbf{r}}|\psi_{n\mathbf{k}}\rangle\langle\psi_{n\mathbf{k}}|e^{-i(\mathbf{q}+\mathbf{G}')\mathbf{r}'}|\psi_{n',\mathbf{k}+\mathbf{q}}\rangle}{\epsilon_{n',\mathbf{k}+\mathbf{q}} - \epsilon_{n\mathbf{k}} - \omega - i\eta}\end{aligned} \tag{4.26}$$

where Ω is the volume of the primitive cell and the w_k are k-point weights while f are the Fermi weights that are 1 for occupied and 0 for unoccupied states. $\mathbf{G}$ and $\mathbf{G}'$ are reciprocal lattice vectors and $\mathbf{q}$ stands for the Bloch vector of the incident wave. The Fourier transform of the frequency-dependent symmetric dielectric matrix is given by:

$$\varepsilon_{\mathbf{G},\mathbf{G}'}(\mathbf{q},\omega) = \delta_{\mathbf{G},\mathbf{G}'} - \frac{4\pi e^2}{|\mathbf{G}+\mathbf{q}||\mathbf{G}'+\mathbf{q}|}\chi^0_{\mathbf{G},\mathbf{G}'}(\mathbf{q},\omega) \tag{4.27}$$

The evaluation of the macroscopic dielectric matrix $\varepsilon_\infty(\mathbf{q},\omega)$ is as follows:

$$\frac{1}{\varepsilon_\infty(\hat{\mathbf{q}},\omega)} = \lim_{\mathbf{q}\to 0}\varepsilon^{-1}_{0,0}(\mathbf{q},\omega) \tag{4.28}$$

In this case, the local field effects, which are the changes of the cell periodic part of the potential, are included on the Hartree level only. Nevertheless, if the local field effects are neglected, in other words if the off-diagonal elements of the dielectric matrix are negligible, the macroscopic dielectric function can be approximated as:

$$\varepsilon_\infty(\hat{\mathbf{q}},\omega) \approx \lim_{\mathbf{q}\to 0}\varepsilon_{0,0}(\mathbf{q},\omega) \tag{4.29}$$

Following this simplification, the imaginary part of the macroscopic dielectric function is given by:

$$\varepsilon_{\infty}^{(2)}(\hat{\mathbf{q}},\omega)=\frac{4\pi^2e^2}{\Omega}\lim_{\mathbf{q}\to 0}\frac{1}{|\mathbf{q}|^2}\sum_{c,v,\mathbf{k}}2w_{\mathbf{k}}\delta(\epsilon_{c\mathbf{k}+\mathbf{q}}-\epsilon_{v\mathbf{k}}-\omega)\times|\langle u_{c\mathbf{k}+\mathbf{q}}|u_{v\mathbf{k}}\rangle|^2 \tag{4.30}$$

where the indices c and v correspond to the conduction and valence band respectively. The dielectric function depends on the direction $\hat{\mathbf{q}}=\mathbf{q}/|\mathbf{q}|$ such that:

$$\varepsilon_{\infty}(\hat{\mathbf{q}},\omega)=\lim_{\mathbf{q}\to 0}\varepsilon_{\infty}(\mathbf{q},\omega)=\sum_{\alpha,\beta}\hat{\mathbf{q}}_{\alpha}\varepsilon_{\alpha\beta}(\omega)\hat{\mathbf{q}}_{\beta} \tag{4.31}$$

Indeed, the 3×3 Cartesian tensor $\varepsilon_{\alpha\beta}$ is defined by its imaginary part as:

$$\varepsilon_{\alpha\beta}^{(2)}(\omega)=\frac{4\pi^2e^2}{\Omega}\lim_{\mathbf{q}\to 0}\frac{1}{q^2}\sum_{c,v,\mathbf{k}}2w_{\mathbf{k}}\delta(\epsilon_{c\mathbf{k}}-\epsilon_{v\mathbf{k}}-\omega)\times\langle u_{c\mathbf{k}+e_{\alpha}q}|u_{v\mathbf{k}}\rangle\langle u_{c\mathbf{k}+e_{\beta}q}|u_{v\mathbf{k}}\rangle^{*} \tag{4.32}$$

whereas the real part is obtained from the imaginary part using the Kramers-Kronig transformation:

$$\varepsilon_{\alpha\beta}^{(1)}(\omega)=1+\frac{2}{\pi}P\int_0^{\infty}\frac{\varepsilon_{\alpha\beta}^{(2)}(\omega')\omega'}{\omega'^2-\omega^2}d\omega' \tag{4.33}$$

where P denotes the principle value.

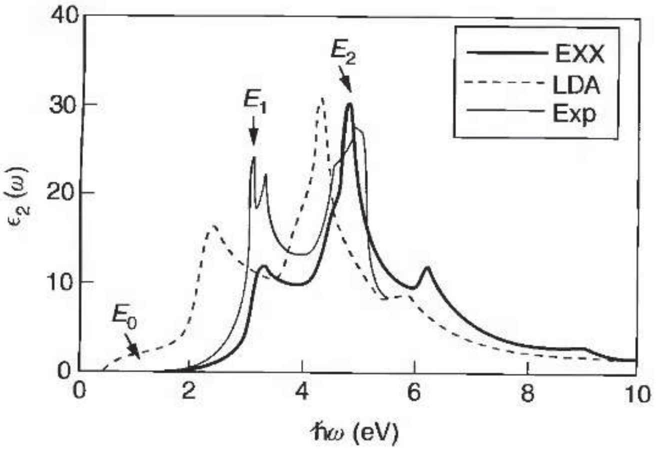

Figure 4.12: Calculated and experimental optical spectra of GaAs comparing the experimental and the two density functional calculations: the LDA and exact exchange [Staedele 1999].

The dielectric properties are affected by interactions among the electrons, in particular the electron-hole attraction leads to bound states in the gap. Thus, including these interactions induces changes in the spectrum. Indeed, many calculations done using adiabatic LDA and GGA have improved the agreement with experiments over the non-interacting approximation though better results could be obtained using many-body calculations (GW quasi-particles). Figure 4.12 shows the optical spectra of GaAs compared between experiment and different levels of theory, LDA and exact exchange, where the LDA underestimation of the band gap versus the improvement obtained by using the exact exchange is depicted [Staedele 1999]. Nevertheless, the inclusion of the electron-hole interaction remains a barrier toward achieving consistency between calculated and measured optical spectra; a problem that is overcome by solving the two-particle Bethe-Salpeter equation.

4.4.2 Optical properties of GFO: An insight of cationic site occupation

The aforementioned interesting aspects of GFO, in particular the exotic disorder-driven ferrimagnetism and the concentration dependent properties pushes forward the inquiry about a more detailed understanding of the properties of this material. In this sense, investigating the optical properties seems to be an important approach. As the optical spectra of such transition metal oxide resembles the intra-band as well as the charge transfer transitions, a direct comparison between experimental spectroscopic results and theoretical calculated spectra will be of great interest to understand the electronic properties and the disorder in GFO.

In the following, the dielectric function is calculated considering different cation site occupations to have access to the effect of disorder. Besides, the effect of the composition is addressed by considering different Fe concentrations ($1 \leq x \leq 1.4$). The exchange-correlation potentials used were within the GGA+U employing $U = 4eV$ and $J = 1eV$. The frequency dependent dielectric matrix was calculated after the ground state has been determined. In particular, the imaginary part is calculated by a summation over the empty states, as shown in the previous section, according to the following equation (as implemented in VASP [Gajdos 2006]),

$$\varepsilon^{(2)}_{\alpha\beta}(\omega) = \frac{4\pi^2 e^2}{\Omega} \lim_{q\to 0} \frac{1}{q^2} \sum_{c,v,\mathbf{k}} 2w_{\mathbf{k}} \delta(\epsilon_{c\mathbf{k}} - \epsilon_{v\mathbf{k}} - \omega) \times \langle u_{c\mathbf{k}+\mathbf{e}_\alpha \mathbf{q}} | u_{v\mathbf{k}} \rangle \langle u_{c\mathbf{k}+\mathbf{e}_\beta \mathbf{q}} | u_{v\mathbf{k}} \rangle^*, \tag{4.34}$$

where c and v refer to the conduction and the valence band states, and $u_{c\mathbf{k}}$ is the cell periodic part of the wave functions at the k-point $\mathbf{k}$ while the vectors $\mathbf{e}_\alpha$ are unit vectors for the three cartesian directions. The real part $\varepsilon^{(1)}$ of the dielectric tensor is straight forward obtained by the Kramers-Kronig transformation. Due to computational limits, the local field effects as well as excitonic effects were neglected in our calculations. Our calculations are used to support spectroscopic ellipsometry measurements performed by our experimental colleagues in the group of Nathalie Viart.

4.4.2.1 Effect of Fe concentration

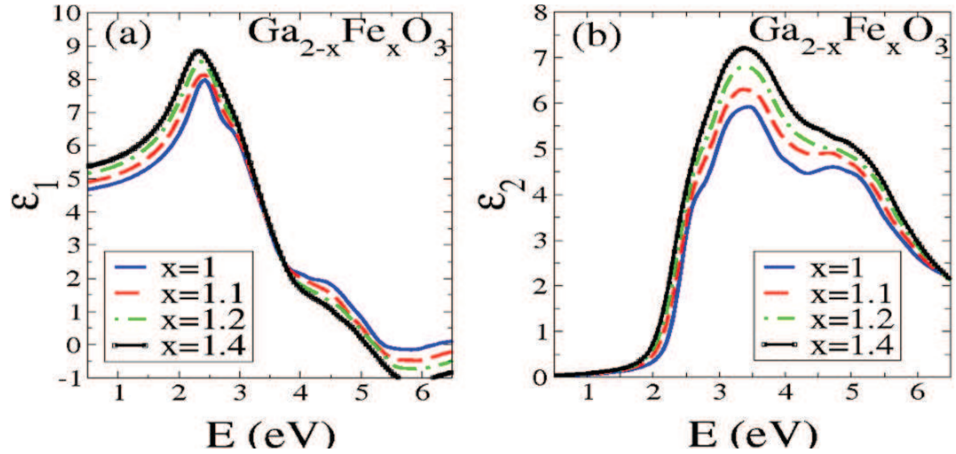

Figure 4.13: Calculated (a) $\varepsilon^{(1)}$ and (b) $\varepsilon^{(2)}$ spectra for various values of Fe content x in $Ga_{2-x}Fe_xO3$ unit cell.

As mentioned earlier, the properties of GFO are highly influenced by the Fe/Ga ratio. In this sense, we address in this section the evolution of the optical properties as a function of increasing the Fe concentration x [1]. Figure 4.13 displays $\varepsilon^{(1)}$ and $\varepsilon^{(2)}$ spectra calculated for different values of x. We notice

---

[1] The crystallographic orthorhombic structure of GFO implies that its optically biaxial. However, we proceed the discussion considering the average of the three components of the dielectric function.

that the static dielectric function increases almost linearly with x, from 4.6 for $x = 1$ to 5.3 for $x = 1.4$ which is in good agreement with the experimental results shown in Figure 4.14; 4.75 is reported for $x = 1$ and 5.5 for $x = 1.4$. Indeed, concerning the $\varepsilon^{(2)}$, we note a difference in the low-energy region

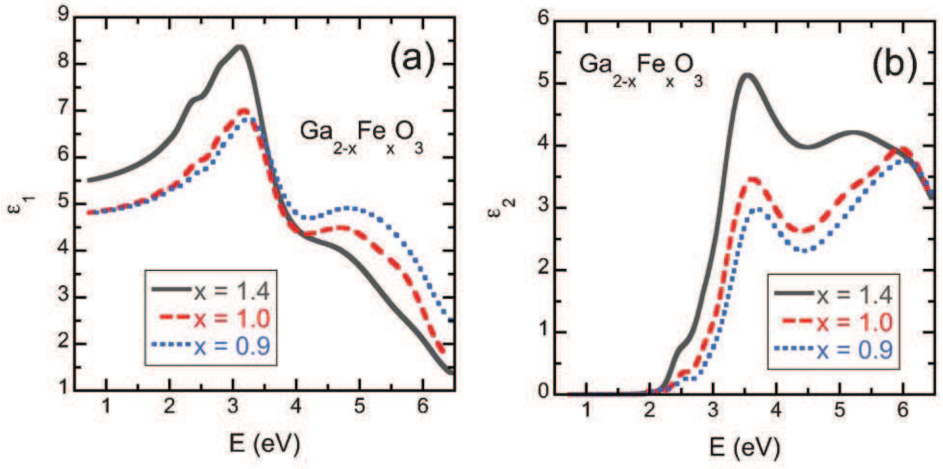

Figure 4.14: a) Real and (b) imaginary parts of ε spectra modeled with eight Tauc-Lorentz oscillators for the $Ga_{2-x}Fe_xO_3$ (x = 0.9, 1.0 and 1.4) thin films..

between our calculated curves and the experimental ones, due to the fact that the excitonic effects are excluded in our calculations. The calculated spectra show two main features at 3.5 and 4.7 eV which weakly depend on x. We first verify the electronic origins of the two main structures for the $\varepsilon^{(2)}$ spectra. To this end, we plot in Figure 4.15 the Fe and O projected density of states (DOS) in the region of interest, i.e. the valence and conduction states. Here we show both the e_g and the t_{2g} orbitals of Fe as well as the p-states of O and Fe. In fact, charge transfer transitions in a metal-oxide complex involve electron transition from O $2p$ toward $3d$ orbitals of the Fe sites, which is allowed from the point of view of electric-dipole transitions provided that there exists a spatial overlap of the wave functions of these orbitals and that one of them is occupied and the other empty. As a first stage, one can observe from the DOS plots that both the O p-states and the Fe d-states lie almost on the same energy range. This finding is supported by the partial charge plots, shown in the right panel of Figure 4.15. In particular, we present the partial charge densities integrated over a small energy interval around the peaks designated by arrows in both the valence and the conduction bands. These plots show

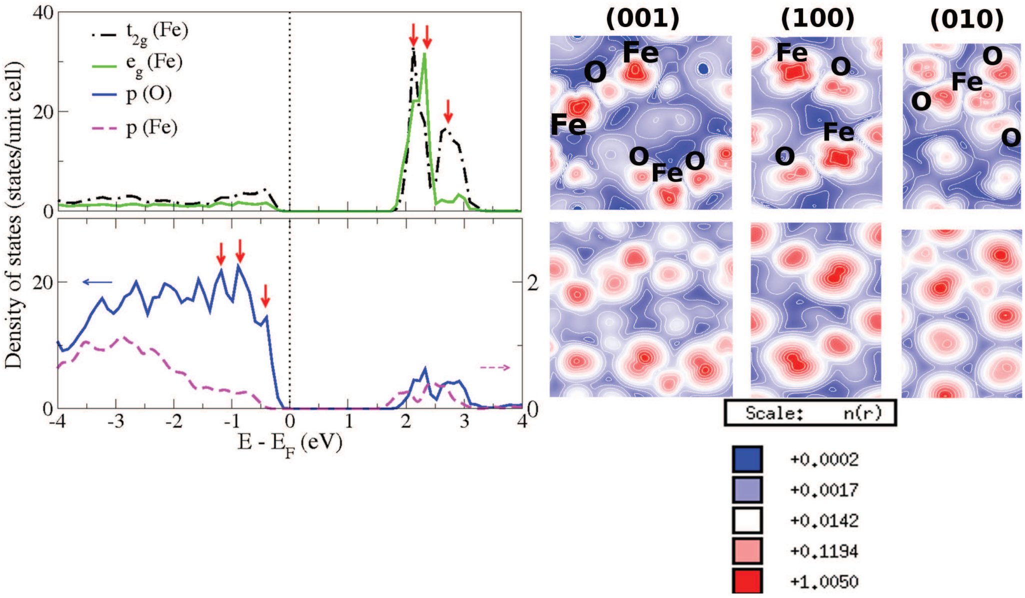

Figure 4.15: Left panel: d-states of Fe and p-states of O and Fe in an ideal GaFeO$_3$ unit cell. The red arrows mark the main peaks in the valence band of the O-p and the conduction band of Fe-d that are involved in the charge transfer transitions. Right panel: Partial charge distribution integrated over the energy range around the highest marked peak in the Fe-conduction band and the lowest one in the O-valence band, drawn with a logarithmic scale along the three crystallographic directions of the GFO unit cell. The spatial overlap between the O-p and the Fe-d orbitals can be observed..

a substantial spatial overlap between the O orbitals, which are obviously of p-like character, and the Fe orbitals, which have a d-like one. This finding also brings us to a fact that the presented p-states of Fe are in part the projection of the O p-states into the Fe spheres. Indeed, the energies of such kind of excitation, O-p to Fe-d charge transfer, involves the difference of the energy of a valence state and a conduction one. It can be easily remarked that the energies of the transitions obtained from the marked peaks in Figure 4.8 show good correspondence to the energies of the two main structures rising in the ε_2 spectrum. Thereby, we assign these two features to the O-p to Fe-d charge transfer transitions in GFO which is consistent with the current and previous experimental results [Kalashnikova 2005, Choi 2012].

However, the oscillatory strength of the main features of ε_2 increases with x which is consistent with the experimental observation shown in Figure 4.14. This can be understood in terms of promoting more O-2p to Fe-3d transitions as the Fe-d unoccupied DOS increases enhancing drastically the oscillator strength at the vicinity of those peaks.

4.4.2.2 Effect of site disorder

Ga1	Ga2	Fe1	Fe2	Disorder%
0	0	1	1	0%
0	0.25	1	0.75	12.5%
0	0.5	0.75	0.75	25%
0	0.75	0.75	0.5	37.5%
0	1	0.5	0.5	50%

Table 4.3: Description of the type of disorder considered for the Fe-Ga site interchange in a $GaFeO_3$ unit cell.

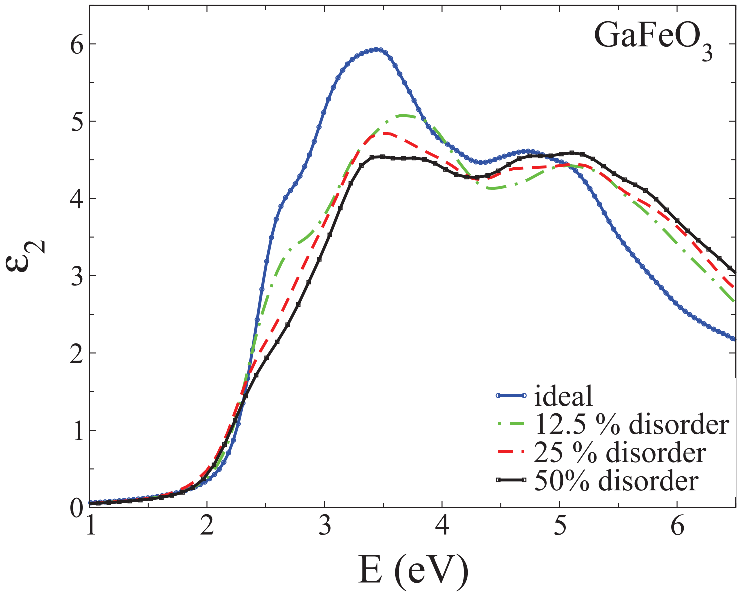

Figure 4.16: Calculated $\varepsilon^{(2)}$ spectra for different percentages of site disorder, Fe-Ga2 site interchange, in the $GaFeO_3$ unit cell.

It is noteworthy that the experimental and theoretical $\varepsilon^{(2)}$ spectra agree better for larger x, in terms of the relative amplitudes of the two main structures at 3.5 and 4.7 eV. This is linked to the fact that Fe-Ga site interchange has a diminishing probability as more Fe ions are populated into the unit cell. In fact, disorder in the cationic site occupation imposed itself as a property accompanying all elaborated $GaFeO_3$ samples regardless of the method of preparation, though its percentage is influenced by the recipe. To explain the observed differences in the $\varepsilon^{(2)}$ spectra between the experiments and calculations for small x values, we considered possible disorder in the cationic site occupations. To this extent, we have modeled different percentages of cation site disorder in a $GaFeO_3$ unit cell, in particular interchange between Fe and Ga ions as detailed in Table 4.3. The calculated spectra presented in Figure 4.16 reveal that the oscillator strength of the first major peak at 3.5 eV decreases as the disorder is enhanced, which is also accompanied by the broadening of the second major peak at 4.7 eV. Now, we consider the origin of the particular changes in the $\varepsilon^{(2)}$ spectra induced by promoting the cationic site disorder. To this end, we show in Figure 4.17 the Fe-d DOS as a function of different levels of disorder. We interpret the broadening of the second structure in the $\varepsilon^{(2)}$ spectra at 4.7 eV as the change in the unoccupied Fe d-DOS that become more dispersed in energy as the percentage of disorder increases.

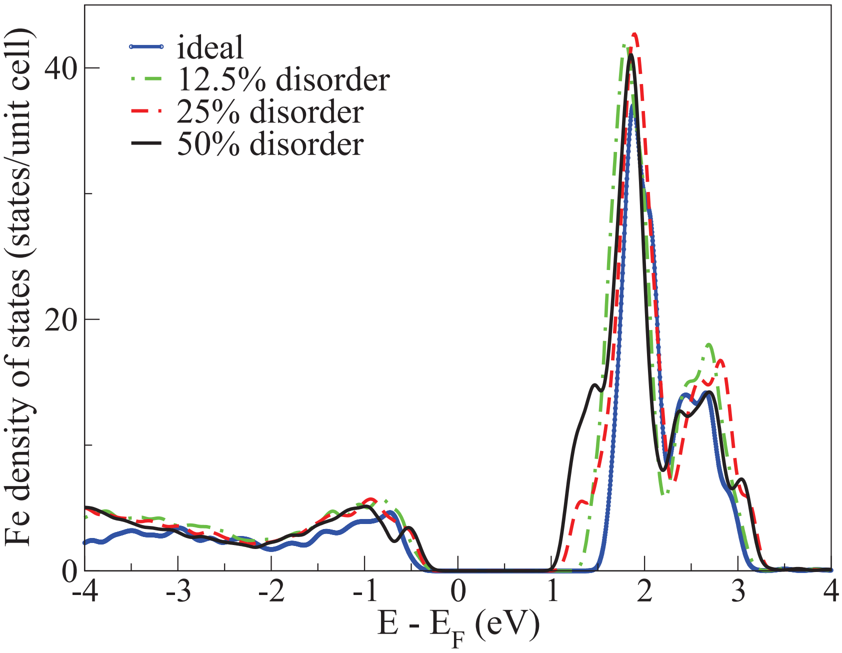

Figure 4.17: Calculated d-DOS contribution of the Fe projected DOS in $GaFeO_3$ unit cell shown for different percentages of site disorder.

The Ga1 site is probably very little influenced by the cationic disorder. Our

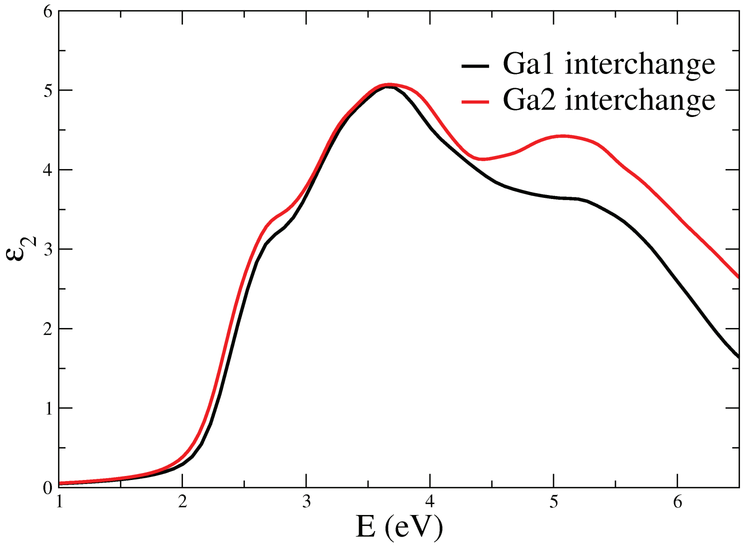

Figure 4.18: Calculated $\varepsilon^{(2)}$ spectra for the interchange of one Fe from the Fe2 site into the Ga1 or Ga2 sites in the $GaFeO_3$ unit cell.

calculations show that exchanging one Fe cation from the Fe2 or Fe1 site with the Ga1 site does not allow reproducing the shape of the experimental spectra, as opposed to the case of Fe sites with Ga2. Figure 4.18 shows the calculated $\varepsilon^{(2)}$ spectra obtained for the interchange when the origin of the interchanged cation is the Fe2 site. Similar curves are obtained when the Fe1 site is taken as the origin of the exchange.

In fact, the calculated spectra become more comparable to the experimental data for either large site disorder or large x. Large x compositions implicitly imply the occupation of Ga sites by Fe. Therefore, our observations suggest that, for all compositions, some Ga sites are occupied by Fe, which in turn suggests a high level of site disordering for GFO films containing a low amount of Fe atoms in its unit cell.

4.5 Conclusion

In summary, we have presented an investigation of the evolution of the structural, electronic, and magnetic properties of the polar ferrimagnet $Ga_{2-x}Fe_xO_3$ with increasing the iron concentration. We found that setting the U value to $8eV$ describes well the experimental observations. Bader charge analysis shows that the bonding in GFO is not completely ionic and that the energy band gap decreases while increasing the iron content x. We demonstrate that the structural parameters are influenced by the iron concentration which supports previous experimental findings. Though the magnetic properties seem to be enhanced as the iron concentration increases, the value of the magnetocrystalline anisotropy energy declines while conserving the magnetic easy axis. The direction of the magnetization easy axis and the drop of the MAE value was discussed and explained in view of the differences among the atomic sites. Indeed, the particularity of this system resides in this interplay between the structure, namely the different atomic sites, and its magnetic properties. Besides, we have presented the optical properties of GFO where we interpret the main optical structures arising from charge transfer transitions taking place from the O-2p toward the Fe-3d states. The intensity of these structures is influenced by both Fe-Ga site interchange and the Fe content. We found that a better agreement with experimental results is achieved while promoting more site disorder or increasing the Fe content. Our results point toward high levels of disorder present in GFO samples, exceeding 50%.

Chapter 5

Properties of MnPc/Co spinterface

Contents

5.1 Introduction

Organic semiconductors constitute promising candidates in spintronics-driven applications. In particular, metal phthalocyanines (MPc) have so far emerged as prototypical single molecule magnets that possess wide applicability in the field of molecular spintronics. Thanks to the bonding-induced exchange interaction, MPcs adsorbed on ferromagnetic substrates constitute a typical model of hybrid (semiconductor/ferromagnet) interface which serves as a key element toward building advanced spintronic devices where the electron spin is manipulated at the molecular level. In this chapter, we present a theoretical and experimental- coordinated study on the model spinterface between MnPc molecule and a Co single crystal surface. In the first section, we provide an overview of the well known properties of Pc/metal interfaces preceded by the properties of the Pc molecules. In particular, we consider the manganese phthalocyanine (MnPc) molecule which is the issue under investigation in the framework of this thesis. In the second part of this chapter, we present our results on the electronic and magnetic properties of Co/MnPc interface within including the van der Waals interaction and spin-orbit coupling.

5.2 MPc/metal interface: An overview

A meaningful interpretation of the hybrid Pc/metal system requires, as a first step, an accurate description of the electronic structure and the properties of a single molecule.

5.2.1 Phthalocyanine molecules

Phthalocyanines (Pcs) are organic planar macrocycles, with D_{4h} symmetry, that host a central atom that is often either a metallic one or H_2 in the case of a metal-free Pc. The central atom coordinates with four pyrrole rings. Pcs have been of wide interest in the scientific world especially from the nanotechnological point of view where MPcs are considered as prototypical organic semiconductors that serve as potential candidates for constituting light emitting diodes, field-effect transistors, and single-molecule devices. In this respect, MPcs show remarkable features such as their ordered growth in thin films and thermal stability during deposition. Besides, the unique structure and shape of Pcs make them ideally suited for scanning tunneling microscopy (STM) studies.

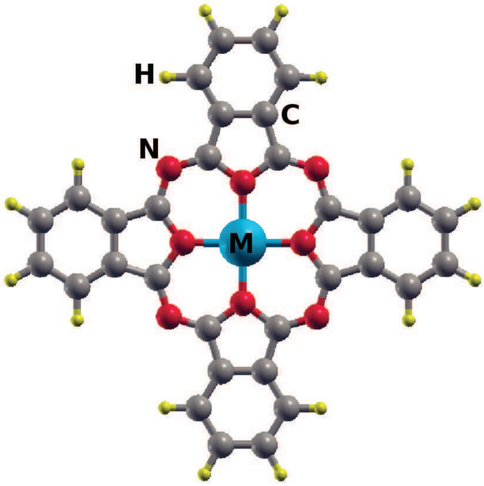

Figure 5.1: A schematic of the structure of a metal phthalocyanine molecule.

5.2.1.1 Electronic structure

The investigation of the electronic structure of MPcs has been the subject of different theoretical studies. In fact, determining and understanding the sequence of the outer molecular orbitals is of primary importance from a fundamental point of view, to interpret later the interface properties issued from molecule/substrate interactions, along with the interest in analyzing photoemission, optical, and transport experiments. In this sense, a detailed elucidation of the electronic structure of the MPcs and their ions is presented in the work of Liao *et al.* [Liao 2001]. According to the irreducible representation of the D_{4h} point group, the five metal *d*-orbitals transform as $a_{1g}(d_{z^2}), b_{1g}(dx^2-y^2), e_g(d_{zx}, d_{yz})$, and $b_{2g}(d_{xy})$. Taking the molecule to lie in the xy plane, the d_{xz} ,d_{yz} orbitals have π-character and the rest may be considered of σ type. In Figure 5.2, the highest occupied (HOMO) and the lowest unoccupied molecular orbitals (LUMO) of different MPcs are presented. In fact, the positions of the HOMO and LUMO highly depend on the central atom. Generally, the *d*-orbitals of the central metal atom move lower in energy as the atomic number of this atom increases such that: for M= (Fe or Co), the HOMO is mainly of *d*-character wheres for M= (Ni to Zn) the HOMO is determined by the a_{1u} Pc-orbital. On the other hand, the LUMO is mainly dominated by the $2e_g$ Pc-orbital contribution. In the framework of this thesis we are interested in the MnPc molecule. The electronic structure of MnPc is investigated in Calzolari *et al.* work [Calzolari 2007] where both the GGA and the GGA+U were explored due to the half occupation of the highly correlated $3d$ shell of the Mn central cation. Figure 5.3 shows their calculated spin resolved density of states (DOS) of the MnPc corresponding to PBE (a) and PBE+U functional. For the spin-up channel a_{1u} and $2e_g$ states are singly occupied HOMO and LUMO respectively, while the b_{1g} orbital is empty where the energy difference is $E = E(2e_g) - E(a_{1u}) = 1.41$ eV. As for the spin down, the HOMO and the LUMO are almost dominated by the degenerate couple of e_{1g} states, that are π-like orbital extended over the Mn and the Pc ring, where $\Delta E = 0.16$ eV. Indeed, the a_{1g} and the b_{2g} states, which are σ-like, are partially filled in the spin-up channel while the b_{1g} is completely empty in both spin channels. The unbalancing of these three orbitals between the spin up and down component results in a total magnetization of the MnPc molecule of $3\mu_B$. However, the description of the electronic structure is improved by

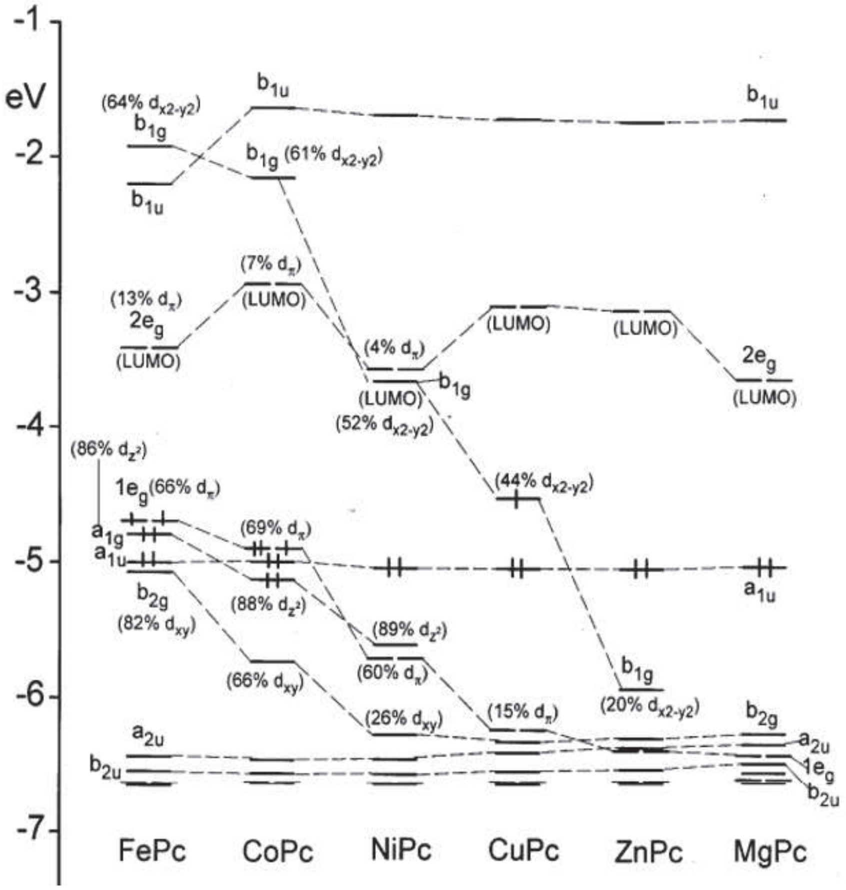

Figure 5.2: Orbital energy levels for the outer orbitals of different MPc molecules as presented in [Liao 2001].

adding the Hubbard term $U = 3eV$ on the Mn site, such that $\Delta E = 0.46$ eV (c.f. Figure 5.3(b)). Later, Stradi *et al.* [Stradi 2011] presented a systematic study of the electronic structure of MnPc using different exchange-correlation functionals ranging from B3LYP to HSE06 and the results were compared to UPS experiments. The results are shown in Figure 5.4. It was found that the screened hybrid HSE06 functional gives the overall best description of the MnPc electronic structure where a HOMO-LUMO band gap of 0.82 eV is calculated. However, reasonable results are obtained when the PBE0 functional is used.

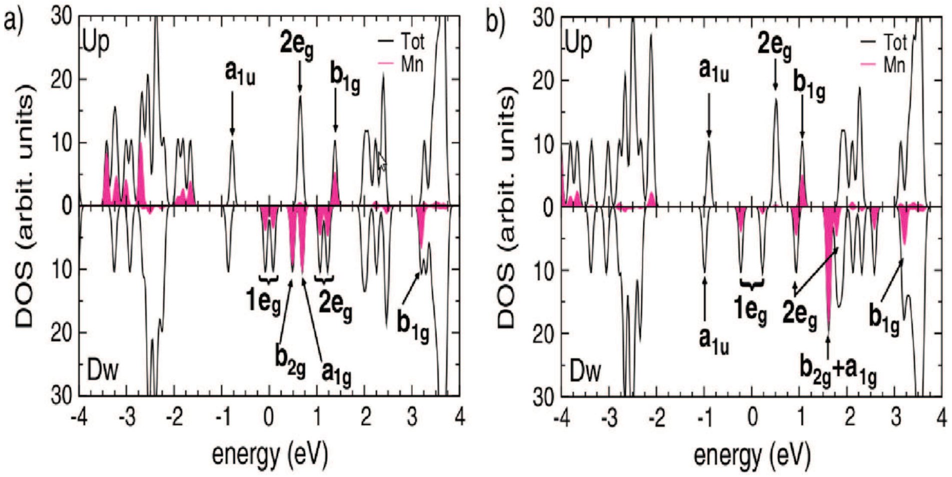

Figure 5.3: MnPc spin-resolved density of states (DOS) corresponding to (a) PBE calculation and (b) PBE $+U$ ($U = 3$ eV) functionals. The shaded areas are the projections on the atomic Mn states. Vertical arrows and labels identify the energy position of the peaks corresponding to molecular orbitals [Calzolari 2007].

5.2.1.2 Magnetic properties

The interesting class of MPcs is the one exhibiting a magnetic order due to the presence of a transition metal atom in the central site of the molecule. As important molecular magnets, 3d transition MPc were systematically studied in the bulk form, and it is well known that only the β-form polymorph of MnPc is ferromagnetic [Lever 1965]. This ferromagnetic behavior is explained qualitatively by the 90°superexchange interaction between nearest-neighboring Mn atoms via N atoms in Pc rings, resulting in the ordering of Mn^{2+} having an $S = 3/2$ state [Barraclough 1970]. In this case, the stacking arrangement of the planar MnPc molecules is along the monoclinic b-axis where each Mn atom lies directly above or below the N atom of the adjacent parallel molecule and the distance between Mn and the adjacent N atom is 3.38 Å . However, it has been shown that the magnetic properties differ between the bulk crystals and thin films of MnPc which has been attributed to the difference in superexchange interaction caused by microscopic modification of the crystal structure, i.e., the stacking arrangement of the molecules [Yamada 1998]. For instance, as shown in Figure 5.5 when the angle between the b-axis and the Pc-ring denoted by θ increases from 45°to 65°, the overlap of the dz^2 and the adjacent π orbital moves from the electron-rich N atom toward the node.

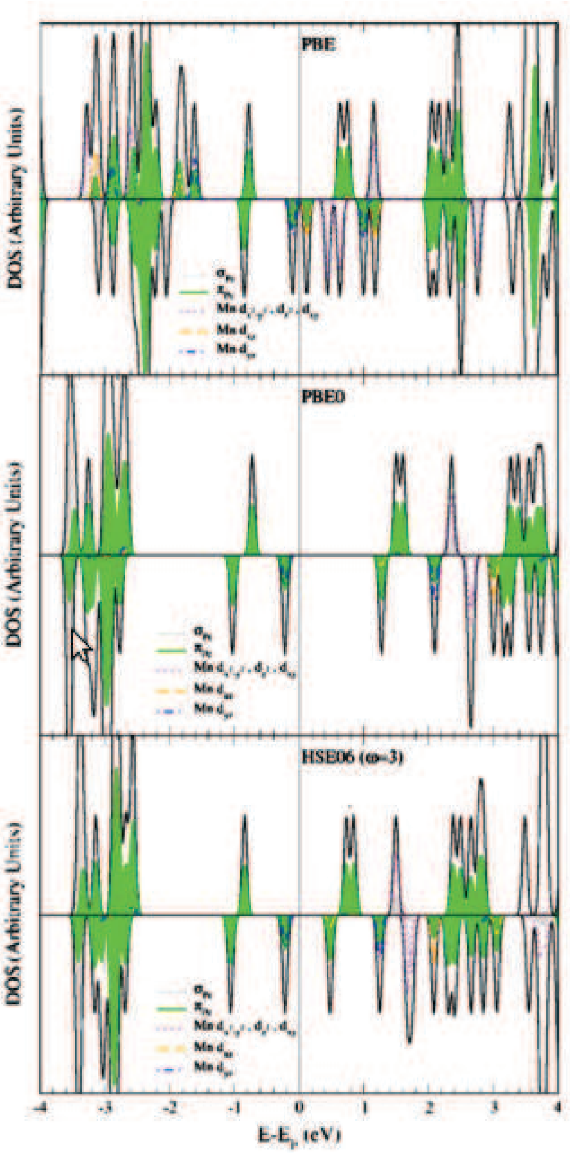

Figure 5.4: Projected Density Of States of MnPc, for PBE, PBE0, and HSE06 (ω = 3 Å $^{-1}$) functionals [Stradi 2011].

As a result the ferromagnetic interaction becomes weak. In order to cause antiferromagnetic superexchange coupling, it is necessary to make the mediating orbital to have a large overlap with both metal orbitals. Among the possible superexchange pathways in MnPc, $e_g - e_g$ interactions via π orbital with E_g symmetry can be antiferromagnetic. While in contrary to a_{1g}, the $e_g - E_g$ interaction among adjacent molecules does not become weak when θ changes from 45°to 65°. Another interesting aspect of the MPc molecules

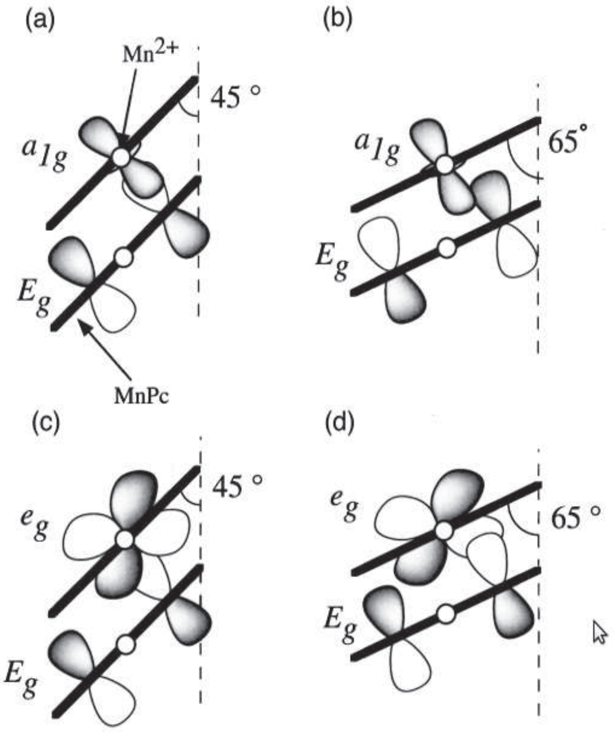

Figure 5.5: A schematic illustration of the $a_g - E_g$ and $e_g - E_g$ interactions in MnPc when $\theta = 45°$and $\theta = 65°$[Yamada 1998].

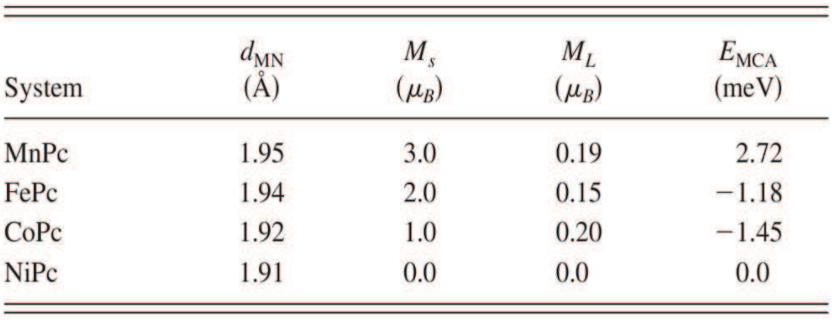

System	d_{MN} (Å)	M_s (μ_B)	M_L (μ_B)	E_{MCA} (meV)
MnPc	1.95	3.0	0.19	2.72
FePc	1.94	2.0	0.15	−1.18
CoPc	1.92	1.0	0.20	−1.45
NiPc	1.91	0.0	0.0	0.0

Figure 5.6: Total spin M$_S$ and orbital M$_L$ magnetic moments, and magnetocrystalline anisotropy energies E$_{MCA}$ in different MPc molecules as calculated in [Wang 2009]. Positive and negative signs of E$_{MCA}$ correspond to perpendicular and in-plane easy axes, respectively.

lies in theoretically exploring their magnetic anisotropy which is imperative in guiding the design of MPc-based molecular magnets. To this end, Wang et al. [Wang 2009] calculations showed that the spin magnetic moments of MPcs can be expressed as $8 - n\ \mu_B$ ($n = 5, 6, 7, 8$ for Mn, Fe, Co, and Ni).

Indeed, enhanced orbital moments were calculated for MnPc, FePc, CoPc. For instance, the orbital magnetic moment of MnPc is 0.19 μ_B which is the largest for the Mn atom in different environments. Another important finding was that MnPc molecules have sizable $MAE = 2.72$ meV with an easy axis perpendicular to the plane of molecule. Again, this MAE is large for Mn, which typically has it $3d$ shell filled (empty) in the majority (minority) spin channel.

5.2.2 MPcs adsorbed on metallic surfaces

The adsorption of a molecule on a metallic surface is governed by the type of interfacial interactions. The molecule might be either physisorbed in the absence of chemical interactions at the molecule/metal interface, where the weak van der Waals forces mediate the interactions, or chemisorbed in the presence of chemical interactions. In the later, the electronic states are significantly modified giving rise to modifications mainly in the molecule's properties. An interesting aspect is the magnetic interactions that arise in the case of a molecule adsorbed on a ferromagnetic surface.

In particular, we consider here the class of organic molecules due to the aforementioned interest in the hybrid organic/metal interface they form and which might display a high spin injection efficiency. In fact, the indirect exchange interaction might drive a ferromagnetic coupling between the metal site in the metallo-organic molecule and a ferromagnetic substrate which provides the possibility of controlling the magnetization of the molecular magnet. This kind of coupling have been demonstrated for Fe porphyrin molecules on ferromagnetic Ni and Co films in [Wende 2007]. Besides, another distinctive feature of the hybrid interfaces is the presence of spin polarized hybrid interface states that play a crucial role in the spin-injection efficiency across the interface thereby manipulating the magnetoresistance in organic spin valves. Such spin polarized hybrid interface has been investigated recently in CuPc/Fe hybrid interface [Methfessel 2011].

The interest in investigating MPc/metal interfaces has grown rapidly in the past few years motivated by the promising technological applications. Combined experimental and theoretical studies have been employed to unravel the properties and the physics underlying these hybrid interfaces ranging from the nature and geometry of the MPc's adsorption on the surface, to the electronic and magnetic properties issued from the interaction across the interface. Concerning the adsorption, near edge X-ray absorption fine structure spectroscopy (NEXAFS) as well as scanning tunneling microscopy (STM) results have reported the flat lying of the Pcs on metallic surfaces for ultra thin films which is the result of the domination of the molecule-substrate interactions over the molecule-molecule ones [Biswas 2007, Peisert 2005, Takacs 2008]. Indeed, DFT calculations have predicted the central atom-surface distances and the adsorption sites for different Pcs on metallic substrates which showed good agreement with X-ray standing wave spectroscopy (XSW) and STM experiments [Baran 2010, Heinrich 2010].

In fact, metallic substrates have strong impact on the electronic, magnetic, and transport properties of Pc molecules via the interactions present at the interface. Obviously, the type and strength of such interfacial interactions, determined by the adsorption site and distance, demonstrate to what extent the Pc 's properties are influenced. For instance, it has been shown that the hybridization and in particular the spin-polarized charge transfer at the interface promotes a reduction of the local magnetic moment of the central atom in MPcs [Brede 2010, Heinrich 2010, Iacovita 2008]. Besides, STM and DFT studies demonstrated that different strength of interfacial interactions, such as the strong chemisorption of CoPc on ferromagnetic Co(111) and its weaker one on paramagnetic Cu(111) surface, strongly influences the molecular conductance [Takacs 2008, Chen 2010].

5.2.3 MnPc adsorbed on metallic surfaces

In the framework of this thesis, we have considered the model interface between manganese phthalocaynine and the ferromagnetic Co(001) surface. In fact, the adsorption of MnPc on Co(001) or Cu(001) metallic surfaces has been the subject of the thesis of S. Javaid [Javaid 2011]. Preliminary DFT-*GGA* calculations and XAS experiments demonstrated that MnPc is physisorbed on Cu(001) while it is chemisorbed on Co(001). The calculated spin-polarized PDOS of MnPc/Cu(001) and MnPc/Co(001), shown in Figure 5.7, are compared to the Mn PDOS for free MnPc molecule. Due to physisorption of MnPc on Cu(001), the electronic structure of MnPc would not change significantly from that of a free molecule. However, the electronic structure of MnPc is strongly modified due to the influence of Co(001) substrate. Nevertheless, the adsorption mechanism of MnPc on Cu(001) changes from physisorption to weak chemisorption upon adding van der Waal (vdW) interactions to the calculations, which showed to be consistent with the performed XSW experiments. Indeed, both calculations and x-ray magnetic circular dichroism XMCD measurements showed that the Mn of the MnPc is ferromagnetically coupled to Co(001) and a reduction of the Mn magnetic moment to 2.9 μ_B was calculated.

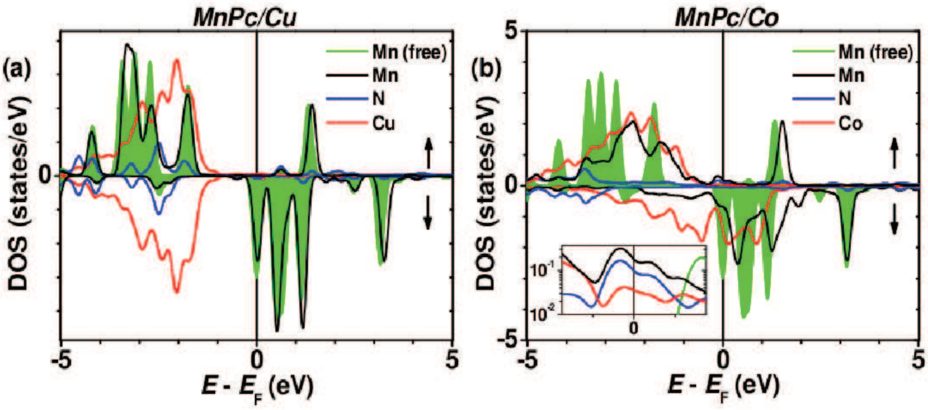

Figure 5.7: The calculated spin-polarized PDOS of Mn within the free MnPc molecule compared with the Mn, N and Cu(Co) spin-polarized PDOS for MnPc on (a) Cu(001) and (b) Co(001). Inset to panel (b): spin ↑ PDOS of MnPc/Co near E_F [Javaid 2013].

After this comprehensive study of the strong impact of the ferromagnetic Co substrate on the properties of MnPc, a better understanding of the Co/MnPc interface is still required. For instance, a more detailed description of the interface-formation mechanism is crucial. Besides, it is obviously interesting to include spin-orbit coupling to have access to calculating the orbital moments as well as the magnetic anisotropy of the molecule. In fact, our study, presented in the following section, basically addresses these arguments while trying to provide a more realistic description of the interactions across a MnPc/metallic interface.

5.3 Co/MnPc spinterface

Interestingly, spin-polarized direct and inverse photoemission experiments, performed by our experimental colleagues, have revealed a high degree of spin polarization at room temperature at the Co/MnPc interface. Besides, a magnetic moment was measured on the molecule's nitrogen π-orbitals by means of XMCD. These two findings invoked a more insight theoretical analysis of the interactions taking place at this interface. In this respect, we have conducted a systematic theoretical study of the magnetic properties of the Co/MnPc interface including the van der Waals interactions and spin-orbit coupling.

5.3.1 Computational details

Our density-functional based (DFT) calculations were carried by means of the VASP package [vas , Blochl 1994] and the generalized gradient approximation for exchange-correlation potential as parametrized by Perdew, Burke, and Ernzerhof [Perdew 1996]. We used the projector augmented wave (PAW) pseudopotentials as provided by VASP [Kresse 1999]. The van der Waals (vdW) weak interactions were computed within the so called GGA-D2 approach developed by Grimme [Grimme 2006] and later implemented in the VASP package [BucÌko 2010]. Our formalism can correctly reproduce the experimentally determined atomic distances between molecular sites and metallic sites. Fcc Co(001) surface was modeled by using a supercell of 3 atomic monolayers of $8x8$ atoms separated by a vacuum region. The lattice vector perpendicular to the surface is 3 nm. This results in a supercell of 249 atoms, including the 57 atoms of the MnPc molecule. Since experiments used cobalt epitaxially grown on Cu, we used the fcc lattice parameter of 0.36 nm for both cobalt and copper. We have found that additional monolayers will not change significantly the results [Chen 2010]. The distance between the adsorbed molecule and the Co surface was found to be 2.1 Å . A kinetic energy cutoff of 450 eV has been used for the plane-wave basis set. For our study of a single molecule on metallic surfaces, we used only the gamma point to sample the first Brillouin zone. DOS were calculated using a 1 meV energy mesh and a Gaussian broadening of 20 meV full-width at half-maximum. The spin-orbit coupling was included as a perturbation in the augmentation region at each atomic site as implemented in VASP [Kresse 1996]. The magnetic anisotropy energy (MAE) is calculated, as proposed in the force theorem, for two different spin quantization axes.

5.3.2 The highly spin polarized Co/MnPc interface

5.3.2.1 Photoemission results

Spin-polarized direct and inverse photoemission (PE) experiments were performed at room temperature (RT) on interfaces between fcc Co(001) and MnPc or H_2Pc as potential spinterface candidates. Those PE experiments reveal the presence of Pc-induced states close to E_F. In fact, to extract the signal coming only from the molecular sites, a subtraction procedure that takes into account the attenuation of the signal arising from ever deeper atomic sites away from the sample surface was adopted. The spin-resolved difference spectra of direct and inverse PE spectroscopy of Co/MnPc at RT (2.6 ML MnPc for direct and 2 ML MnPc for inverse PE) that were obtained by this subtraction procedure are shown in Figure 5.8. Both direct and inverse

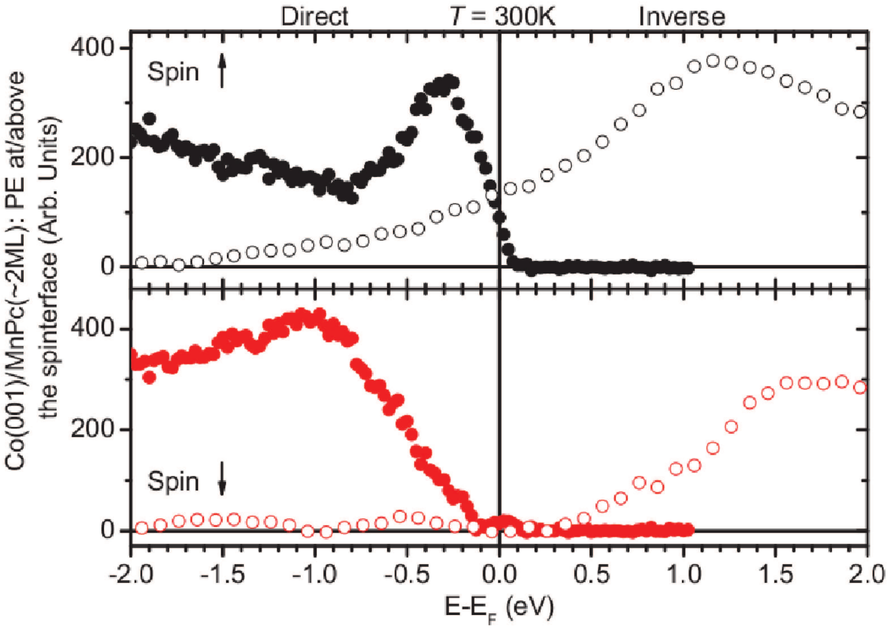

Figure 5.8: Spin-resolved difference spectra of direct (closed symbols: $h\nu = 20$ eV) and inverse (open symbols) photoemission (PE) spectroscopy at room temperature of Co/MnPc(2.6(2.0) ML for direct(inverse) PE) reveal a $P = 80\%$ at E_F.

PE experiments reveal significant (nearly no) spin ↑ (↓) intensity at/near E_F, which indicates a high polarization P of the Pc-induced states in the vicinity of E_F. It is noteworthy to state that very similar difference spectra (indirect PE) are also obtained in the case of H_2Pc, which shows that the central Mn^{2+} ion in MnPc plays a minor role in the formation of the spinterface. Indeed, the RT P at E_F of the first two layers of MnPc or H_2Pc adsorbed on Co(001) reaches 80% ±10%, i.e. is opposite in sign to that of bare Co.

5.3.2.2 Theoretical description of the spinterface

To more realistically describe the interface, our formalism now relaxes atomic positions and includes van der Waals forces so as to quantitatively reproduce the crucially important molecule-substrate distance inferred from x-ray standing wave measurements. This leads to a final distance Δz between Co and the adsorbed molecule of 2.1 Å .

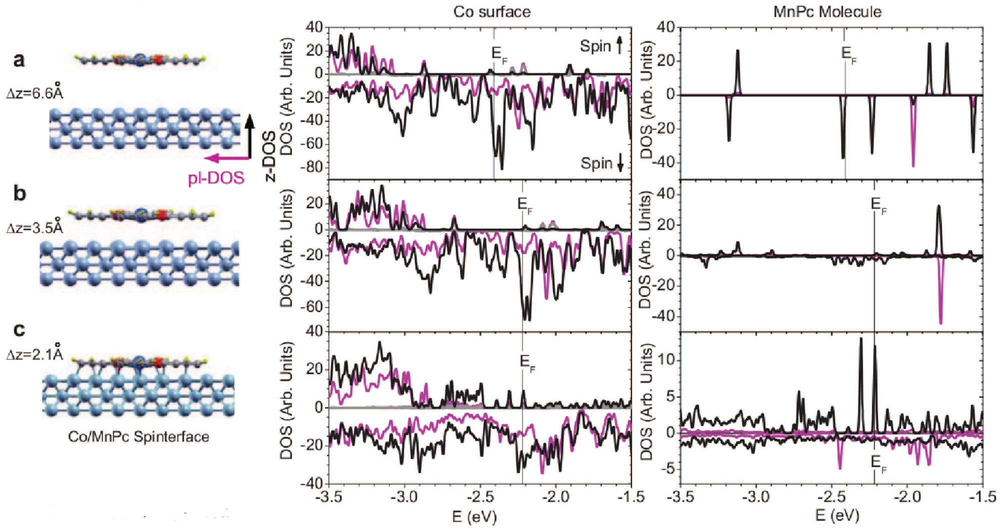

Figure 5.9: The z and planar density of states of the Co and the MnPc molecular sites calculated for three different configurations with varied Δz distance between the molecule and the surface. $\Delta z = 2.1$ Å corresponds to the final position of the spinterface..

To unravel the formation of the spinterface, we first consider the molecule-Co system as calculated using the actual atomic positions of the final interface, but we artificially impose $\Delta z = 6.6$ Å . Consequently, we can examine the states of the two systems using a common Fermi level in the absence of interactions between them as shown in Figure 5.9(a). The Co d-spin ↓ band crosses

E_F, while the d-spin ↑ band ends at $E - E_F = -0.7$ eV. Above this energy level, the spin ↑ sub-band exhibits only small DOS spikes that correspond to surface states. We note in particular one surface state at E_F with a strong perpendicular component (z-DOS, black) compared to its planar counterpart (pl-DOS, magenta). We emphasize that these surface states also exhibit a s-component of DOS (gray). Near E_F, the molecule exhibits a molecular orbital (MO) only in the spin ↓ channel. Adsorption-induced displacements of the molecule's atoms overall promote a slight energy shift (~ 30 meV) of the MOs.

We now turn on interactions between the molecule and the Co surface by reducing Δz to 3.5 Å as shown in Figure 5.9(b). At this distance, π orbitals that spatially extend perpendicularly to the nascent interface promote wave function overlap between the molecule and Co surface sites, causing E_F to shift from $E = -2.4$ eV to $E = -2.2$ eV. At the vicinity of E_F, the Co spin ↓ states and spin ↑ surface states are little affected. In contrast, the interaction strongly modifies the molecule's states: while planar states remain mostly unaffected, perpendicular states experience the onset of hybridization. In particular, this results in the energy dispersion of the initially sharp spin ↓ states in Figure 5.9(a) at -2.4 eV and -2.2 eV. We emphasize here that there are no spin ↑ MO at/near E_F at $\Delta z = 3.5$ Å .

At the final stage $\Delta z = 2.1$ Å (Figure 5.9(c)), the molecule and Co surface sites may fully hybridize to form the spinterface. More precisely, all combinations of $s - p$, $p - d$ and $s - d$ hybridization may occur. Although fcc Co(001) has, near E_F, no p-states and a highly spin-polarized d-band, the flat, spin-degenerate s-band that crosses E_F is essentially responsible, through $s - d$ hybridization, for the only moderate 45% spin polarization of conduction electrons. Yet, referring to Figure 5.9(c), the spinterface formation involves Co s-states (gray datasets) only very weakly. Thus, although fcc Co(001) is obviously not half-metallic, the Co/MnPc spinterface shall strongly transmit the highly spin-polarized d-component of the Co DOS and attenuate the s and p components.

In the following, we consider how the Co d-band DOS are transmitted onto the molecule in each spin channel. Prior to adsorption and in the spin ↓ channel, the Co d-band z-DOS intersects E_F and the z-DOS of the free molecule also exhibit a MO at/near E_F. Hybridization is therefore governed by the well-known spinterface mechanism of spin-dependent broadening of MOs due to

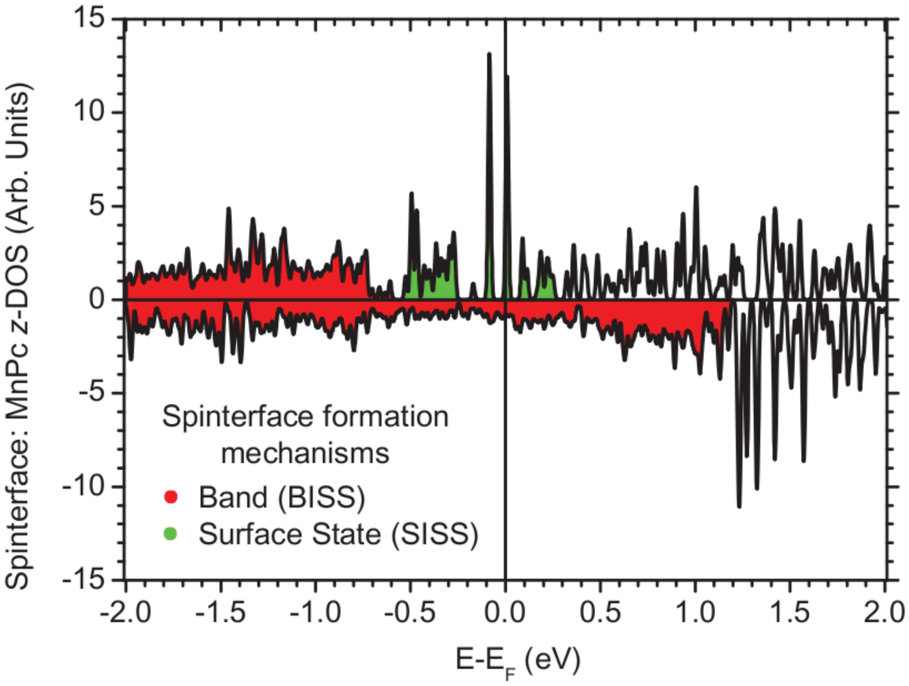

Figure 5.10: Calculated MnPc z-DOS showing the different mechanisms responsible for the spinterface formation. The area shaded by red resembles the band-induced spinterface states (BISS) while the green shaded one shows the surface-induced spinterface states (SISS).

band hybridization [Schmaus 2011, Barraud 2010, Sanvito 2010]. The resulting BISS (band-induced spinterface states) are shaded in red in Figure 5.10. These BISS exhibit a flat continuous energy dependence across E_F. However, the molecule does not exhibit any sizable, pre-existing spin ↑ z-DOS at the vicinity of E_F to hybridize with, and the Co surface's d-band does not cross E_F. Another spinterface formation mechanism must therefore account for the appearance of entirely new, hybrid states in the spin ↑ channel within -2.7 eV $\leq E \leq -1.9$ eV, i.e. at the vicinity of E_F, (c.f. right-hand panel of Figure 5.9(c) and the segment of the spinterface z-DOS shaded in green in Figure 5.10). We propose that pre-existing Co surface states (c.f. left-hand panel of Figure 5.9(a) and (b)) pin initially distant MOs to E_F. The narrow energy width of these surface-induced spinterface states (SISS) reflects that of both the pre-existing Co surface states and of the pre-existing MOs. Due to the Pauli exclusion principle, these newly formed SISS cannot occupy the spin ↓ states since they are already occupied by Co, and hence appear only in the spin ↑ channel. The presence of two sharp, tall peaks near E_F reflects a lifting of degeneracy induced by upward (downward) buckling of the benzene rings below (at) E_F along each of the two orthogonal axes that define the free molecule's 4-fold symmetry. This underscores how crucial it is to fully relax the interface structure if one wishes to study SISS.

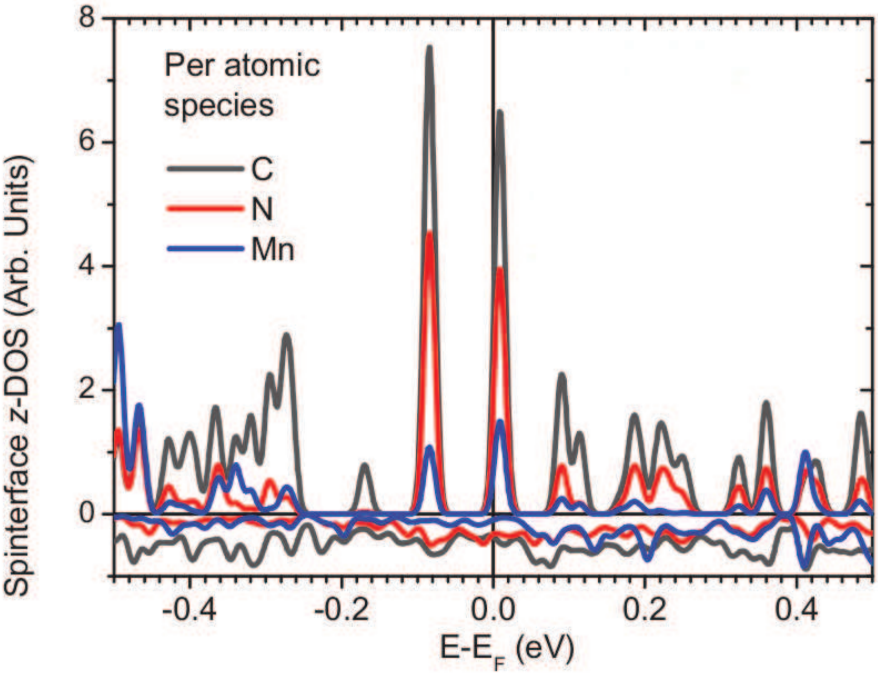

Figure 5.11: The calculated z-DOS per atomic species of the molecular sites showing that all the molecular sites are spin polarized around E_F.

Since surface states naturally lie at the vicinity of E_F, so shall SISS. Although SISS may appear as energetically sharp DOS peaks, which could reflect localization, SISS contribute to conduction across the interface. Indeed, the spectral signature of the SISS appears in the spin ↑ z-DOS of both Co surface and molecular sites. Focusing now on the DOS that contributes to transport at RT, we present in Figure 5.12(c-d) spin-polarized spatial maps, taken along the dashed line of Figure 5.12(a), of the Co/MnPc interface DOS within $E_F - 25$ meV $\leq E \leq E_F + 25$ meV (c.f. Figure 5.12(b)). Aside from the central Mn site, the remaining N and C sites exhibit very large positive P at E_F thanks to electronic states that are clearly hybridized with the Co interface atoms. In fact, these interface states are present on all atomic species of the molecule, as it can be seen from Figure 5.11, and their amplitude trends with the number of molecular nearest-neighbors for a given Co spinterface site.

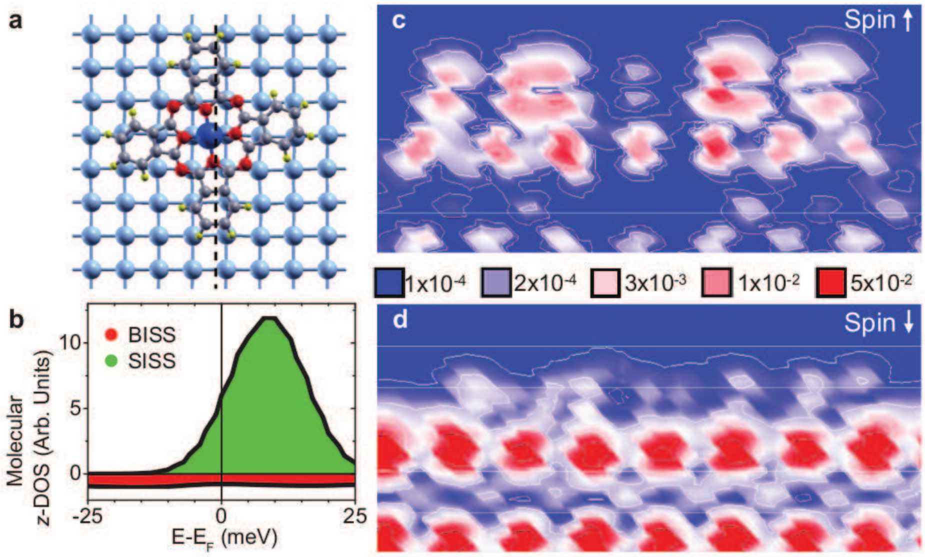

Figure 5.12: (a) Adsorption geometry of MnPc on Co(001). (b) The spin ↑ and ↓ z-DOS within $E_F - 25$ meV $\leq E \leq E_F + 25$ meV: SISS (BISS) lead to a sharp (monotonous) energy dependence at E_F; and (c-d) spatial charge density maps, taken along the dashed line of panel (a), show how the numerous C and N sites of MnPc exhibit a highly spin-polarized density of states at E_F that, furthermore, are hybridized with Co states and thus contribute to conduction. The maps are in units of $e{\cdot}\text{Å}^{-3}$.

At E_F, both the energetically smooth BISS in the spin ↓ channel and the energetically sharp SISS in the spin ↑ channel define the sign and amplitude of the spinterface's P. Due in large part to the energetically sharp SISS that crosses E_F, we find that $P = 80\%$. Thus, considering the limitations of the comparison, we find that both theory and the direct/inverse PE experiments yield the same sign and high amplitude of P at E_F (Figure 5.8 and 5.11). Furthermore, peaks in the spin ↑ (↓) PE (Figure 5.8) and DOS spectra (Figure 5.10) at $E - E_F = -0.3(-1.0)$ eV underscore a reasonably good agreement between theory and the direct PE experiment thanks to its good energy resolution (130 meV), while a qualitative agreement is found with inverse PE.

5.3.3 Magnetic properties of Co/MnPc spinterface

Since both PE experiments and ab-initio theory describe how the molecule's sites are spin-polarized, we now consider the magnetic properties of the spin-

	MnPc	MnPc	MnPc/Co	MnPc/Co
	M_S	M_L	M_S	M_L
Mn	3.1	$+0.04$	$+2.54$	$+0.02$
N (n.n)	-0.12	$+6.2 \times 10^{-4}$	$+0.01$	$+1 \times 10^{-3}$
N (f.n)	-0.02	$+4.4 \times 10^{-4}$	$+0.1$	-1.3×10^{-3}
C (pyrrole)	-0.09	-2×10^{-4}	$+0.08$	$+0.4 \times 10^{-4}$
C (benzene)	-0.02	-2.2×10^{-4}	-0.3	$+5.7 \times 10^{-4}$

Table 5.1: Calculated spin and orbital moments (in units of μ_B) for the MnPc molecular sites in the free molecule compared to those obtained when the molecule is adsorbed on the Co surface. We denote by (n.n) the N atoms that are nearest neighbors to Mn and by (f.n) the far neighbors.

terface. To get in sight of the magnetism of the spinterface, we compare in Table 5.1 the spin and orbital moments per atomic species for the free MnPc molecule and the adsorbed on Co surface and we show as well the local magnetization density plot in Figure 5.13.

Qualitatively, the hybridization of the molecule to the Co surface alters the magnetic coupling among the molecular sites such that Mn becomes ferromagnetically coupled to the N sites. The type of the magnetic coupling, whether ferromagnetic (F) or antiferromagnetic (AF), can be explained by a simpler picture based on Hund's rule. The hybridization leads to the direct $d-d$ FM coupling between the Mn site and Co, since the Mn d-band is less than half filled. Consequently, the N sites experience such coupling through the Mn-N σ-bond and thus N sites become FM coupled to Mn and Co. Indeed, the C sites in the benzene rings are AF coupled to the Co surface. Since the Co d-band is more than half filled, only the minority spin states are responsible for the hybridization to the C sites. This direct $p-d$ coupling leads to an exchange splitting of the C majority and minority states in an opposite direction to that of Co. On the other hand, the C sites of the pyrrole cage experience an additional coupling to the N sites, i.e. two competing coupling mechanisms, which leads to an overall spin moment which is parallel to that of Co.

Meanwhile, x-ray magnetic circular dichroism (XMCD) experiments were performed at the N K-edge of MnPc's 8 nitrogen sites. Referring to Figure 5.14(a), we witness XMCD intensity within the energy range corresponding

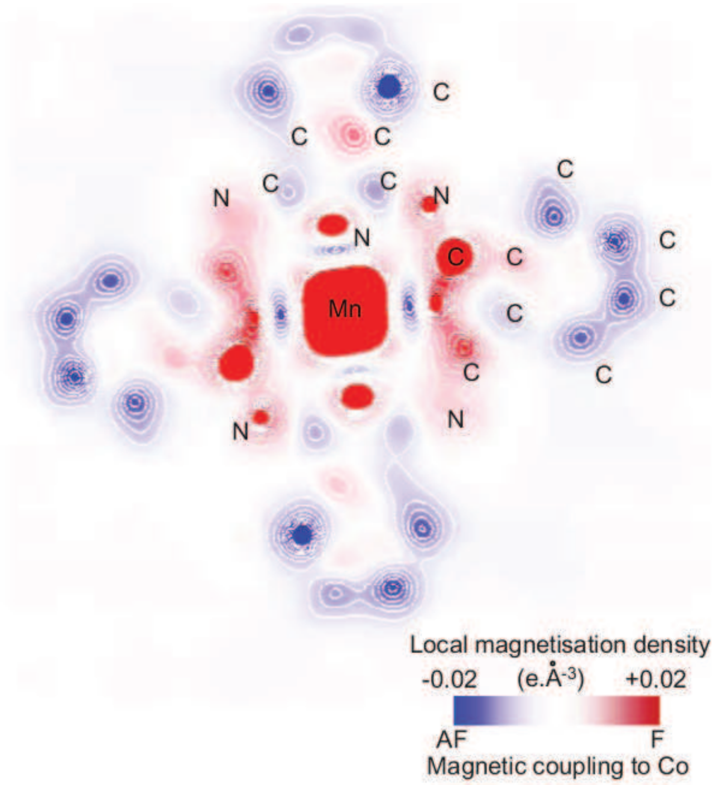

Figure 5.13: Top view of the on-site magnetization density of the MnPc molecule adsorbed onto Co(001) surface.

to final $2p$ π (i.e. that probe the z-DOS just above E_F), but not $2p$ σ- states. This unequivocal XMCD signal is very strong compared to the stray XMCD signal obtained when MnPc is adsorbed onto Cu(001) (c.f. Figure 5.14(b)), for which one does not expect the presence of on-site magnetic moments. Since these are K-edge transitions, we can only state that an orbital magnetic moment appears on the final N $2p$ π states at the Co/MnPc spinterface, the sign of which is in agreement with that found theoretically (c.f. Table 5.1). This experimentally confirms that the N z-DOS is spin-polarized as we have previously described theoretically.

The evolution of the magnetic state of the MnPc molecule upon adsorption on Co substrate can be analyzed in relation to the charge transfer occurring at the interface. We show in Table 5.2 the calculated Bader charges per atomic species using the Bader charge analysis [Tang 2009] on a fine fft-grid of $216 \times 216 \times 320$. It can be observed that, in total, the molecule gains about $3.5e^-$. In particular, the charge transfer from the Mn and pyrrole C molecular

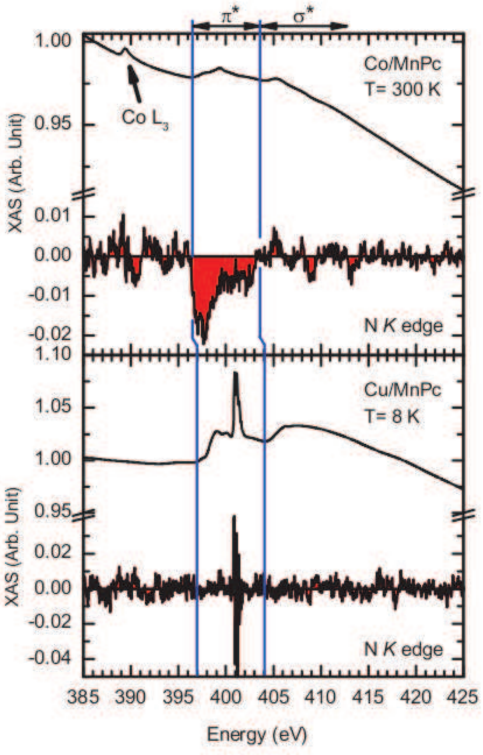

Figure 5.14: X-ray magnetic circular dichroic (XMCD) spectra reveal a magnetic polarization of the N π-states of MnPc for (b) Co/MnPc but not (c) Cu/MnPc..

sites reduces their magnetic moment. On the other hand, the C atoms in the benzene rings that gain electrons develop a larger magnetic moment than those of the pyrrole cage.

5.3.3.1 Magnetic anisotropy

We discuss now the magnetic anisotropy of the MnPc/Co interface. For free MnPc molecule, our calculations yielded a magnetic anisotropy energy value $MAE = 0.62meV$ calculated between in- and out-of plane magnetization direction. This value is less, by an order of magnitude, than the one reported using the full potential linearized augmented plane wave method [Wang 2009] and is in turn related to the value of the orbital moment which is also lower by an order of magnitude. This is due to the difference in treating the d-electrons among the two methods beside the different methods used to calculate the MAE. Nevertheless, the magnetization easy axis is found to be out of the molecule's plane consistently.

	Bader charge
Mn	+1.03
N (n.n)	−4.59
N (f.n)	−4.81
C (pyrrole)	+6.56
C (benzene)	−3.52

Table 5.2: The calculated Bader charges on the MnPc molecular sites upon adsorption on Co surface.

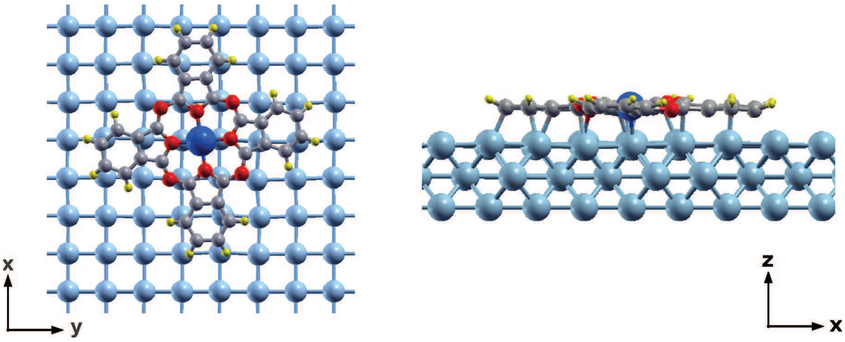

Figure 5.15: Structure showing the geometry of the MnPc molecule adsorbed on Co(001) and a lateral view showing the molecular distortions where the sites lying along x-axis are lower toward the surface than those along y.

Indeed, upon the molecule's adsorption on Co surface, the magnetization easy axis becomes along the molecule's plane where $MAE = 48$ meV. This large value is due to the fact that the magnetization of the system is overwhelmed by the Co contribution. Yet it is also interesting to find out the exact direction of the in-plane magnetization easy axis. For this sake, the calculations were performed along three in-plane magnetization directions along: x-axis, y-axis, and 45°in between. The easiest axis is found to be along the x-axis with $MAE = 0.66$ meV. In the following, we interpret the direction of the magnetization easy axis in terms of the structural properties of the interface. In fact, the atomic relaxation performed while including the van der Waals interaction yielded a ground state structure with geometric distortions where the molecular sites of the MnPc are vertically displaced (Figure 5.15). In particular, one can distinguish two behaviors: along the x-axis the atoms are displaced toward the Co surface with respect to Mn position, whereas along y-direction the atoms are displaced away. This promotes the x-axis to be the magnetization easy axis. Indeed, a similar symmetry reduction was previously reported for CoPc adsorbed on Cu(111) [Cuadrado 2010].

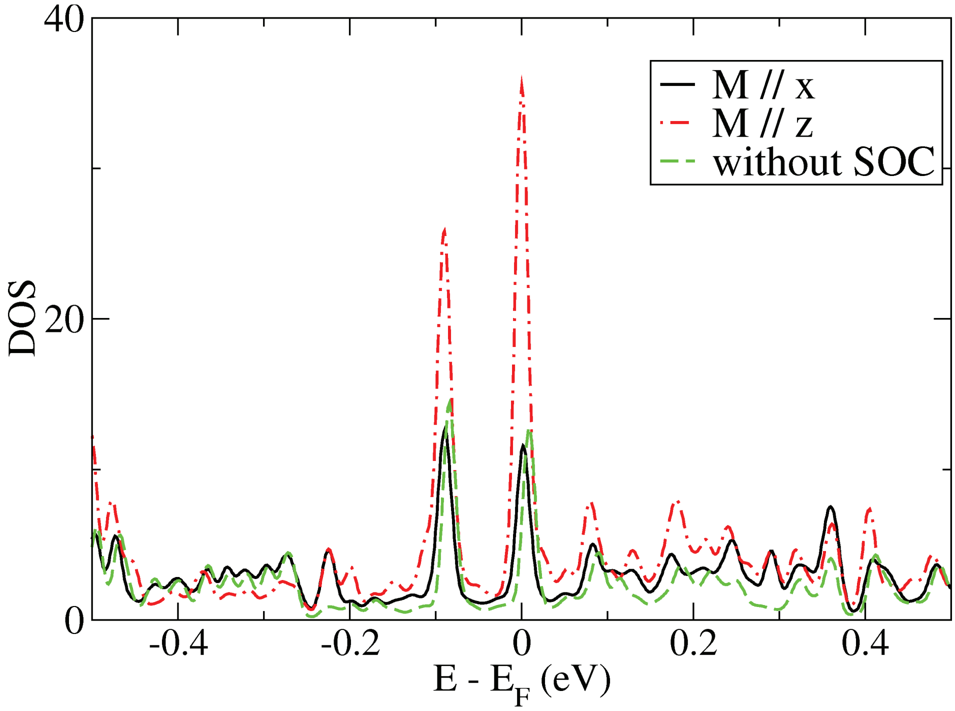

Figure 5.16: MnPc density of states for non-relativistic calculation of Co/MnPc compared to two spin-orbit coupling calculations where the magnetization is aligned: (black) in the molecule's plane along x-axis, (red) perpendicular to the molecule along z-axis.

It is also interesting to analyze the changes in the density of states (DOS) induced by including spin-orbit coupling as well as by changing the magnetization direction. The MnPc DOS obtained for two magnetization directions (x and z) are displayed in Figure 5.16 and compared to the non relativistic DOS. In the first stage, including spin-orbit coupling induces a shift of the molecular DOS peaks around E_F by about 7 meV to lower energy. As for the magnetization direction, the intensity of the DOS peaks when magnetization is along x-axis, the easy magnetization direction, is smaller than that when the magnetization is aligned along z-axis. In fact, spin orbit coupling induces some changes in the electronic structure depending on the direction of magnetization. Consequently, one may expect changes in the resistances especially that the energy range concerned is around the E_F leading to anisotropic magnetoresistance. Nevertheless, those limited differences in the DOS almost cancel when integrated leading to the small value of MAE obtained.

		$M \parallel x$	$M \parallel z$
$M_S(\mu_B)$	Mn	+2.542	+2.542
	N	+0.11	+0.11
$M_L(\mu_B)$	Mn	+0.02	−0.011
	N	−0.0003	+0.001

Table 5.3: Spin and orbital moment on Mn and N calculated for in plane x and out of plane z magnetization orientation.

Another interesting aspect about the magnetic anisotropy of the MnPc/Co interface is the re-orientation of the orbital moment upon changing the magnetization direction from in-plane to out-of-plane direction. We show in Table 5.3 the spin and orbital moments of the Mn and N corresponding to the hardest magnetization direction z and the easiest one x. It is obvious that the spin moment is isotropic, whereas the orbital moment is not. In fact, the orbital moment shows a remarkable behavior in response to the magnetization re-orientation to the out of plane direction where it changes sign. In particular, for the in plane magnetization direction, the spin and orbital moment of Mn are parallel while those of N are antiparallel. Meanwhile, when the magnetization aligns out of plane, they become antiparallel for Mn and parallel for N. This behavior conserves an antiparallel coupling between the Mn and N orbital moments regardless of the magnetization orientation.

5.4 Conclusion

In this chapter, we have presented a comprehensive theoretical study of the interface between manganese phthalocyanine and Co(001) including both van der Waals and spin-orbit interaction. A high spin polarization is observed around the Fermi level which is found to be consistent with photoemission results. We show in particular that the highly spin polarized interface is coordinated with an induced magnetism on the molecule's carbon and nitrogen sites upon hybridization to the Co surface. These results are depicted in relation to the charge transfer results obtained from Bader charge analysis. Besides, the magnetic anisotropy of the interface is investigated and compared to that of a free molecule. Indeed, the Co/MnPc interface involves differing spinterface formation mechanism in each spin channel which yield a high polarization. Beside the initially described mechanism in terms of band-induced spinterface states (BISS), we propose to extend the spinterface concept to include the additional spinterface formation mechanism of surface-induced spinterface states (SISS). The direct hybridization which drives both mechanisms introduces Co/MnPc spinterface as a strong candidate of an ideal spin polarized current source which could be promising once integrated in spintronic devices.

Chapter 6

General Conclusion

In the active field of research on functional materials that represent potential candidates for spintronics technological applications, a fundamental description of the electronic structure and magnetic properties of such materials becomes crucial. In this context, the present thesis addresses the investigation of the properties of two different classes of functional materials by means of the density functional theory (DFT) including the spin-orbit interactions. In particular, we have studied the magnetoelectric oxide gallium ferrite (GFO) and the hybrid interface between the organic molecule manganese phthalocyanine (MnPc) and the ferromagnetic Co(001) surface.

In the first part, we have presented a comprehensive study of the properties of GFO. Mainly, the dependence of the different properties on the iron concentration x has been demonstrated and discussed from the theoretical perception after it was witnessed experimentally in literature. At the first stage, we showed that using the Hubbard term $U = 8$ eV best describes the previously observed properties of GFO. The lattice parameters were found to vary as x is increased leading to an overall increase of the unit cell volume. We showed also that the band gap decreases while increasing x in relation to the changes in the conduction band induced by the excess Fe atoms. Interestingly, the magnetic properties seem to be enhanced with the increase of x. Indeed, the calculated magnetic anisotropy values showed a decrease as function of the Fe concentration while keeping the c-axis as the preferential magnetization direction in good agreement with experimental observations. The aspect and behavior of the magnetic anisotropy was interpreted in terms of the difference in the distortion directions among the Fe atomic sites. Bader charge analysis showed that the bonding in GFO is non completely ionic as it was previously expected. Besides, the optical spectra were calculated and directly compared to the experimentally measured once. The main optical features were interpreted, in view of the electronic structure, to be rising from the charge transfer transitions from the O $2p$-states toward the Fe $3d$-states.

By comparing the calculated and measured optical spectra, we have proven that the optical properties provide a good tool to determine the cationic site occupation in GFO. As a consequence, we point out high levels of site-disorder contained in GFO.

The peculiarity of GFO resides in the interplay between its structure and magnetic properties on one side and its electric and magnetic properties as well. In this respect, it is of great interest to compute and tune the magnetoelectric effect, i.e. the response to an electric field, in GFO which is unfortunately beyond the scope of this thesis.

In the second part, we have presented the calculated properties of the Co/MnPc interface, relaxed with including van der Waals interactions, which provide an interpretation for the observed experimental results. Specifically, the highly polarized interface measured by photoemission was verified by a careful analysis of the interface density of states in the vicinity of the Fermi level. In addition, this high polarization is coordinated with induced magnetic moments on the molecular sites, in particular we calculate an orbital moment on the N sites which was also verified by XMCD results. Indeed, the formation of the Co/MnPc spinterface was described by differing mechanisms in each spin channel: the original spinterface formation mechanism BISS (band-induced spinterface states) resulting from the spin selective broadening of the molecular orbitals on one hand and the SISS (surface-induced spinterface states) which is a new mechanism that we have proposed.

The direct hybridization which drives both formation mechanisms introduces Co/MnPc spinterface as a strong candidate of an ideal spin polarized current source which could be promising once integrated in spintronic devices. It is noteworthy to state that the similar results of a high polarized spinterface witnessed using other phthalocyanine molecules (e.g. $H_2Pc/Co(001)$) provide a direct proof of the promise behind the spinterface concept, which was initially described in terms of band-induced spinterface states (BISS). We proposed to extend this concept to include the additional spinterface formation mechanism of surface-induced spinterface states (SISS) that appear if the FM band of the dominant hybridization mechanism is absent near Fermi level in one spin channel. For instance, this criterion is satisfied in the spin $\uparrow$ channel by strong ferromagnets such as Co or Ni. By combining BISS and SISS in separate spin channels, we can, thus, guarantee a large spintronic response of a spinterface.

Bibliography

[Abrahams 1965] S. C. Abrahams, J. M. Reddy and J. L. Bernstein. *Crystal Structure of Piezoelectric Ferromagnetic Gallium Iron Oxide*. J. Chem. Phys., vol. 42, page 3957, 1965. 37

[Adler 1962] S. L. Adler. *Quantum theory of the dielectric constant in real solids*. Phys. Rev., vol. 126, pages 413–420, 1962. 60

[Andersen 1975] O. K. Andersen. *Linear methods in band theory*. Phys. Rev. B, vol. 12, pages 3060–3083, 1975. 14

[Anisimov 1997] V. I. Anisimov, F. Aryasetiawan and A. I. Lichtenstein. *First-principles calculations of the electronic structure and spectra of strongly correlated systems: the LDA+U method*. J. Phys.: Condens. Matter, vol. 9, page 767, 1997. 11, 40, 46

[Arima 2004] T. Arima, D. Higashiyama, Y. Kaneko, J. P. He, T. Goto, S. Miyasaka, T. Kimura, K. Oikawa, T. Kamiyama, R. Kumai and Y. Tokura. *Structural and magnetoelectric properties of Ga2-xFexO3 single crystals grown by a floating-zone method*. Phys. Rev. B, vol. 70, page 064426, 2004. VII, 2, 38, 39, 42, 43, 44, 45, 49, 50, 51

[Atodiresei 2010] N. Atodiresei, J. Brede, P. Lazic, V. Caciuc, G. Hoffmann, R. Wiesendanger and S. Blugel. *Design of the Local Spin Polarization at the Organic-Ferromagnetic Interface*. Phys. Rev. Lett., vol. 105, pages 066601–066604, 2010. 3

[Baran 2010] J. D. Baran, J. A. Larsson, R. A. J. Woolley, Yan Cong, P. J. Moriarty, A. A. Cafolla, K. Schulte and V. R. Dhanak. *Theoretical and experimental comparison of SnPc, PbPc, and CoPc adsorption on Ag(111)*. Phys. Rev. B, vol. 81, pages 075413–075425, 2010. 80

[Barraclough 1970] C. G. Barraclough, R. L. Martin, S. Mitra and R. C. Sherwood. *Paramagnetic Anisotropy, Electronic Structure, and Ferromagnetism in Spin Sâ=â3/2 Manganese(II) Phthalocyanine*. J. Chem. Phys., vol. 53, pages 1638–1642, 1970. 76

[Barraud 2010] C. Barraud, P. Seneor, R. Mattana, S. Fusil, K. Bouzehouane, C. Deranlot, P. Graziosi, L. Hueso, I. Bergenti, V. Dediu, F. Petroff and A. Fert. *Unravelling the role of the interface for spin injection into organic semiconductors.* Nature Phys., vol. 6, pages 615–620, 2010. 86

[Becke 1988] A. D. Becke. *Density-functional exchange-energy approximation with correct asymptotic behavior.* Phys. Rev. A, vol. 38, pages 3098–3100, 1988. 10

[Bertaut 2008] E. F. Bertaut and G. Bassi and. *Multiferroics: Towards a magnetoelectric memory.* Nature Mater., vol. 7, page 425, 2008. 37

[Bibes 2008] M. Bibes and A. Barthélḿy. *Multiferroics: Towards a magnetoelectric memory.* Nature Mater., vol. 7, page 425, 2008. VII, 2

[Binek 2005] Ch. Binek and B. Doudin. *Magnetoelectronics with magnetoelectrics.* J. Phys.: Condens. Matter, vol. 17, page L39, 2005. 2

[Biswas 2007] I. Biswas, H. Peisert, M. Nagel, MB. Casu, S. Schuppler, P. Nagel, E. Pellegrin and T. Chasse. *Buried interfacial layer of highly oriented molecules in copper phthalocyanine thin films on polycrystalline gold.* J. Chem. Phys., vol. 126, page 174704, 2007. 80

[Blochl 1994] P.E. Blochl. *Projector augmented-wave method.* Phys. Rev. B, vol. 50, page 17953, 1994. 13, 14, 40, 82

[Born 1927] M. Born and J. R. Oppenheimer. *Quantum theory of molecules.* Ann. Phys., vol. 389, pages 457–484, 1927. 6

[Brede 2010] J. Brede, N. Atodiresei, S. Kuck, P. Lazic, V. Caciuc, Y. Morikawa, G. Hoffmann, S. Blugel and R. Wiesendanger. *Spin- and Energy-Dependent Tunneling through a Single Molecule with Intramolecular Spatial Resolution.* Phys. Rev. Lett., vol. 105, page 047204, 2010. 80

[Brooks 1940] H. Brooks. *Ferromagnetic Anisotropy and the Itinerant Electron Model.* Phys. Rev., vol. 58, pages 909–918, 1940. 31

[Bruno 1989] P. Bruno. *Tight-binding approach to the orbital magnetic moment and magnetocrystalline anisotropy of transition-metal monolayers.* Phys. Rev. B, vol. 39, pages 865–868, 1989. 33

[Bruno 1993] P. Bruno. *Physical origins and theoretical models of magnetic anisotropy.* Ferienkurse des Forschungszentrums Julich, Julich, vol. 24, pages 24.1–24.28, 1993. 31

[BucÌko 2010] T. BucÌko, J. Hafner, S. LebeÌgue and J. G. AÌngyaÌn. *Improved description of the structure of molecular and layered crystals: Ab initio DFT calculations with van der Waals corrections.* J. Phys. Chem. A, vol. 114, page 11814, 2010. 82

[Bulut 1993] N. Bulut, D. J. Scalapino and S. R. White. *Comparison of Monte Carlo and diagrammatic calculations for the two-dimensional Hubbard model.* Phys. Rev. B, vol. 47, page 2742, 1993. 41

[Callaway 1955] J. Callaway. *Orthogonalized plane wave method.* Phys. Rev., vol. 97, pages 933–936, 1955. 13

[Calzolari 2007] A. Calzolari, A. Ferretti and M. B. Nardelli. *Ab initio correlation effects on the electronic and transport properties of metal(II)-phthalocyanine-based devices.* Nanotechnology, vol. 18, page 424013, 2007. IX, 74, 76

[Ceperley 1980] D. M. Ceperley and B. J. Alder. *Ground state of the electron gas by a stochastic method.* Phys. Rev. Lett., vol. 45, pages 566–569, 1980. 9

[Chen 2010] X. Chen and M. Alouani. *Effect of metallic surfaces on the electronic structure, magnetism, and transport properties of Co-phthalocyanine molecules.* Phys. Rev. B, vol. 82, page 094443, 2010. 80, 82

[Choi 2012] S. Choi, C. Lefev́re, F. Roulland, C. Mény, N. Viart, B. To, D. E. Shafer, R. Shin, J. Lee and W. Jo. *Optical transitions in magneto-electric Ga0.6Fe1.4O3 from 0.73 to 6.45 eV.* J. Vac. Sci. Technol. B, vol. 30, page 041204, 2012. 65

[Christensen 1971] N. E. Christensen and B. O. Seraphin. *Relativistic Band Calculation and the Optical Properties of Gold.* Phys. Rev. B, vol. 4, pages 3321–3344, 1971. 27

[Cuadrado 2010] R. Cuadrado, J. I. Cerda, Y. Wang, G. Xin, R. Berndt and H. Tang. *CoPc adsorption on Cu(111): Origin of the C4 to C2 symmetry reduction.* J. Chem. Phys., vol. 133, page 154701, 2010. 93

[Daalderop 1990] G. H. O. Daalderop, P. J. Kelly and M. F. H. Schurmans. *First-principles calculation of the magnetocrystalline anisotropy energy of iron, cobalt, and nickel.* Phys. Rev. B, vol. 41, pages 11919–11937, 1990. 31, 33

[Daalderop 1991] G. H. O. Daalderop, P. J. Kelly and M. F. H. Schuurmans. *Magnetocrystalline anisotropy and orbital moments in transition-metal compounds.* Phys. Rev. B, vol. 44, pages 12054–12057, 1991. 33

[Dediu 2009] V. A. Dediu, L. E. Hueso, I. Bergenti and C. Taliani. *Spin routes in organic semiconductors.* Nat. Mater., vol. 8, pages 707–716, 2009. 3

[D.Wang 1993] D.Wang, R.Wu and A. J. Freeman. *State-Tracking First-Principles Determination of Magnetocrystalline Anisotropy.* Phys. Rev. Lett., vol. 70, pages 869–872, 1993. 33

[Ebert 1988] H. Ebert, P. Strange and B. L. Gyorffy. *The influence of relativistic effects on the magnetic moments and hyperfine fields of Fe, Co and Ni.* J. Phys. F: Met. Phys., vol. 18, page L135, 1988. 27

[Ebert 2000] H. Ebert. Fully relativistic band structure calculations for magnetic solids-formalism and application. Springer, 2000. 29

[Ehrenreich 1959] H. Ehrenreich and M. H. Cohen. *Self-consistent field approach to the many-electron problem.* Phys. Rev., vol. 115, pages 786–790, 1959. 60

[Eschrig 1985] H. Eschrig, G. Seifert and P. Ziesche. *Current density functional theory of quantum electrodynamics.* Solid State Commun., vol. 56, pages 777–780, 1985. 29

[Eschrig 1987] H. Eschrig. Optimized lcao methods. Springer, 1987. 14

[Fletcher 1954] G. C. Fletcher. *Calculations of the first ferromagnetic anisotropy coefficient, gyromagnetic ratio and spectroscopic splitting factor for Nickel.* Proc. Phys. Soc. A, vol. 67, pages 505–519, 1954. 31

[Fock 1930a] V. Fock. *Approximation method for the solution of the quantum-mechanical many-body problem.* Z. Phys., vol. 61, page 126, 1930. 6

[Fock 1930b] V. Fock. *Self-consistent field with exchange for sodium.* Z. Phys., vol. 62, page 795, 1930. 6

[Frankel 1965] R. B. Frankel, N. A. Blum, S. Foner, A. J. Freeman and M. Schieber. *Ferrimagnetic structure of Magnetoelectric Ga2-xFexO3.* Phys. Rev. Lett., vol. 15, pages 958–960, 1965. 37

[Gajdos 2006] M. Gajdos, K. Hummer, G. Kresse, J. Furthmuller and F. Bechstedt. *Linear optical properties in the projector-augmented wave methodology.* Phys. Rev. B, vol. 73, page 045112, 2006. 63

[Grimme 2006] S. Grimme. *Semiempirical GGA-type density functional constructed with a long-range dispersion correction.* J. Comput. Chem., vol. 27, page 1787, 2006. 82

[Han 2007] M. J. Han, T. Ozaki and J. Yu. *Magnetic ordering and exchange interactions in multiferroic GaFeO3.* Phys. Rev. B, vol. 75, page 060404, 2007. 38

[Heinrich 2010] B. W. Heinrich, C. Iacovita, T. Brumme, D. J. Choi, L. Limot, M. V. Rastei, W.-A. Hofer, J. Kortus and J.-P. Bucher. *Direct Observation of the Tunneling Channels of a Chemisorbed Molecule.* J. Phys. Chem. Lett., vol. 1, page 1517â1523, 2010. 80

[Hobbs 2000] D. Hobbs, G. Kresse and J. Hafner. *Fully unconstrained noncollinear magnetism within the projector augmented-wave method.* Phys. Rev. B, vol. 62, page 11556, 2000. 40

[Hohenberg 1964] P. Hohenberg and W. Kohn. *Inhomogeneous electron gas.* Phys. Rev, vol. 136, pages 864–871, 1964. 7

[Iacovita 2008] C. Iacovita, M. V. Rastei, B. W. Heinrich, T. Brumme, J. Kortus, L. Limot and J. P. Bucher. *Visualizing the Spin of Individual Cobalt-Phthalocyanine Molecules.* Phys. Rev. Lett., vol. 101, page 116602, 2008. 3, 80

[Jansen 1988] H. J. F. Jansen. *Magnetc anisotropy in density-functional theory.* Phys. Rev. B, vol. 38, pages 8022–8029, 1988. 31

[Javaid 2010] S. Javaid, M. Bowen, S. Boukari, L. Joly, J.-B. Beaufrand, X. Chen, Y. J. Dappe, F. Scheurer, J.-P. Kappler, J. Arabski, W. Wulfhekel, M. Alouani and E. Beaurepaire. *Impact on Interface Spin Polarization of Molecular Bonding to Metallic Surfaces*. Phys. Rev. Lett., vol. 105, page 077201, 2010. 3

[Javaid 2011] Saqib Javaid. *Magnetism and Electronic Structure at Hybrid Manganese-Phthalocyanine/Metal Interfaces*. PhD thesis, Universite de Strasbourg, 2011. 80

[Javaid 2013] S. Javaid, S. Lebegue, B. Detlefs, F. Ibrahim, F. Djeghloul, M. Bowen, S. Boukari, T. Miyamachi, J. Arabski, D. Spor, J. Zegenhagen, W. Wulfhekel, W. Weber, E. Beaurepaire and M. Alouani. *Chemisorption of manganese phthalocyanine on Cu(001) surface promoted by van der Waals interactions*. submitted to Phys. Rev. B, 2013. IX, 81

[Julliere 1975] M. Julliere. *Tunneling between ferromagnetic films*. Phys. Lett. A, vol. 54, pages 225–226, 1975. 1

[Kalashnikova 2005] A. M. Kalashnikova, R. V. Pisarev, L. N. Bezmaternykh, V. L. Temerov, A. Kirilyuk and Th. Rasing. *Optical and Magneto-Optical Studies of a Multiferroic GaFeO3 with a High Curie Temperature*. JETP Lett., vol. 81, page 452, 2005. VII, 42, 46, 65

[Kalashnikova 2009] A. M. Kalashnikova. *Ultrafast light-induced dunamics of spin and lattice in iron oxides*. PhD thesis, Universiteit Nijmegen, April 2009. VII, 46

[Kim 2006] J.-Y. Kim, T.Y. Koo and J.-H. Park. *Orbital and Bonding Anisotropy in a Half-Filled GaFeO3 Magnetoelectric Ferrimagnet*. Phys. Rev. Letter., vol. 96, page 047205, 2006. 43, 52

[Koelling 1977] D. D. Koelling and B. N. Harmon. *A technique for relativistic spin-polarised calculations*. J. Phys. C: Solid State Phys., vol. 10, pages 3107–3114, 1977. 29

[Kohn 1954] W. Kohn and N. Rostoker. *Solution of the Schrodinger equation in periodic lattices with an application to metallic lithium*. Phys. Rev., vol. 94, pages 1111–1120, 1954. 14

[Kohn 1965] W. Kohn and L. J. Sham. *Self consistent equations in including exchange and correlation effects*. Phys. Rev., vol. 140, pages 1133–1138, 1965. 8

[Korringa 1947] J. Korringa. *On the calculation of the energy of a Bloch wave in a metal*. Physica, vol. 13, pages 392–400, 1947. 14

[Kresse 1996] G. Kresse and J. Furthmuller. *Efficient iterative schemes for ab initio total-energy calculations using a plane-wave basis set*. Phys. Rev. B, vol. 54, page 11169, 1996. 83

[Kresse 1999] G. Kresse and D. Joubert. *From ultrasoft pseudopotentials to the projector augmented-wave method*. Phys. Rev. B, vol. 59, page 1758, 1999. 25, 40, 82

[Lever 1965] A. B. P. Lever. *The magnetic behaviour of transition-metal phathalocyanines*. J. Chem. Soc., vol. 336, pages 1821–1829, 1965. 76

[Liao 2001] M. S. Liao and S. Scheinera. *Electronic structure and bonding in metal phthalocyanines, Metal:Fe,Co,Ni,Cu,Zn,Mg*. J. Chem. Phys., vol. 114, pages 9780–9791, 2001. IX, 3, 74, 75

[Liechtenstein 1995] A. I. Liechtenstein, V. I. Anisimov and J. Zaanen. *Density-functional theory and strong interactions: Orbital ordering in Mott-Hubbard insulators*. Phys. Rev. B, vol. 52, page R5467, 1995. 40

[Madsen 2005] G. K. H. Madsen and P. Novak. *Charge order in mangnetite. An LDA+U study*. Europhys. Lett., vol. 69, page 777, 2005. 41

[Martin 1968] P. C. Martin. Measurement and correlation functions. Gordon and Breach-New York, 1968. 57

[Methfessel 2011] T. Methfessel, S. Steil, N. Baadji, N. GroÃmann, K. Koffler, S. Sanvito, M. Aeschlimann, M. Cinchetti and H. J. Elmers. *Spin scattering and spin-polarized hybrid interface states at a metal-organic interface*. Phys. Rev. B, vol. 84, page 224403, 2011. 3, 79

[Mukherjee 2011] S. Mukherjee, V. Ranjan, R. Gupta and A. Grag. *Composition Dependence of Structural Parameters and Properties of Gallium Ferrite*. arXiv :1107.3623v1, 2011. VII, 39, 43, 44

[Naber 2007] W. J. M. Naber, S. Faez and W. G. van der Wiel. *Oragnic Spintronics.* J. Phys. D: Appl. Phys., vol. 40, pages R205–R228, 2007. 3

[Ozolins 1993] V. Ozolins and M. Korling. *Full-potential calculations using the generalized gradient approximation-Structural properties of transition metals.* Phys. Rev. B.:Condensed matter, vol. 48, pages 18304–18307, 1993. 10

[Peisert 2005] H. Peisert, I. Biswas, L. Zhang, M. Knupfer, M. Hanack, D. Dini, M.J. Cook, I. Chambrier, T. Schmidt, D. Batchelor and T. Chasse. *Orientation of substituted phthalocyanines on polycrystalline gold: distinguishing between the first layers and thin films.* Chem. Phys. Lett., vol. 403, pages 1–6, 2005. 80

[Perdew 1981a] J. P. Perdew and A. Zunger. *Self-interaction correction to density-functional approximations for many-electron systems.* Phys. Rev. B, vol. 23, page 5048, 1981. 9, 11

[Perdew 1981b] J. P. Perdew and A. Zunger. *Self-interaction correction to density-functional approximations for many-electron systems.* Phys. Rev. B, vol. 23, page 5048, 1981. 40

[Perdew 1992] J. P. Perdew and Y. Wang. *Accurate and simple analytic representation of the electron-gas correlation energy.* Phys. Rev. B, vol. 45, pages 13244–13249, 1992. 10

[Perdew 1996] J. P. Perdew, K. Burke and M. Ernzerhof. *Generalized Gradient Approximation Made Simple.* Phys. Rev. Lett., vol. 77, page 3865, 1996. 10, 40, 82

[Pickett 1989] W. E. Pickett. *Electronic structure of high-temperature oxide superconductors.* Rev. Mod. Phys., vol. 61, pages 433–512, 1989. 10, 11

[Pines 1964] D. Pines. Elementary excitations in solids. Wiley-New York, 1964. 57

[Proynov 1995] E. I. Proynov, E. Ruiz, A. Vela and D. R. Salahub. *Determining and extending the domain of exchange and correlation functionals.* Int. J. Quantum Chem., vol. 56, pages 61–78, 1995. 10

[Rado 1964] G. T. Rado. *Observation and possible mechanisms of magnetoelectric effects in a ferromagnet.* Phys. Rev. Lett., vol. 13, page 335, 1964. 2

[Rajagopal 1973] A. K. Rajagopal and J. Callaway. *Inhomogeneous Electron Gas.* Phys. Rev. B, vol. 7, pages 1912–1919, 1973. 28

[Remeika 1960] J. P. Remeika. *GaFeO3: A ferromagnetic-piezoelectric compound.* J. Appl. Phys., vol. 31, page 263S, 1960. 2, 37

[Roy 2011] A. Roy, S. Mukherjee, R. Gupta, R. Prasad, S. Auluck and A. Garg. *Crystal and Electronic Structures, Born Effective Charges, and Magneto-structural Coupling in Multiferroic Gallium Ferrite.* J. Phys.: Condens. Matter, vol. 23, page 325902, 2011. 39, 43, 45, 48

[Sanvito 2007] S. Sanvito. *Injecting and controlling spins in organic materials.* J. Mater. Chem., vol. 17, pages 4455–4459, 2007. 3

[Sanvito 2010] S. Sanvito. *Molecular spintronics: The rise of spinterface science.* Nature Phys., vol. 6, pages 562–564, 2010. 3, 86

[Schmaus 2011] S. Schmaus, A. Bagrets, Y. Nahas, T. K. Yamada, A. Bork, M. Bowen, E. Beaurepaire, F. Evers and W. Wulfhekel. *Giant magnetoresistance through a single molecule.* Nature Nanotech., vol. 6, pages 185–189, 2011. 86

[Schutz 1987] G. Schutz, W. Wagner, W. Wilhelm and P. Kienle. *Absorption of circularly polarized x rays in iron.* Phys. Rev. Lett., vol. 58, pages 737–740, 1987. 27

[Singh 2006] D. J. Singh and L. Nordstrom. Planewaves, pseudopotentials, and the lapw method. Springer, 2006. 13, 14

[Slater 1953] J. C. Slater. *An augmented planewave method for the periodic potential problem.* Phys. Rev., vol. 92, page 603, 1953. 14

[Slater 1954] J. C. Slater and G. F. Koster. *Simplified LCAO method for the periodic potential problem.* Phys. Rev., vol. 94, pages 1498–1524, 1954. 14

[Solovyev 1995] I. Solovyev, N Hamada and K. Terakura. *t_2g versus all 3d localization in LaMO$_3$ perovskites (M=Ti–Cu): First-principles study.* Phys. Rev. B, vol. 53, page 7158, 1995. 41

[Staedele 1999] M. Staedele, M. Moukara, J.A. Majewski, P. Vogl and A. Gorling. *Exact exchange Kohn-Sham formalism applied to semiconductors.* Phys. Rev. B, vol. 59, pages 10031–10043, 1999. VIII, 61, 62

[Stradi 2011] D. Stradi, C. Diaz, F. Martin and M. Alcami. *A density functional theory study of the manganese-phthalocyanine.* Theo. Chem. Acc, vol. 128, pages 497–503, 2011. IX, 75, 77

[Takacs 2008] A. F. Takacs, F. Witt, S. Schmaus, T. Balashov, M. Bowen, E. Beaurepaire and W. Wulfhekel. *Electron transport through single phthalocyanine molecules studied using scanning tunneling microscopy.* Phys. Rev. B, vol. 78, pages 233404–233408, 2008. 80

[Tang 2009] W. Tang, E. Sanville and G. Henkelman. *A grid-based Bader analysis algorithm without lattice bias.* J. Phys.: Condens. Matter, vol. 21, page 084204, 2009. 48, 90

[Terakura 1984] K. Terakura, T. Oguchi, A. R. Williams and J. Kubler. *Band theory of insulating transition-metal monoxides: Band-structure calculations.* Phys. Rev. B: Condensed Matter., vol. 30, pages 4734–4747, 1984. 10

[Trassin 2009] M. Trassin, N. Viart, G. Versini, S. Barre, G. Pourroy, J. Lee, W. Jo, K. Dumesnil, C. Dufour and S. Robert. *Room temperature ferrimagnetic thin films of the magnetoelectric Ga2-xFexO3.* J. Mater. Chem., vol. 19, page 8876, 2009. 2, 39, 52

[Trygg 1995] J. Trygg, B. Johansson, O. Eriksson and J. M. Wills. *Total energy calculation of the magnetocrystalline anisotropy energy in the ferromagnetic 3d metals.* Phys. Rev. Lett., vol. 75, pages 2871–2874, 1995. 31

[van der Laan 1998] G. van der Laan. *Microscopic origin of magnetocrystalline anisotropy in transition metal thin films.* J. Phys.: Condens. Matt., vol. 10, pages 3239–3253, 1998. 33

[vas] *VASP manual.* `http://www.cms.mpi.univie.ac.at/vasp/vasp/vasp.html`. 40, 82

[Vleck 1937] J. H. Van Vleck. *On the anisotropy of cubic ferromagnetic crystals.* Phys. Rev., vol. 52, pages 1178–1198, 1937. 31

[Wang 1996a] X. Wang, D. Wang, R. Wu and A. J. Freeman. *Validity of force theorem for magnetocrystalline anisotropy.* J. Magn. Magn. Mat., vol. 159, pages 337–341, 1996. 32

[Wang 1996b] X. Wang, R. Wu, D. Wang and A. J. Freeman. *Torque method for the theoretical description of magnetocrystalline anisotropy.* Phys. Rev. B, vol. 54, pages 61–64, 1996. 32

[Wang 2009] J. Wang, Y. Shi, J. Cao and R. Wu. *Magnetization and magnetic anisotropy of metallophthalocyanine molecules from the first principles calculations.* Appl. Phys. Lett., vol. 94, page 122502, 2009. IX, 3, 78, 91

[Weinert 1985] M. Weinert, R. E. Watson and J. W. Davenport. *Total-energy differences and eigenvalue sums.* Phys. Rev. B, vol. 32, pages 2115–2119, 1985. 32

[Wende 2007] H. Wende, M. Bernien, J. Luo, C. Sorg, N. Ponpandian, J. Kurde, J. Miguel, M. Piantek, X. Xu, Ph. Eckhold, W. Kuch, K. Baberschke, P. M. Panchmatia, B. Sanyal, P. M. Oppeneer and O. Eriksson. *Substrate-induced magnetic ordering and switching of iron porphyrin molecules.* Nature Mater., vol. 6, pages 516–520, 2007. 79

[Wiser 1963] N. Wiser. *Dielectric constant with local field effects included.* Phys. Rev., vol. 129, pages 62–69, 1963. 60

[Yamada 1998] H. Yamada, T. Shimada and A. Koma. *Preparation and magnetic properties of manganese(II) phthalocyanine thin films.* J. Chem. Phys., vol. 108, pages 10256–10261, 1998. IX, 76, 78

[Yang 2001] I. Yang, S. Y. Savrasov and G. Kotliar. *Importance of correlation effects on magnetic anisotropy in Fe and Ni.* Phys. Rev. Lett., vol. 87, page 216405, 2001. 31

[Zutic 2004] I. Zutic, J. Fabian and S. Das Sarma. *Spintronics: Fundamentals and applications.* Rev. Mod. Phys., vol. 76, pages 323–410, 2004. 1